2021

Experimental Investigations of Contact Friction and Transport Properties of Monolayer and Bilayer Graphene

Prakash Gajurel
prgajurel@mix.wvu.edu

Recommended Citation

Gajurel, Prakash, "Experimental Investigations of Contact Friction and Transport Properties of Monolayer and Bilayer Graphene" (2021). *Graduate Theses, Dissertations, and Problem Reports*. 7994.
https://researchrepository.wvu.edu/etd/7994

2021

EXPERIMENTAL INVESTIGATIONS OF CONTACT FRICTION AND TRANSPORT PROPERTIES OF MONOLAYER AND BILAYER GRAPHENE

Prakash Gajurel

EXPERIMENTAL INVESTIGATIONS OF CONTACT FRICTION AND TRANSPORT PROPERTIES OF MONOLAYER AND BILAYER GRAPHENE

Prakash Gajurel

Dissertation submitted to the Eberly College of Arts and Sciences at West Virginia University in partial fulfillment of the requirements for the degree of

Doctor of Philosophy

In

Physics

Mikel Holcomb, Ph.D., Chair

Wathiq Abdul -Razzaq, Ph.D.

Lian Li, Ph.D.

Fabien Goulay, Ph.D.

Department of Physics and Astronomy

Morgantown, West Virginia

2021

Key words: Graphene, Frictional force, Lateral force microscopy.

ABSTRACT

Experimental investigations of contact friction and transport properties of monolayer and bilayer graphene

Prakash Gajurel

Results obtained from experimental investigations of contact friction in monolayer and bilayers graphene and the related effects on their transport properties are presented here along with their discussion and interpretation. For this purpose, chemical vapor deposited (CVD) graphene samples on SiO_2/Si were prepared. The samples were characterized by atomic force microscopy (AFM), Raman and X-ray photoelectron spectroscopy (XPS). Summaries of the results are given below.

Defects-controlled friction in graphene is of technological importance but the underlying mechanism remains a subject of debate. The new results obtained from the analysis of lateral force microscopy images revealed that the contact friction in chemical vapor deposition (CVD) grown graphene is dominated by the vacancies formed instead of the bonding with add-atoms. This effect is attributed to the vacancy-enhanced out-of-plane deformation flexibility in graphene, which tends to produce large puckering of graphene sheet near the contact edge and thus increases the effective contact area. Modified graphene with large contact friction has a large density of defects. However, it remains a good electrical conductor, in which the carrier transport is strongly affected by quantum localization effects even at room temperature. Negative magnetoresistance observed in high defect density monolayer graphene samples revealed that scattering event is dominated by the short-range scattering (intervalley). It is also found that the oxidation process in mono-layer graphene is substrate sensitive since the oxidation process progresses much faster when the substrate is Strontium Titanate ($SrTiO_3$) compared to SiO_2 substrate. However, bilayer graphene exhibits great oxidation resistance on both substrates. These observations provide important information for tailoring the mechanical, electrical, and chemical properties of graphene through selected defects and substrates.

ACKNOWLEDGEMENTS

The research reported here on graphene was done under the direction and supervision of Professor Cheng Cen. I joined the research group of Professor Cen in 2015 at West Virginia University. I extend my thanks to Prof. Cen for her guidance and support during these investigations. I would also like to thank the Chairman (Prof. D.J. Pisano) and Associate Chair (Prof. Alan Bristow) for their guidance in my transition to my job with Intel in March 2020.

This dissertation was written in absentia in my off-hours during my training period with Intel. I would like to express my gratitude to Professor Emeritus Dr. Mohindar Seehra for his expert guidance in the organization of this dissertation and for his useful suggestions. I also thank the members of my Ph.D. committee (Professor Micky Holcomb, Professor Lian Li, Professor Wathiq Abdul-Razzaq and Professor Fabien Goulay) for their time in reviewing this dissertation and for their comments and suggestions. Special thanks to Professor Holcomb for chairing the Ph.D. committee.

I would like to thank Dr. Harley Hart and Dr. Qiang Wang for their help in using Shared Research Facilities throughout this work. Additionally, I would like to thank my lab colleagues both past and present; Dr. Weitao Dai, Dr. Sobhit Singh, Dr. Sujan Kasani and Ghadendra Bhandari for their help at various stages of this work. Also, I am thankful to Mina Aziziha and Navid Mottaghi for their help in PPMS measurements.

Finally, I thank my wife, Anjana Neupane Gajurel and my parents for their unconditional support throughout my work towards this degree.

Table of Contents

Contents

List of Figures

Chapter 1

Introduction and Background

1.1: Introduction:

The research presented in this dissertation is on graphene and the friction force on gradually oxidized monolayer and bilayer graphene. In order to place my research in proper context, relevant background information on the properties and applications of graphene are presented in this chapter. Furthermore, I have briefly mentioned friction properties at nanoscale dimensions and have reviewed relevant fundamental friction properties of graphene based on published papers cited here.

1.2: Review of the Crystal and Band Structure of Graphene:

Graphene is a single sheet of carbon atoms in hexagonal arrangement. It can be prepared from graphite via mechanical exfoliation i.e. by repeated peeling of small mesas of highly oriented pyrolytic graphite [1]. Graphite is a stacked arrangement of graphene sheets held together by van-der-Waals forces. Before monolayer graphene was isolated in 2004 by Geim and Novoselov, it was theoretically believed that two-dimensional compound could not exist due to thermal instability when separated. The sp^2 hybridization of carbon atoms and very thin atomic thickness make graphene a special 2D material.

The electronic structure of an isolated C atom is $1s^2, 2s^2\ 2p^2$. Each carbon atom provides six electrons, two of which belong to the core (1s) shell, with the remainder occupying the 2s, $2p_x$, $2p_y$ and $2p_z$ orbitals. The 2s an 2p states, known as 'valence states' have higher energies. In the excited state of the carbon atom, one of the electrons in the 2s subshell is promoted to 2p subshell such that there are four unpaired electrons in each of the orbitals. All these four electrons hybridized together in diamond (sp^3 hybridization) leading to tetrahedral structure. However, there occurs sp^2 hybridization in graphene involving the electrons in the orbitals $2s^1$, $2p_x^1$ and $2p_y^1$. The sp^2 hybridize orbitals form strong σ-bond in the plane of graphene with bond angle 120^0. These sigma bonds with the length of $1.42A^0$ are responsible for mechanical properties of graphene. The remaining one electron in the $2p_z$ orbitals forms the extended π-bond lying perpendicular to the plane. The extra π-electron in the $2p_z$ orbital is responsible for the graphene unique electrical and optical properties [2].

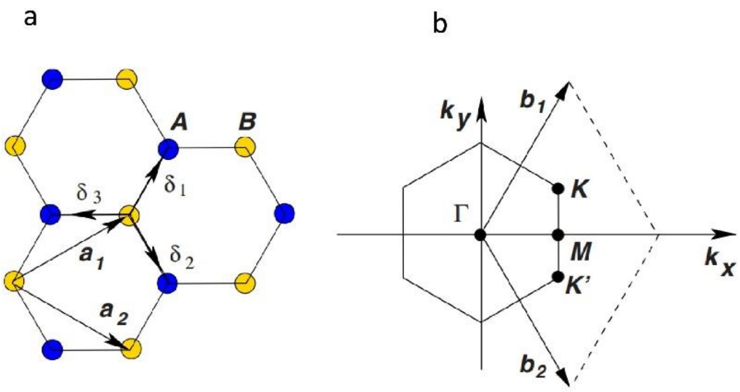

Figure 1.1: (a) Lattice structure of graphene consisting of two triangular lattices; (b) the corresponding Brillouin zone. The Dirac cones are located at K and K′ points [3].

Graphene's lattice structure can be considered as two equivalents triangular sublattice A and B with inversion symmetry as shown in figure 1.1(a). The lattice vectors in the unit cell in terms of the position coordinates are:

$$\boldsymbol{a_1} = (a\hat{x} + b\hat{y}) = \frac{a_0}{2}\left(3, \sqrt{3}\right) \text{ and } \boldsymbol{a_2} = (a\hat{x} - b\hat{y}) = \frac{a_0}{2}\left(3, -\sqrt{3}\right) \tag{1.1}$$

Here a_0 is the nearest neighbor carbon-carbon spacing (≈ 0.142 nm). Using $\boldsymbol{a_i}.\boldsymbol{b_j} = 2\pi\delta_{ij}$, the corresponding reciprocal lattice vectors are:

$$\boldsymbol{b_1} = \frac{2\pi}{3a_0}\left(1, \sqrt{3}\right) \qquad \boldsymbol{b_2} = \frac{2\pi}{3a_0}\left(1, -\sqrt{3}\right) \tag{1.2}$$

and the vectors for the two Dirac cones are expressed as

$$\mathbf{K} = \frac{2\pi}{3\sqrt{3}a_0}\left(\sqrt{3}, 1\right) \text{ and } \mathbf{K}' = \frac{2\pi}{3\sqrt{3}a_0}\left(\sqrt{3}, -1\right) \tag{1.3}$$

These vectors define the corresponding Brillouin zones as shown in figure 1.1 (b). The six corners of the first Brillouin zone, which consists of three pairs of inequivalent points K and

K$^{\prime}$, are called Dirac points. Below I have described the dispersion relation of graphene considering only nearest tight -binding model and using Bloch wavefunction for a crystal.

The most general form of the Schrodinger equation is as follow:

$$\widehat{H}\Psi = E\Psi \tag{1.4}$$

Where, Ψ is the wave function of an electron in unit cell, E is the energy and $\widehat{H}$ is the Hamiltonian operator. Let us consider a unit cell 'n' of graphene connected to 'm' neighboring unit cells by Hamiltonian H_{nm}, then the equation (1.4) in matrix form can be written as,

$$\sum_m \lfloor H_{nm} \rfloor \{\phi_m\} = E\{\phi_n\} \tag{1.5}$$

Where $\{\phi_m\}$ is a column vector denoting the wave function for unit cell 'm' and is given by $\{\phi_m\} = \{\phi_0\} \exp^{\mathbf{ik}.\boldsymbol{r_m}}$ [4] and with this; equation (1.5) can be expressed as,

$$\sum_m \lfloor H_{nm} \rfloor \{\phi_0\} \exp^{\mathbf{ik}.\boldsymbol{r_m}} = E\{\phi_0\} \exp^{\mathbf{ik}.\boldsymbol{r_n}}$$

$$E\{\phi_0\} = \sum_m \lfloor H_{nm} \rfloor \exp^{\mathbf{ik}.(r_m - r_n)} \{\phi_0\}$$

$$E\{\phi_0\} = [h(k)] \{\phi_0\} \tag{1.6}$$

Where, $(\boldsymbol{r_m} - \boldsymbol{r_n})$ is the vector connecting nearest neighbor atoms and,

$$[h(k)] = \sum_m \lfloor H_{nm} \rfloor \exp^{\mathbf{ik}.(r_m - r_n)} \tag{1.7}$$

Now we use the general form of equation (1.7) to find the matrix elements of graphene considering the nearest neighbor interaction.

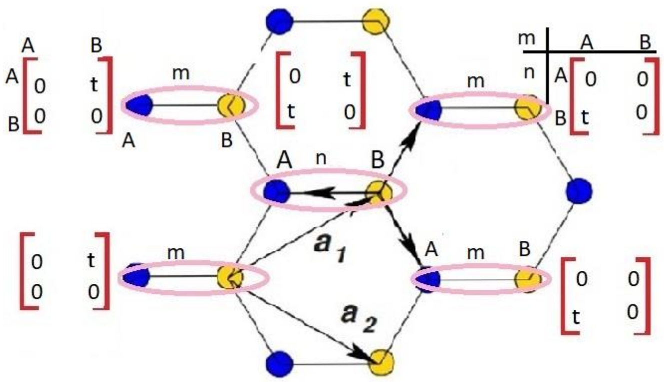

Figure 1.2: Schematic diagram showing the interaction between unit cells of graphene in the nearest neighbor tight-binding model. The nearest neighbor connection is represented by t.

The matrix elements due to the interaction between the unit cells; sanding at ‘n’ unit cell and to the nearest neighbor unit cells ‘m’ is shown in figure 1.2. We have assumed the nearest neighbor connection is t. The matrix h(**k**) summing over all neighbor unit cells with the corresponding phase factors can be expressed as,

$$\mathrm{h}(\mathbf{k}) = \begin{bmatrix} 0 & t \\ t & 0 \end{bmatrix} e^{ik.0} + \begin{bmatrix} 0 & 0 \\ t & 0 \end{bmatrix} e^{i\boldsymbol{k}.\boldsymbol{a_1}} + \begin{bmatrix} 0 & 0 \\ t & 0 \end{bmatrix} e^{i\boldsymbol{k}.\boldsymbol{a_2}} + \begin{bmatrix} 0 & t \\ 0 & 0 \end{bmatrix} e^{-i\boldsymbol{k}.\boldsymbol{a_2}} + \begin{bmatrix} 0 & t \\ 0 & 0 \end{bmatrix} e^{-i\boldsymbol{k}.\boldsymbol{a_1}}$$

$$\mathrm{h}(\mathbf{k}) = \begin{pmatrix} 0 & t(1 + e^{-i\boldsymbol{k}.\boldsymbol{a_1}} + e^{-i\boldsymbol{k}.\boldsymbol{a_2}}) \\ t(1 + \boldsymbol{e}^{i\boldsymbol{k}.\boldsymbol{a_1}} + e^{i\boldsymbol{k}.\boldsymbol{a_2}}) & 0 \end{pmatrix} = \begin{pmatrix} 0 & h_0^* \\ h_0 & 0 \end{pmatrix} \tag{1.8}$$

Where, $h_0 = t(1 + e^{i\boldsymbol{k}.\boldsymbol{a_1}} + e^{i\boldsymbol{k}.\boldsymbol{a_2}})$ and h_0^* is its complex conjugate.

Further,

$$h_0 = t(1 + e^{i\boldsymbol{k}.\boldsymbol{a_1}} + e^{i\boldsymbol{k}.\boldsymbol{a_2}})$$

$$h_0 = t(1 + e^{i\boldsymbol{k}.(a\hat{x}+b\hat{y})} + e^{i\boldsymbol{k}.(a\hat{x}-b\hat{y})})$$

$$h_0 = 1 + e^{ik_xb}\left(e^{ik_ya} - e^{ik_xb}\right)$$

$$h_0 = t[1 + 2e^{ik_xa} cosk_yb]$$

Substituting $a = \frac{3a_0}{2}$ and $b = \frac{\sqrt{3}a_0}{2}$ from equation (1.1), we get

$$h_0(\boldsymbol{k}) = t[1 + 2e^{i\frac{3a_0}{2}k_x} cos\frac{\sqrt{3}a_0}{2}k_y] \tag{1.9}$$

The eigen values of matrix (1.8) gives the energy dispersion relation i.e.

$$E(\mathbf{k}) = \pm|h_0|$$

$$E(\mathbf{k}) = \pm|t[1 + 2e^{i\frac{3a_0}{2}k_x} cos\frac{\sqrt{3}a_0}{2}k_y]|$$

Solving the absolute value $\sqrt{h_0 h_0^*}$ we get,

$$E(\mathbf{k}) = \pm t\sqrt{1 + 4\,cos\left(\frac{3a_0}{2}k_x\right) cos\left(\frac{\sqrt{3}a_0}{2}k_y\right) + 4cos^2\left(\frac{\sqrt{3}a_0}{2}k_y\right)}$$

$$E(\mathbf{k}) = \pm t\sqrt{1 + 4\,cos\left(\frac{\sqrt{3}c}{2}k_x\right) cos\left(\frac{c}{2}k_y\right) + 4cos^2\left(\frac{c}{2}k_y\right)} \tag{1.10}$$

Where, $c = \sqrt{3}\ a_0$ is the lattice constant and $t \approx 3\ eV$ is the next neighbor hopping energy [2].The plus sign applies to the upper (π*) and the minus sign the lower (π) band. If we the substitute the coordinates of Dirac point K and K′ from equation (1.3) into the equation (1.10) i.e. $k_x = \frac{2\pi}{3a_0} = \frac{2\pi}{\sqrt{3}c}$ and $k_y = \pm\frac{2\pi}{3\sqrt{3}a_0} = \pm\ \frac{2\pi}{3c}$, we get

$$E(\mathbf{k}) = \pm t\sqrt{1 + 4\,cos(\pi)\,cos\left(\pm\frac{\pi}{3}\right) + 4cos^2\left(\pm\frac{\pi}{3}\right)}$$

$$E(\mathbf{k}) = \pm t\sqrt{1 + 4.(-1).\frac{1}{2} + \frac{4}{4}}\ = 0 \qquad \text{(at Dirac points)} \tag{1.11}$$

The spectrum is symmetric around zero energy as shown in figure 1.3.

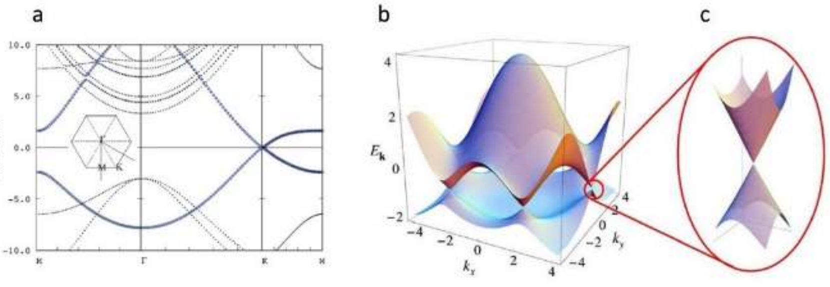

Figure 1.3: (a) Band structure of graphene. The blue lines in the figure correspond to wave function of P_z orbitals (b) energy spectrum, and (c) zoom in of the energy bands close to one of the Dirac points [3].

The corresponding energy bands of these two sublattices intersect at zero energy at K and K´ points, called Dirac points. Graphene's dispersion relation at low energy near Dirac points can be obtained by linear expansion near K-points:

Defining relative wave vector $\boldsymbol{q} = \boldsymbol{K} - \boldsymbol{k}$ at Dirac point **K**, we can write the equation (1.9) as

$$h_{\mathbf{0}}(\boldsymbol{K}+\boldsymbol{q}) = t[1 + 2e^{i\frac{3a_0}{2}(K_x+q_x)} \cos\left\{\frac{\sqrt{3}a_0}{2}\left(K_y+q_y\right)\right\}]$$

Substituting the coordinates of Dirac points K ($k_x = \frac{2\pi}{3a_0}$ and $k_y = \frac{2\pi}{3\sqrt{3}a_0}$), we get

$$h_{\mathbf{0}}(\boldsymbol{K}+\boldsymbol{q}) = t[1 + 2e^{i\pi}.\, e^{i\frac{3a_0}{2}q_x} \cos\left\{\frac{\pi}{3} + \frac{\sqrt{3}a_0}{2}q_y\right\}]$$

$$h_{\mathbf{0}}(\boldsymbol{K}+\boldsymbol{q}) = t[1 - 2e^{i\frac{3a_0}{2}q_x} \cos\left\{\frac{\pi}{3} + \frac{\sqrt{3}a_0}{2}q_y\right\}]$$

$$h_{\mathbf{0}}(\boldsymbol{K}+\boldsymbol{q}) = t[1 - 2e^{i\frac{3a_0}{2}q_x}\left\{\cos\left(\frac{\pi}{3}\right).\cos\left(\frac{\sqrt{3}a_0}{2}q_y\right) - \sin\left(\frac{\pi}{3}\right).\sin\left(\frac{\sqrt{3}a_0}{2}q_y\right)\right\}]$$

$$h_{\mathbf{0}}(\boldsymbol{K}+\boldsymbol{q}) = t[1 - 2e^{i\frac{3a_0}{2}q_x}\left\{\frac{1}{2}\cos\left(\frac{\sqrt{3}a_0}{2}q_y\right) - \frac{\sqrt{3}}{2}\sin\left(\frac{\sqrt{3}a_0}{2}q_y\right)\right\}] \qquad (1.12)$$

Now expanding this about **q =0** to first order, we get

$$h_{\mathbf{0}}(\boldsymbol{K}+\boldsymbol{q}) = -\frac{3at}{2}(\,q_x + iq_y) \;= -\hbar v_F(\,q_x + iq_y)\;,$$

where $v_F = \frac{3at}{2\hbar}$ is the Fermi velocity and $v_F \approx 10^6$ m/s [2]. About the Dirac point K, the Hamiltonian is thus

$$h(\boldsymbol{K}+\boldsymbol{q}) = \begin{pmatrix} 0 & h^*_{0(\boldsymbol{K}+\boldsymbol{q})} \\ h_{0(\boldsymbol{K}+\boldsymbol{q})} & 0 \end{pmatrix} \;=\; \hbar v_F \begin{pmatrix} 0 & q_x - iq_y \\ q_x + iq_y & 0 \end{pmatrix}$$

In terms of Pauli matrices $\sigma_x = \begin{pmatrix} 0 & 1 \\ 1 & 0 \end{pmatrix}$ and $\sigma_y = \begin{pmatrix} 0 & -i \\ i & 0 \end{pmatrix}$

$$h(\boldsymbol{K}+\boldsymbol{q}) = \hbar v_F\left(\sigma_x q_x + \sigma_y q_y\right) = \hbar\, v_F \boldsymbol{q}.\boldsymbol{\sigma} \tag{1.13}$$

From the matrix form of the Hamiltonian near the Dirac points (1.13), the energy bands near the Dirac point can be expressed as,

$$E(\boldsymbol{q}) = \pm\hbar v_F|\boldsymbol{q}| = \pm\hbar v_F\sqrt{\mathbf{q}_\mathbf{x}^2 + \mathbf{q}_\mathbf{y}^2} = \pm v_F|\boldsymbol{P}| \quad (\because \boldsymbol{P} = \hbar\boldsymbol{q}\,) \tag{1.14}$$

Near the Dirac point, the dispersion relation is linear in momentum and the energy is independent of the direction of the momentum, so in a plot of the dispersion relation of equation (1.14), we get perfect cones as shown in figure1.3 (c). According to special theory of relativity, the energy of a relativistic particle is given by:

$$\mathrm{E} = \pm\sqrt{\mathrm{m}^2\mathrm{c}^4 + \mathrm{c}^2\mathbf{p}^2} \tag{1.15}$$

where m is rest mass. When we set $\mathrm{m} = 0$, this gives dispersion relation $\mathrm{E} = \pm\mathrm{c}|\mathbf{p}|$ equivalent to that of light. This particle is massless neutrino, and the negative energy corresponds to an antineutrino. The dispersion of an electron in graphene near Dirac point is obtained by replacing c with $\mathrm{v_F}$. Thus, two-dimensional electron system in graphene makes it possible to study the properties of highly relativistic particles.

People have discovered many interesting properties of graphene. For examples, quantized conductance with minimum conductivity of $\sigma_0 = {2e^2}/{h}$ has been reported for graphene at zero magnetic field [5] . Electron mobility beyond 2.5 x 10^{5} cm^2/Vs has been reported for graphene at room temperature which is four times higher than that in III-V semiconductors [6] and 200 times that of Si; this is due to reduced electron-phonon interaction [7]. The electrons in graphene seem to be almost insensitive to disorder and electron -electron interactions and have very long mean free path. The mean free path larger than 1µm is reported in graphene [8]. In another words, charge carriers are able to travel sub-micrometer distances without scattering; this phenomenon is known as ballistic transport. However, the quality of the graphene and the substrate that is used will be limiting factors.

Recent discovery of superconductivity in magic -angle bilayer graphene by Pablo Jarillo-Herrero and his research group caught worldwide attention among the theorists and experimentalists. Bilayer graphene is a stack of two layers of graphene and if one of the graphene sheets is rotated with respect to another, it creates a Moire lattice- a periodic pattern within the twisted layers as shown in figure 1.4 (a). The Moire pattern creates a new landscape for electrons to move through, making it possible to fine-tune their behavior at atomic level. MacDonald and Rafi Bistritzer in a 2011 paper [9] predicted that any 2D materials at specific angle twists would have its property changed but nobody knew for certain how or what would happen.

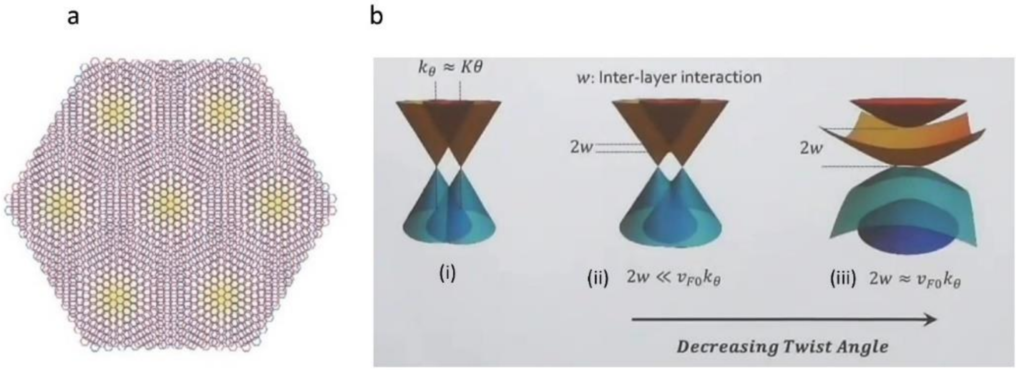

Figure 1.4: (a) Graphene Moire superlattice when one of the graphene layers is twisted relative to another (b) evolution of flat band when two Dirac cones interacts [10].

Figure 1.4 (b) illustrates evolution of flat band in the twisted bilayer graphene at the particular magic-angle of 1.1^0 and it can be described as: Separation of the Dirac cones in momentum space for twist angle θ is given by: (i): $\Delta K = 2K\sin\left(\frac{\theta}{2}\right)$ and for small angle $sin\theta \approx \theta$; $\Delta K = K\theta$ [Fig 1.4 b (i)]; (ii) For a small angle, interlayer tunneling of electrons open band gap [Fig 1.4 b (ii)]; and (iii) Decreasing the twist angle further, the Dirac cones becomes closer and band become flatter. At the specific angle i.e., magic angel forms perfect flat band [Fig 1.4 b (iii)].

MacDonald and Bristrizer [9] in their model had reasoned that degree of twist between two graphene sheets would control the ability of electrons to tunnel between them and predicted that electrons would slow at the magic angle, leaving them all at similar low energies, called a flat band, and thus more likely to interact. Unlike, in a paper published in *Physical Review Letters* [11], the Harvard University condensed matter theorists Tarnopolsky, Kruchkov and Vishwanath (known as TKV model) have explained that carbon atoms in the twisted sheets align more exactly in some places than in others. They assumed there are two types of alternating regions: areas where all the carbon atoms are fully aligned, and those where half the atoms are aligned, and half are offset. According to this model, most of the tunneling take place within the half-aligned regions, because repulsion between the fully aligned carbons atoms causes the graphene to spread apart in those regions, prohibiting tunneling there. As mentioned in TKV model [11], the electron stops altogether at the magic angle, putting them at precisely the same energy level- a perfect flat band. It is assumed that amount of extra energy that electrons would need to jump to the next-higher energy state becomes prohibitively large at the magic angle and this result in locking the electrons into that perfect flat band. Those conditions favor for strong correlation among electrons, inducing superconductivity and other novel physics. Twistronics began after this discovery and has triggered several important follow up discoveries in graphene research. Scientists at Columbia University invented a way to fine-tune the angle between adjacent layers of 2D materials and there by controlling the electronic properties [12].This represents a fundamentally new approach to device engineering.

Besides the unusual basic properties, graphene has the potential for many applications, from chemical sensors to transistors. In a graphene -based chemical sensing device, every atom in graphene is exposed to its surrounding allowing it to sense changes in its surroundings. Due to high surface to volume ratio, graphene- supercapacitor can store massive amount of electrical power. In addition, capability of graphene in handling high current densities (10^8 A/cm^2) together with its low resistivity and high thermal conductivity, makes it a potential material for interconnect applications [13, 14]. Ultrahigh bandwidth photodetectors made from single and multilayers graphene have been also reported [15]. Graphene is gas impermeable, chemically, and thermally stable making it an excellent candidate as a solid lubricant and protective coating material. Unlike liquid lubricants, solid lubricants and coating cannot evaporate and deplete. Liquid lubricants lose their lubricative ability at high temperatures, near the boiling point while solid lubricants can generally withstand much higher temperatures [16].

1.3: Friction at Nanoscale Dimensions:

Friction force for two bodies in contact may be defined as the force acting in the plane of the interface that opposes the relative lateral displacement of one surface with respect to the other. Friction is mainly divided in two categories namely, static, and kinetic friction. The static friction force is the force that prevents slip, whereas kinetic friction is the interfacial force that opposes slip when two bodies are in relative tangential motion. One of the major characteristics of the kinetic friction is that it is dissipative where mechanical energy converts to other forms, eventually degrading to thermal energy. Identifying and understanding mechanisms of frictional dissipation has long been of scientific interest and there has been renewed focus on this topic with the introduction of the atomic force microscope, which enabled to better understand how the friction forces experienced by macroscopic bodies arise from atomic level interactions[17-22].

According to the well-known Amontons' law [23], the friction force (F_r) between two macroscopic bodies is linearly proportional to the applied load (L), that is $F_r = \mu L$, where μ is the coefficient of friction. Friction force is also independent of the macroscopic contact area. Later it was noted that a macroscopic contact is rough and consists of a large number of smaller contacts, called asperities and total area of true contact ($\sum A_{asperity}$) is less the microscope area (A_{micro}). The frictional force was shown to be proportional to this true contact area, that is $F_r = \tau \sum A_{asperity}$, where τ is the effective shear strength of the contacting bodies [24].

Macroscopic laws of friction do not generally apply to nanoscale contacts. The friction behavior on the nanoscale is based on the three major contributing factors, namely adhesion at the tip-sample interface, high impact velocity -related deformation at contacting asperities, and atomic scale stick-slip. An understanding of how friction force depends on applied load and contact area at these scales is essential for the design of miniaturized devices with optimal mechanical performance. Defining contact area is one of the major challenges for understanding friction at nanoscale dimensions because fundamentally contact is formed by atoms interacting across the interface. Yifei Mo [25] and his research team performed the molecular dynamics simulations of normal loading and friction in the absence of van der Waals forces and their results are shown in figure 1.5 (*graph on the lest-hand side*). The above results demonstrated that $A_{real}\, \alpha\, L$ (Fig 1.5 b) and $F_f = \tau A_{real}$ (Fig 1.5 c) with constant τ which is consistent with the relation $F_f \alpha\, L$ (Fig 1.5 a). The friction force is proportional to contact area at all length scale as the contact area is correctly defined at each length scale. Further, Yifei Mo *et al.* investigated the effect of van der Waals adhesion on contact behavior by adding these forces to the tip-sample interactions and by performing additional molecular dynamics simulations, they found that the relation $F_f = \tau A_{real}$ (Fig 1.5a *on the right-hand side*) still holds, which demonstrates that friction is controlled by the short range i.e., chemical interactions even in the presence of dispersive force.

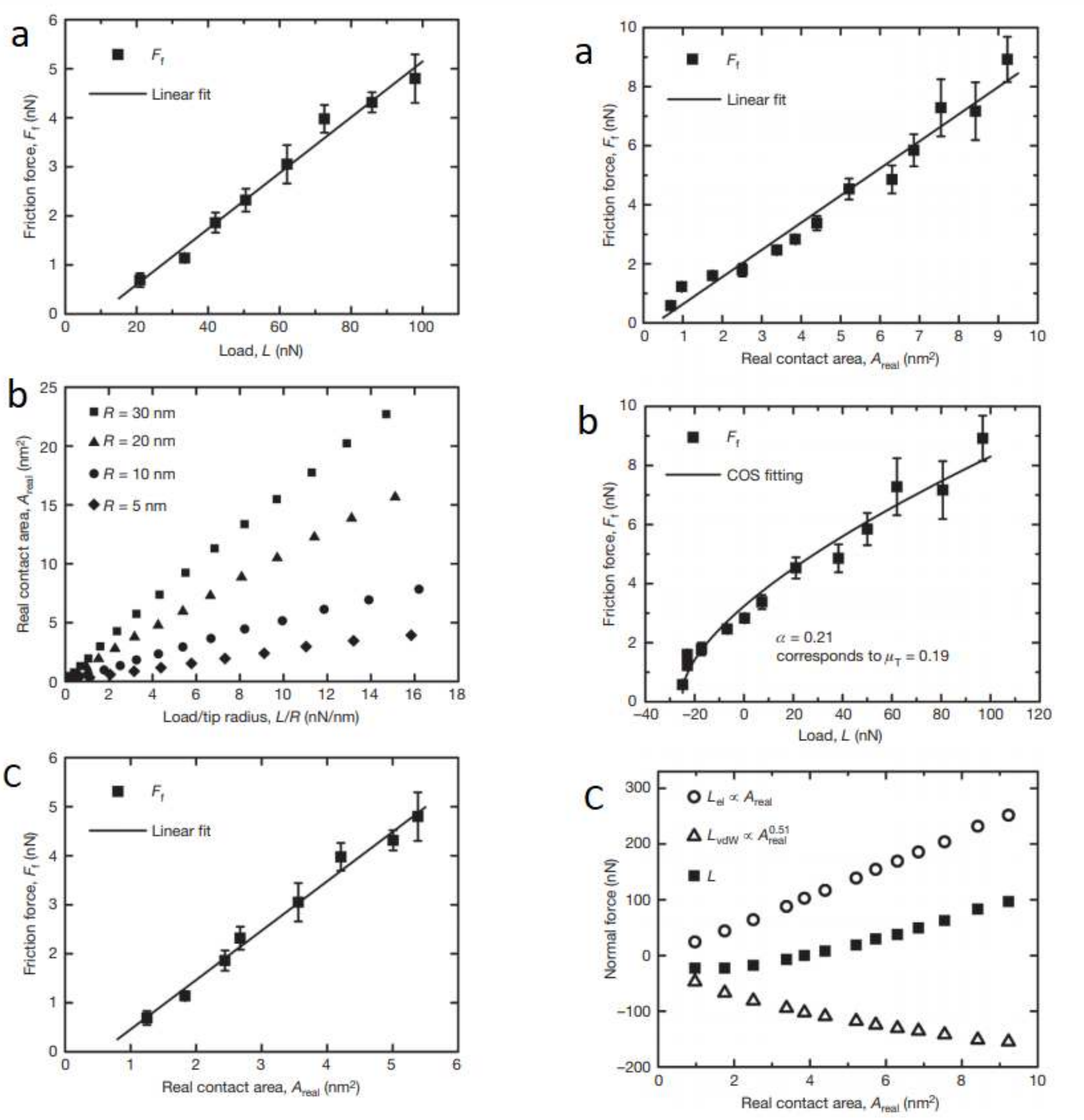

Figure 1.5: *Graph on the left-hand side is for non -adhesive contact* (a) friction force versus load, (b) real contact area versus load and (c) friction force versus contact area. *Graph on the right-hand side is for adhesive contacts (a)* friction force versus real contact area, (b) friction force versus load and (c) contribution to the total load as a function of real contact area: total load L (full squares); van der Waals contribution (empty triangles) and elastic restoring force (empty circles) [25].

However, unlike the non-adhesive case, the F_f is non-linear function of L (Fig 1.5b *on the right-hand side*). This non-linear behavior is due to the presence of adhesion forces L_{vw}, which for a spherical tip in contact with the flat sample surface do not scale linearly with the contact area (A_{real}) as shown in figure 1.5 c (open *triangles on the right-hand side*). As a result, total load $L = L_{el}\,(elastic\ restoring\ force\,) + L_{vw}(\,adhision\ force)$ is not proportional to $A_{real}$and hence $F_f\ = \tau A_{real}$ is a non-linear function of L.

A systematic investigation of the dependence of friction on the contact area was carried out recently for nano-sized metal clusters on graphite in ultraclean and atmospheric conditions [26-28]. Dietzel *et al* [26] and his research group performed experiments to understand the area dependence of friction state between two flat surfaces that are sliding past each other with ultralow resistance. They measured the sliding resistance of amorphous antimony and crystalline gold nanoparticles on crystalline graphite. For the amorphous particles, a square root relation between friction and the contact area is observed, while for crystalline gold particles they found a more complex scaling behavior related to variations in particles shape and orientation. Similarly, the effect of contact area on friction at nanoscale dimensions was experimentally studied by Sung *et al* [29] using glass balls of various radii against Si-wafer and diamond-like carbon (DLC) coated silicon film using Atomic force microscopy. Their findings suggested that the friction force at the nanoscale increases with the applied normal load and the tip size because of the increase in contact area, while the lower friction on DLC at the nanoscale compared to that of Si-wafer was attributed to the smaller contact area and the lower adhesive force, which are affected by the lower interfacial energy.

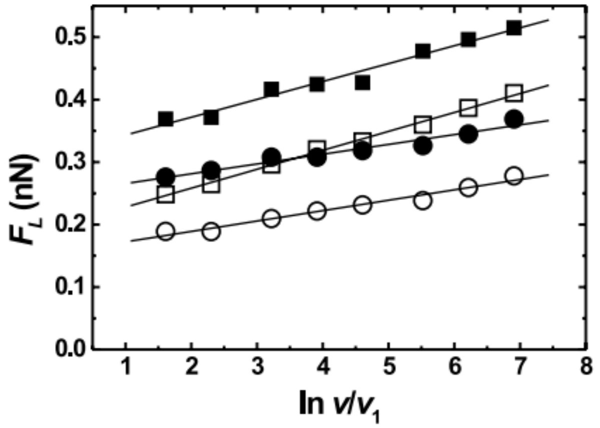

Figure 1.6: Friction as a function of the scanning velocity at F_N=0.44nN (circles) and F_N=0.65nN(squares) load. The experiments were performed with silicon tip on a NaCl (100) surface [30].

The sliding speed between contacts is another importance aspect in friction mechanisms at nanoscale dimensions [30-32]. Although there is a significant influence of the sliding speed in friction for bulk materials, only a few studies measuring its influence in friction on atomically thin layered materials have been reported [33-35]. The first measurements of the velocity dependence of atomic-scale friction have been reported by Gnecco *et al* [30]. The experiments were performed with a silicon tip on a NaCl (100) surface, using a homebuilt ultra-high vacuum (UHV) friction force microscope (FFM). The experimental data revealed the logarithmic dependence of the mean friction force at low velocities as shown in figure 1.6. The velocity dependence is due to thermal activation of the irreversible jumps between minima of the interaction potential.

Lately, researchers have looked at friction at the nanoscale level on the layered materials because of their unique physical and chemical properties. In particular, two dimensional (2D) materials such as graphene, hexagonal BN, and MoS_2 exhibit some of the lowest friction coefficient and wear rates, making them attractive for enhancing the efficiency, durability, and environmental compatibility of future mechanical systems. Graphene, which is a layer of carbon atoms, is extremely slippery material, which is why it has been added to lubricants over the years. The Prandtl-Thomlinson model remains one of the most popular models to described nanoscale friction in general [36]. One surprising result, not predicted by the Prandtl-Thomlinson model, is that friction is at its highest on single layer graphene sheet. In turn, as the number of layers of graphene increases, the level of friction decreases. Besides thickness dependence, friction on 2D materials often grows notably during initial sliding and then saturates after a certain sliding distance. This effect also depends on the sample thickness and more pronounced for thinner samples and diminishes for thicker samples. This results surprised Andersson and Wijn [37], and later they realized that the Prandtl-Thomlinson model required an additional variable that describes the deformation of the layered materials, since the original model only considered the force required to move a tip across a surface. The new model resolved some of the contradictory findings mentioned in research papers. Since 2D materials consist of only a few atomic layers, their mechanical, thermal, and electrical properties can be significantly altered by introducing topological defects, surface functionalization or substrate confinements. These effects inevitably add to the complexity of the frictional behavior of 2D materials. In the next section below, I have briefly reviewed relevant fundamental friction properties of graphene based on published papers cited here.

1.4: Contact Friction Force in Graphene:

Graphene being a two-dimensional material offers unique friction and wear properties that are not typically seen in conversational materials. Besides, because of the well-established thermal, electrical, optical, and mechanical properties of graphene, it can be considered as a solid or colloidal liquid lubricant. Its high chemical inertness, extreme strength, and easy shear capability are the major favorable attributes for tribological applications. Since it is ultrathin even with multilayers, it offers many applications in microelectron-mechanical systems and nanoelectromechanical systems with oscillation, rotating, and sliding contacts to reduce stiction, friction, and wear [38, 39]. However, despite many years of investigations, some of the fundamental properties of graphene are still not well-understood, including the way it behaves when something slides along its surface. Experimental results utilizing the scanning probe microscopies, including scanning tunneling microscopy (STM), atomic force microscopy (AFM) and lateral-force microscopy (LFM) as well as computational methods have revealed quite different results [38-40].

Friction of graphene is greatly affected by graphene-to- substrate adhesion and the number of graphene layers. The interaction with substrate is of relevance as graphene deposited on atomically thin materials has shown much lower friction than graphene deposited on silicon substrate [41]. Such interaction influences the surface roughness, diminishing it and lowering the friction forces. Lee et al [42] has reported the dependence of friction on the number of layers. They found that frictional force on graphene exfoliated onto SiO_2/Si substrate increases with decreasing graphene layers. They reported similar trends concerning the others 2D materials, including molybdenum disulphide (MoS_2), niobium diselenide, and hexagonal boron nitride. Low friction on these 2D layer materials is attributed to the weak interlayers bonding (van der Waals forces) compared with the strong interlayer chemical bonding of layered materials, making them easy to shear. Similarly, Egberts et al [43] reported that friction force of CVD grown monolayer graphene is significantly larger than that of bilayer graphene. The layers-dependent frictional properties result from puckering of the graphene sheet around the sliding tip and out of plane deformation. Thicker sheets are more rigid, and thus any effects of bending of the sheet should become smaller when the number of layers increases. For graphene film grown epitaxially on SiC substrates, the friction on monolayer graphene was found to be a factor two greater than that on bilayer films [40, 44]. The difference in friction is found to arise from the difference in electron-phonon coupling. Remarkable electron-phonon coupling in monolayer graphene dampens lattice vibrations and thus enhance the energy dissipation induced by friction. On the other hand, in bilayers of graphene, electron -phonon coupling almost vanishes, so friction is reduced as well. The crystallographic orientation of the graphene sample is also important, as energy dissipation along the armchair direction can be higher than along the zigzag direction for a monolayer graphene [45].

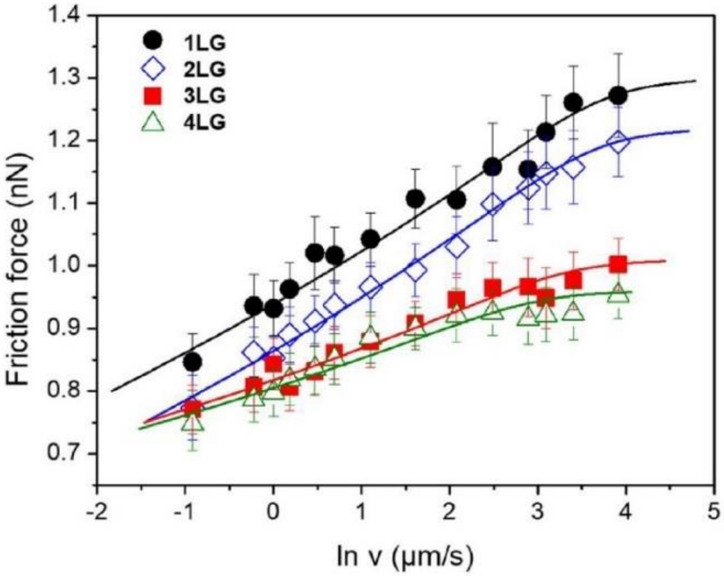

Figure 1.7: Measured friction force as a function of the logarithm of the scanning velocity for different graphene layers [46].

Relationship between the friction and velocity of the sliding object is influenced by the temperature and mechanical resonance of the systems in contact. They affect the probability of the atoms at contacts to jump between the minima of the interaction potential. Early studies on bulk crystal surface suggest a linear dependence of the friction force with the natural logarithm of the scanning velocity [30]. Later, it has been shown that this linear relation occurs until a critical saturation point and then friction becomes constant [47, 48]. Ptak et al [46] has shown the friction-velocity relation for different number of graphene layers as shown in figure1.7. For both monolayer and bilayer graphene, there is a significant linear increase of friction with the logarithm of the scanning velocity and the friction force reaches a critical point at high velocities, while for three-and four-layer graphene, the saturation occurs at lower velocities. Frictional saturation occurs when thermal energy is no longer assisting the tip to overcome the potential barrier between two potential minima. The reasons are not well explained by Ptak *et al* but other researchers [34] found that the act of sliding causes graphene atoms to make better contact with the object sliding alone on it; this increase in the quality of contact and as a result increases friction. The effect is strong for a single layer of graphene because it is more flexible than multilayers, so the atoms can move to location of better contact with the tip. Also , the friction-velocity curves as shown in figure 1.7, have a higher slopes than the curves for three-and four-layers , indicating that a more corrugated potential is involved in the friction process [47].

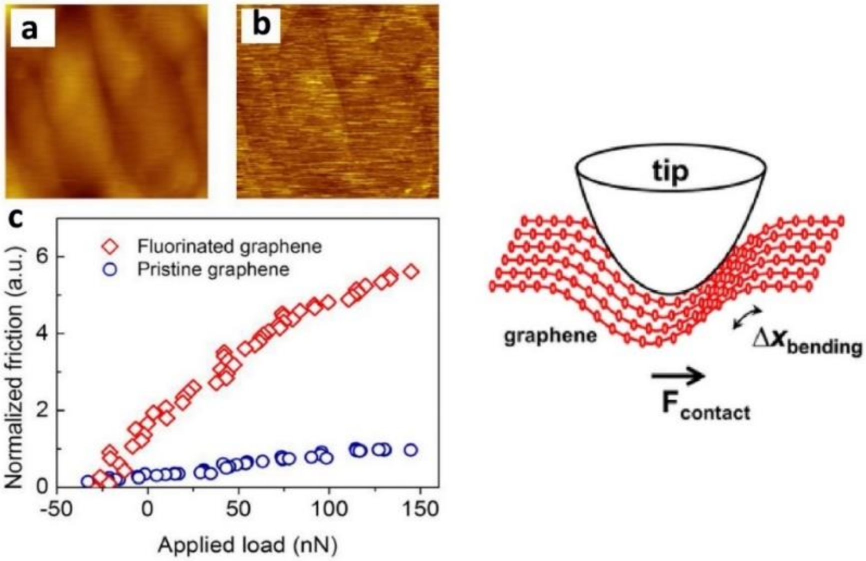

Figure 1.8: 500 x500 images of (a) topography and (b) friction measured on the fluorinated graphene using contact mode AFM. (c) Plot of friction force versus applied load measured on pristine and on fluorinated graphene [49].

Several experimental investigations have shown that friction on graphene can be altered by chemical modification of its surface by fluorine [49], hydrogen [50], and oxygen [51]. Results in Figure 1.8 show an example of the effect of fluorination on the frictional force of graphene. Chemical process mentioned above can generate both adsorption and vacancies. Many suggested mechanisms, such as increased surface roughness, enhanced interaction with the scanning probe, larger flexural phonon dissipation or the effects of add-atoms or functional groups might be the reasons for the increase in friction after chemical modification of graphene's surface. However, the effects of vacancies have not been sufficiently considered in the literature and so the reasons are still in debate. Motivated by all the facts described above, we have carried out research on contact friction in graphene and the results are presented in this dissertation.

1.5: Organization of the Dissertation:

The rest of the dissertation is organized as follows. In Chapter 2, experimental techniques to characterize graphene, and lateral friction force microcopy to measure nanoscale friction force are described. In Chapter 3, details of our modified graphene transfer methods to prepare good quality graphene samples are presented. This is followed by presentations of our results and their discussion in Chapter 4. Finally, in Chapter 5, a summary of major results of this dissertation are presented.

Chapter 2

Experimental Techniques for Characterization Graphene

2.1: Introduction:

In this chapter major spectroscopic and microscopic techniques for the characterization of graphene are reviewed. The primary goal of these characterizations is to distinguish graphene, graphene oxide, reduced graphene oxide and identify functional groups associated with them. The second goal of these characterization is to analyze the size, number of graphene layers and extent of defects. The spectroscopic methods are reviewed first, including X-ray photon electrons, infrared (IR) and Raman spectroscopy and X-ray diffraction (XRD). Among these, Raman spectroscopy stands out since it is recognized as the fingerprint technique to characterize graphene under ambient conditions.

Direct visualization of graphene on the substrate is possible using the microscopy instruments. Success and degree of exfoliation, number of layers, lateral size, atomic-level defects, and field emission characteristics have been studied using scanning tunneling microscopy (SEM), transmission electron microscopy (TEM), atomic force microscopy (AFM) and scanning tunneling electron microscopy (STEM). Among these state-of the art microscopy instruments, a brief review of atomic force microcopy (AFM) for topography images and lateral force microcopy (LFM) for fractional force measurement are presented relevant to this research project.

2.2: IR Spectroscopy:

Oxidation diminishes graphene's excellent conducting properties, so reduction of graphene oxide (GO) is desirable in order to partially restore its sp^2 network [52]. Reduced graphene oxide (RGO) can be produced through chemical [52, 53], microwave [54] , photothermal [55] and electrochemical methods [56, 57]. Infrared (IR) spectroscopy is a powerful method to evaluate the extent of functionalization of graphene, graphene oxide and chemically modified graphene.

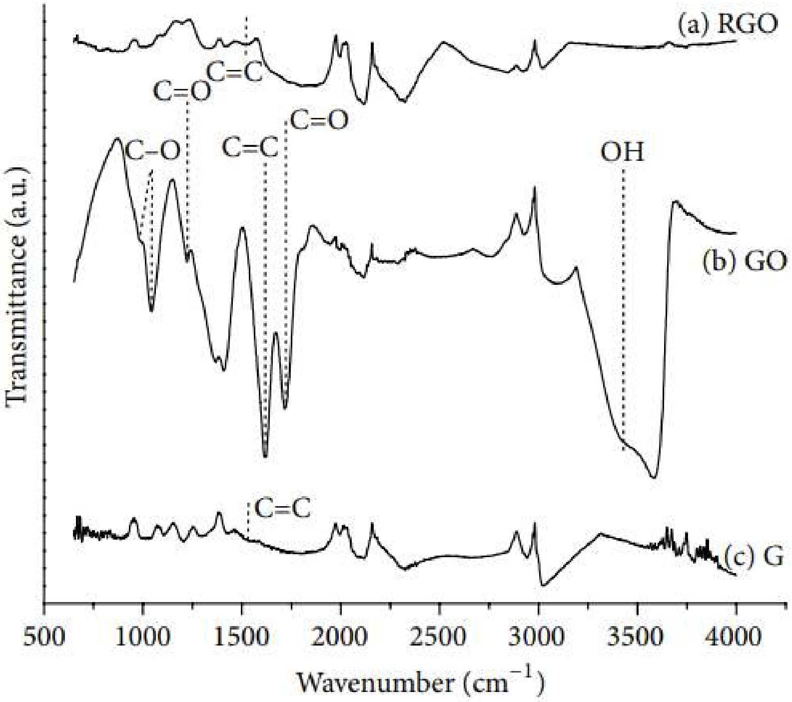

Figure 2.1. Infrared spectra of (a) reduced graphene (RGO), (b) graphene oxide (GO) and (c) pure graphite (G)[58].

Figure 2.1 shows infrared spectra of (a) reduced graphene, (b) graphene oxide, and (c) pure graphite. At ~1500-1600 cm^{-1} in -plane stretching vibration of sp^2 hybridized C=C is found. New bands appear for graphene oxide such as a signal at 3162 cm^{-1} corresponding to OH groups. At 1710 cm^{-1}, the stretching vibration of C=O related to carboxyl groups is found, where at 1220 cm^{-1} and 1050 cm^{-1}, the presence of epoxy and alkoxy group is observed, respectively. For reduced graphene oxide, most of the oxygen groups disappeared and the resulting spectra tends to be like the crystalline graphite spectrum. In comparison to Raman spectroscopy, IR spectra of graphene derivatives do not reveal electronic or atomic features of graphene. It may be difficult to distinguish between graphite and graphene with only trace amounts of functional groups by IR spectroscopy. However, using high energy x-rays, minor defects or oxidation are detected by x-ray photoelectron spectroscopy (XPS).

2.3: X-ray Photoelectron Spectroscopy (XPS):

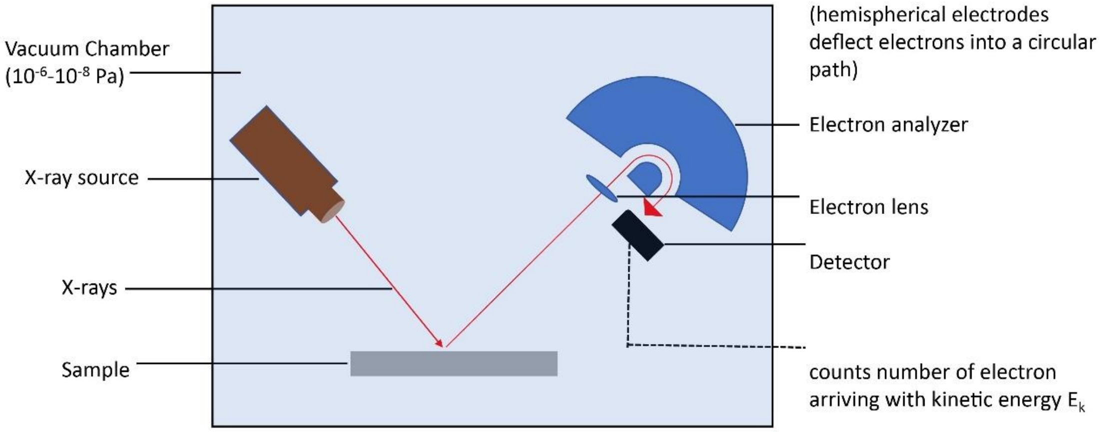

Figure 2.2. Basic components of a monochromatic XPS system.

X-ray photo-electron spectroscopy (XPS) is a quantitative technique for measuring the elemental composition of the surface of a material, chemical specificity (i.e., oxidation state) and thin film thickness. In XPS, surface analysis technique is based on energy -spectrum measurements of photoelectrons emitted from a material surface under irradiation with a monochromatic soft X-ray (200-2000 eV) radiation. Due to the short mean free path of electrons in condensed matter, XPS is particularly well suited for the measurements of films with thickness of up to 1-10nm [59]. As shown figure 2.2, the photoelectrons ejected from the surface of a specimen by the irradiating X-ray having a constant energy (E_{ph}), in vacuum (normally 10^{-7} Pa) are collected and analyzed. An XPS spectra is a plot of binding energy vs the number of electrons detected. Mathematically, binding energy is expressed as:

$$E_{ph} = E_k + E_B + \emptyset$$

$$E_B = E_{ph} - (E_K + \emptyset) \tag{2.1}$$

where E_B is the binding energy of electron to nucleus relative to the Fermi level, E_K is the kinetic energy of the electron and $\emptyset$ a work function of specimen, in the case of solid. E_K is measured my experiment and rest are known parameters. Hence, binding energy is calculated. Each electron in an element has characteristic binding energy and hence the value of E_B and chemical shift are utilized for identification of an element and estimation of its chemical bonding state in the specimen.

X-ray photoelectron spectra contain information about ionization energies of elements and, hence, it is used to determine the elemental composition, doping, defects, and oxidation of graphene with high accuracy. Binding energy of C1s electrons are usually detected around 285 eV and it is taken as reference for the measurement of chemical states of carbon compound. The table 2.1 shows the binding energies of common chemical states of carbon compounds with oxygen and are used to distinguish graphene from graphite, graphene oxide, or reduced graphene oxide.

Table 2.1: Binding energies of C1s in graphene derivatives [60].

Chemical State	**Binding energy (eV)**
C-C	284.8
C=C	283.4
C-O	285.5
O-C-O	286.5
C=O	289
O=C-O	288.5
C-H	285.3
C-N	283.7 (sp^3 N)
C=N	286.8
$\pi - \pi^*$ resonance	291.2

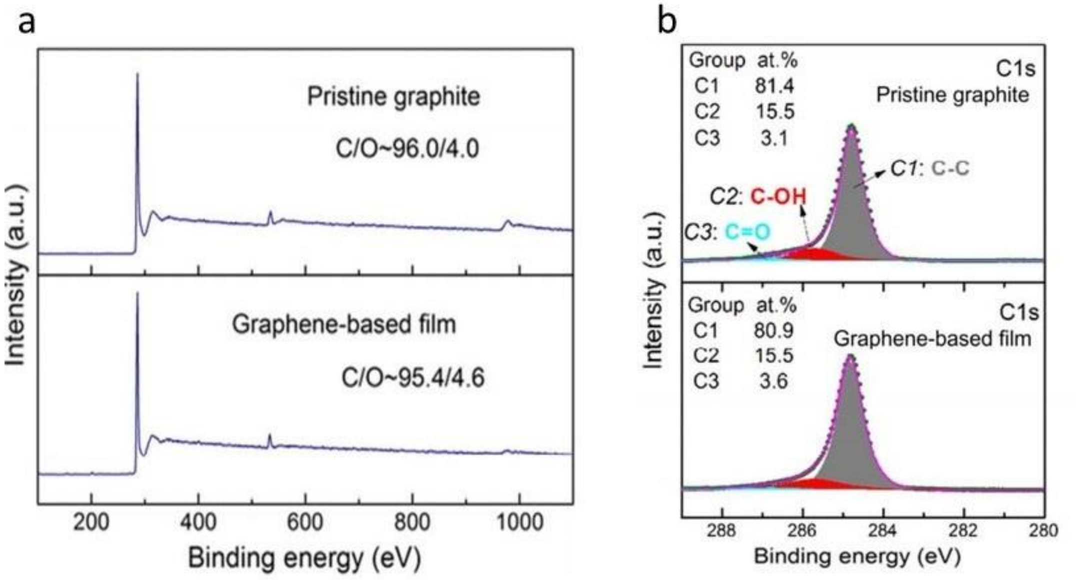

Figure 2.3: (a) XPS spectra of exfoliated graphene in comparison to that of graphite. (b) Identification of percentage composition of carbon bonding in the same sample where C1 is C-C, C2 is C-O and C3 is C=O carbon species [61].

Contamination of the graphene sample by hydrocarbons is the biggest challenge. Atmospheric hydrocarbons from solvents, pump oils, vacuum greases containing long -chain hydrocarbons are common contaminants in graphene. Figure 2.3 (a) shows the XPS spectra of graphene exfoliated in organic solvent in comparison to that of graphite, which shows the absence of significant oxidation of the sample during exfoliation. By considering the relative peaks and the areas enclosed by the peaks, we can determine the percentage of composition of carbon bonding in the sample [Fig 2.3 (b)]

2.4: Raman Spectroscopy:

Raman Spectroscopy is a nondestructive technique suitable for characterizing both laboratory and mass -produced samples, which brings out the atomic -scale information of the samples. Raman spectra can generally be measured from solids, liquids, and gases, including thin films and powders. Raman active bands in graphite (layers of graphene) are sensitive to the number of layers in a sample, types of defects, functionalization, doping concentration and orientation etc. [62]. In the absence of a band gap in graphene, all the incident wavelengths resonate, which has information about both atomic and electronic levels [63]. The peak positions, shape, and intensity of Raman bands of graphene vary with disorder, oxidation, doping and with the numbers of layers and those are valuable information to characterize the samples [62, 64].

Raman spectroscopy is the measurements of the shift in wavelength of the inelastically scattered radiation that provides the chemical and structural information. The phenomenon of inelastic scattering of light was first postulated by Smekal in 1923 [65] and first observed experimentally in 1928 by Raman and Krishnan [66]. Since then, the phenomenon has been referred to as Raman spectroscopy. The energy changes we detect in vibrational spectroscopy are those required to cause nuclear motion. If only electron cloud distortion is involved in scattering process; it is regarded as elastic scattering and there is no change in energy of the scattered photon. This is called Rayleigh scattering and it is a dominant process. However, if the nuclear motion is induced during the scattering process, energy will be transferred either from the incident photon to the molecules or from the molecules to the scattered photon. This is called Ramana scattering. It is a weak process in that only one in every 10^6-10^8 photons which scatter is Raman scatter. Hence, Raman shifted photons can be of either higher or lower energy, depending upon the vibrational state of the molecule under study. A simplified energy diagram that illustrates these concepts is shown in figure 2.4 below.

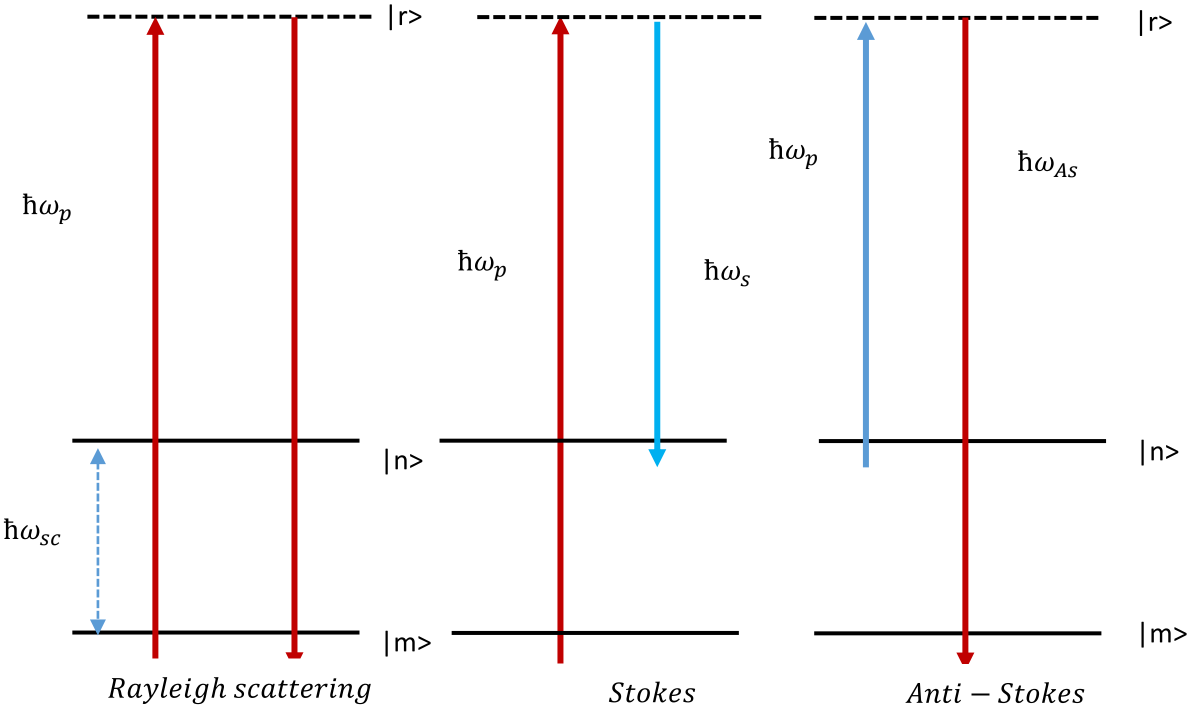

Figure 2.4: Energy diagram showing Raman scattering process.

The Raman scattering process from the ground vibrational state |m> leads to absorption of energy by molecules and its promotion to a higher energy excited vibrational state |n>. This is called Stokes scattering. On the other hand, due to thermal energy, some molecules may be present in an excited state |n> and scattering from these states to the ground state |m> is called anti-Stokes scattering and involves transfer of energy to the scattered photon. The relative intensities of the two process depend on the population of the various states of the molecules. At room temperature, the number of molecules expected to be in an excited vibrational state other than any really low energy ones will be small. Thus, compared to Stokes scattering, anti-Stokes scattering will be weak and will become weaker as the frequency of the vibration increases, due to decreased population of the excited vibrational states. Further, anti-Stokes scattering will increase relative to Stokes scattering as the temperature rises. The difference in intensities of Raman bands in Stokes and anti-Stokes can also be used to measure temperature of the sample [67].

Intense Raman scattering occurs from vibrations which cause a change in the polarizability of the electron cloud of the molecules. Usually, symmetry vibrations cause the largest change and produce the strongest scattering. Classical theory of Raman scattering can be described by considering oscillation induced dipole moment due to a source of electromagnetic radiation. The induced dipole moment can be expressed as,

$$\mu_{ind} = \alpha E + \frac{1}{2}\beta E^2 + \ldots. \qquad (2.2)$$

where α and β are the polarizability and hyperpolarizability constant and E is electric field of the electromagnetic wave. Neglecting the higher terms in equation (2.2), it can be written as,

$$\mu_{ind} = \alpha E_0 \cos(2\pi \nu_0 t) \qquad (2.3)$$

where $E_0$is the amplitude of electric field and ν_0 is the frequency of the incident light. The polarizability is a function of the instantaneous position of the constituent atoms. Let us consider dx is the physical displacement of the atoms about their equilibrium position due to vibration and it can be expressed as,

$$dx = x_0 \cos(2\pi \nu_m t) \qquad (2.4)$$

where, x_0 is the maximum displacement of the atom from its equilibrium position. Since the value x_0 is very small compared to the bond length; the polarizability may be approximated by Taylor series expansion

$$\alpha = \alpha_0 + \frac{d\alpha}{dx}|_{equ}\, dx$$

$$\alpha = \alpha_0 + \frac{d\alpha}{dx}\, x_0 \cos(2\pi \nu_m t) \qquad (2.5)$$

Now, equation (2.3) can be written as

$$\mu_{ind} = \quad [\alpha_0 + \frac{d\alpha}{dx}\, x_0 \cos(2\pi \nu_m\, t)\ ]\ [E_0 \cos(2\pi \nu_0\, t)]$$

$$\mu_{ind} = \quad \alpha_0 E_0 \cos(2\pi \nu_0\, t) + \frac{d\alpha}{dx}\, x_0 E_0 \cos(2\pi \nu_m\, t) \cos(2\pi \nu_0\, t)]$$

using a relation $\cos(A+B) + \cos(A-B) = 2cosAcosB$, we have

$$\mu_{ind} = \alpha_0 E_0 \underbrace{\cos(2\pi \nu_0\, t)}_{\text{Elastic scattering}} + (\frac{d\alpha}{dx}\,\frac{x_0 E_0}{2})\underbrace{[\cos(2\pi\{\nu_0 + \nu_m\}t) + cos(2\pi\{\nu_0 - \nu_m\}t)]}_{\text{inelastic scattering}} \qquad (2.6)$$

The equation (2.6) contains three frequencies and represent the three scattering events. (i) Rayleigh scattering (same frequency as that of the incident light) (ii) Stokes (reduced frequency) and (iii) anti-Stokes scatterings (increased in frequency).

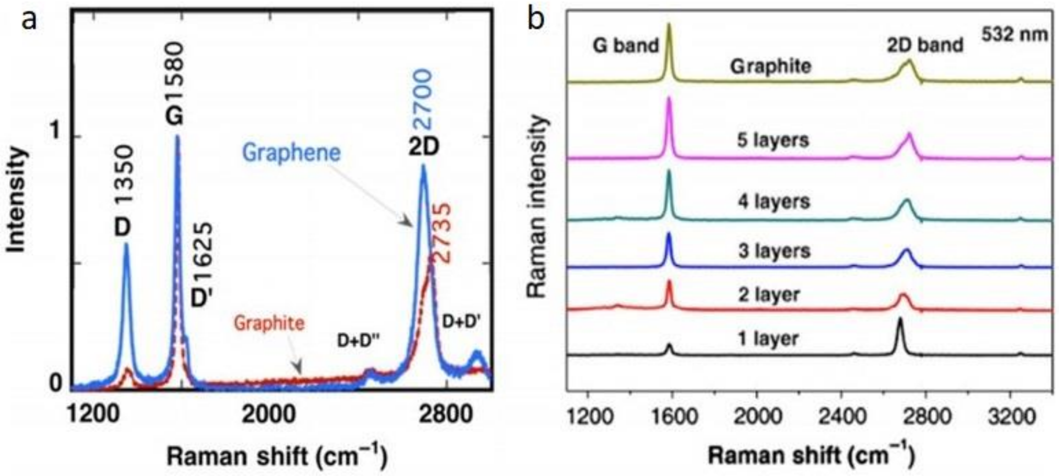

Figure 2.5: (a) Raman spectra of exfoliated monolayer graphene (solid line) and graphite (dotted line) [68]. (b) Raman spectra as a function of number of graphene layers [69].

The Raman spectra of graphene has three main peaks and several minor peaks which contains information about the structural and electronic properties. The most prominent Raman active band in graphene and other sp^2 carbon allotropes is the G band ~1580 cm^{-1} [Fig 2.5 (a)], which arises due to the C-C in -plane vibrations (stretching mode). The D band (~ 1350 cm^{-1}) is due to the disordered carbons arises from the breathing vibrations of six-atom ring [62]. The

D band in graphene is activated only by defects or disorders, and thus, the ratio of the D to the G band intensities (I_D/I_G) is used as to determine the level of defects in graphene samples [70]. The 2D band at ~2700 cm $^{-1}$, does not require defect activation and thus present in graphene and graphite as well. As the number of graphene stakes in graphene increases to few-layer graphene, the 2D band gets broader, shorter, and shifts to lower wave numbers [Fig. 2.5 (b)] due to change in the electronic environment resulting from interactions between the adjacent layers [71].

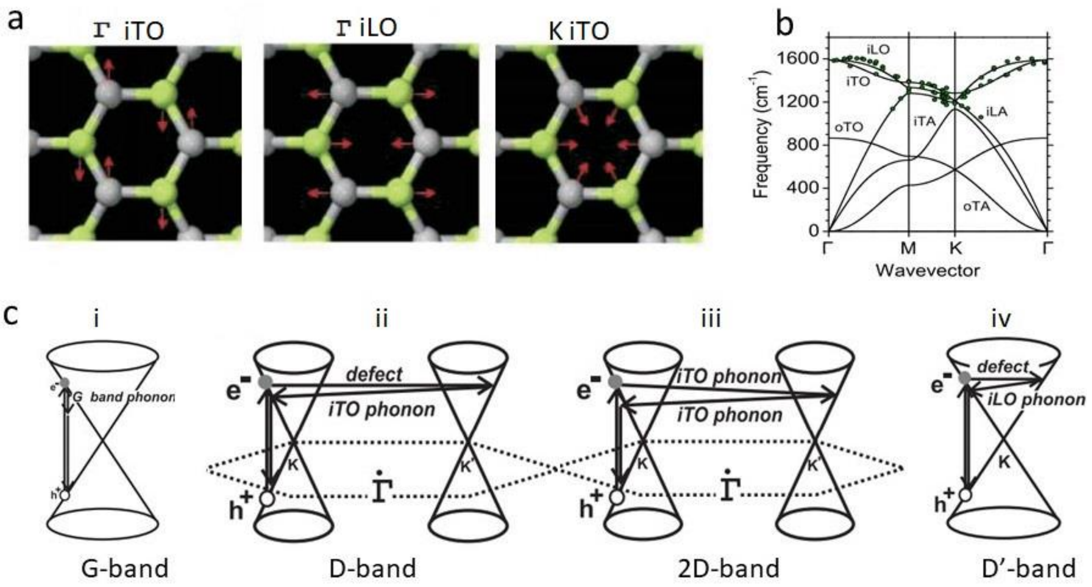

Figure 2.6: (a) Three in -plane phonon modes at Γ and K point in graphene. (b) Phonon dispersion relation of graphene. (c) (i) First -order Raman process which gives rise to the G band, (ii) intervalley D band and (iv) intravalley D' band. (iii) two -phonon second order Raman spectral processes giving rise to the 2D band in graphene.

Since the unit cell of monolayer graphene contains two carbon atoms, there are six phonon dispersion bands [Fig 2.6 (b)], in which three are acoustic (A) and other three are optic (O) phonon modes. For one acoustic (A) and one optic (O) phonon branches, the atomic vibrations are perpendicular to the graphene plane, and they correspond to the out -of plane (o) phonon modes. For two acoustic and two optic phonon branches, the vibrations are in-plane (i). Therefore, along the high symmetry ΓM and ΓK directions, the six phonon dispersion curves are assigned to LO, iTO, oTO, LA, iTA and oTA phonon modes. For visual illustration, figure 2.5 (a) shows the three in-plane phonon modes at Γ and K point in graphene.

The G-band is associated with the doubly degenerate (iTO and LO) phonon mode at the Brillouin zone center. In fact, G -band is the only band coming from a normal first order Raman scattering process in graphene system. The process giving rise to the G-band is shown in figure [2.6 c) i]. On the other hand, the 2D and D-bands originate from a second -order process, involving two iTO phonons near K point for the 2D band or one iTO phonon and one defect in the case of the D-band. The double -resonance process shown in figure [2.6 c) ii] and figure [2.5 c) iii] begins with an electron of wavevector **k** measured from the K point absorbing a photon of energy E_L (L represents laser). The electron is inelastically scattered by a phonon of wave vector **q** and energy E_{phonon} to a point belonging to a circle around the K' point, with momentum **k'.** The electron scatters then back to the **k** state and emits a photon by recombining with a hole. In the case of D band, the two scattering processes consist of one elastic scattering event by defects of the crystal and one inelastic scattering event by emitting or absorbing a phonon, as shown in figure [2.6 c) ii]. In the case of 2D-band, both processes are inelastic scattering events involving two phonons. This double resonance mechanism is also called an inter-valley process because it connects points in circles around inequivalent K and K' points in the first Brillouin zone of graphene. The double resonance process responsible for the D' band is an intra-valley process, since it connects two points belonging to the same circle around the K point (or K' point). For graphene, the G band frequency is known to be insensitive to the change in the energy of incident laser light (E_L), where D and 2D bands exhibit a dispersive behavior i.e., their frequencies in the Raman spectra changes as a function of the energy of the incident laser.

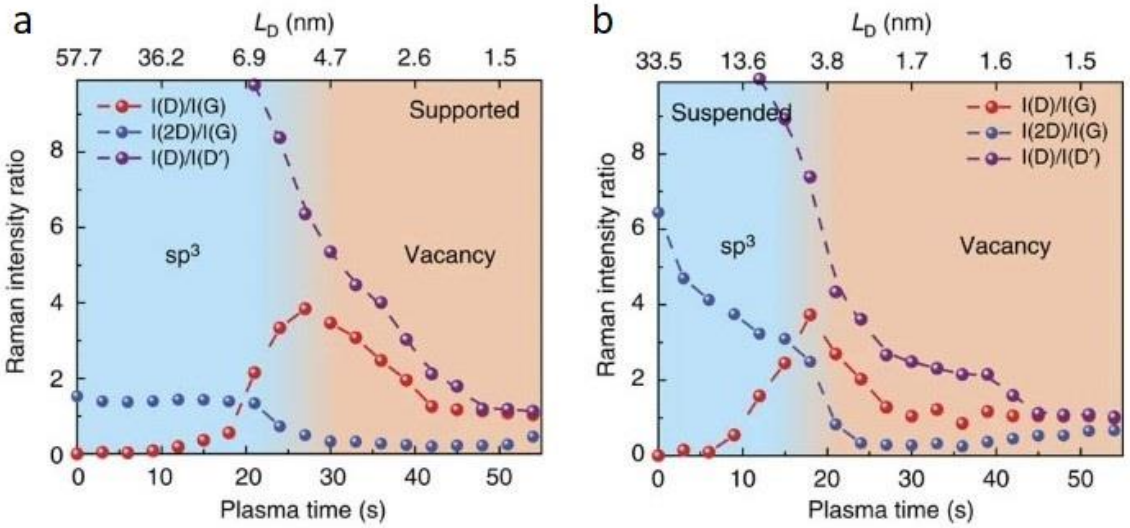

Figure 2.7: Raman peak intensity ratios of (a) graphene supported on SiO_2/Si substrate and (b) suspended graphene samples as a function of plasma exposure time [72].

Quantifying defects in graphene related systems, which include a large family of sp^2 carbon structure, is very important to understand the fundamental properties of graphene and its applications. Raman intensities and peaks ratio are useful information to determine the type of defects and doping level in graphene. For example, upon exfoliation of graphite, the defects peak intensities increase as more edges and vacancies are formed during exfoliation. The I_D/I_G ratio of highly defective graphene oxide is usually above 1, while those of the exfoliated graphene derivatives range from 0.1 to 0.6 [60]. Zandiatashbar *et al* [72] quantitatively examined the type and density of defects in the graphene sheet using Raman spectroscopy. They repeatedly exposed the graphene samples to oxygen plasma with 3s periods and then characterized by Raman spectroscopy after each plasma exposure dose. The peak intensity ratio of D-G peaks (I_D/I_G), 2D-G peaks (I_{2D}/I_G) and D-D' ($I_D/I_{D'}$) for monolayer graphene supported on the SiO_2/Si are shown in figure 2.7 (a). The I_D/I_G) increases with plasma exposure time until it reaches a maximum value of ~4 and then decreases. On the other hand (I_{2D}/I_G) exhibited a slow decrease at the initial stage and then sharp drop around 20s; such behaviors are also reported for the defective graphene in the literature [73-75]. Although the peak intensity ratio [Fig 2.7 (b)] of the suspended graphene shows different values for the same oxygen plasma exposure doses, they follow the similar trend. The differences in Raman spectra between supported and suspended graphene sheets may be attributed to the substrate effect on

Raman intensity in the supported graphene[76], presence of pre-stress [77] and etching of both sides [78] in the suspended graphene.

The lateral size of the graphene is correlated with the intensity of the G band (I_G) and D band (I_D), which need to be normalized with I_D/I_G value of graphite. The empirical formula to determine the lateral size of graphene is [79] :

$$< L >= \frac{k}{(I_D/I_G)_{Graphene} - I_D/I_G)_{Graphite}} \tag{2.7}$$

Where k= 0.17, measured experimentally [79].

Similarly, using the ratio of 2D peak of graphene and its shoulder peak, the number of layers of the exfoliated graphene is established with respect to the graphite. Exfoliation of graphene results in change in peak position of the 2D band to lower wave numbers by about 30 cm $^{-1}$, when compared to that of graphite. These changes are dependents with the number of graphene layers in flakes. The number of layers of the exfoliated graphene is calculated using the relation below [79]:

$$< N_G >= 10^{0.84M+0.45M^2} \quad \text{with M} = \frac{(I_{2D}/I_{2Ds})_{Graphene}}{(I_{2D}/I_{2Ds})_{Graphite}} \tag{2.8}$$

where , I_{2D} is the intensity of the 2D peak and I_{2Ds} is the intensity of the 2D shoulder peak in graphene or graphite.

Experimental considerations: Although Raman spectra contains a large amount of information, there are few limitations and possible error from the measurements, and it is worth mentioning for practical application.

a. While preparing and transferring graphene to a substrate, restacking, or folding of the sheets can occur, which results in overestimation of the numbers of layers.
b. During the spectral acquisition, some samples are prone to photoreduction (graphene oxide), which may give the wrong information. Reducing laser power eliminates this effect as well as prevent sample damage.

2.5: X-Ray Diffraction (XRD):

X-ray diffraction is a non -destructive technique used for the identification of various crystalline phases and their crystallite size present in a material. It can also provide information on structures, preferred crystal orientation, and other structural paraments, such as average grain size and strain distribution. The analysis of the XRD pattern is based on the Bragg law and mathematically it can be expressed as; $2d\ sin\theta = n\lambda$, where d is the spacing between the (hkl) plane, n is the order of diffraction, θ is the Bragg angle and λ is the wavelength of the incident x-ray. X-ray beam are chosen because their wavelength is similar to the spacing between the atoms in the sample, so the angle of diffraction will be affected by the spacing of the atoms in the crystal. The result of x-ray diffraction plots the intensity of the signal for various angles of diffraction at their respective two-theta (deg) positions. The two-theta (2θ) positions correspond to a certain spacing between the crystals or atoms in the samples, determined by the angle of diffraction from the incident x-ray beam sent into the sample. The area under the peak is related to the number of molecules in that phase and the ratio of the areas under these lines are used to determine the relative percentage of the phases or composition of elements in the given sample. In addition, the width of the peaks is inversely proportional to the crystallite size. Bulk samples produce narrow linewidths in XRD spectra whereas the linewidth increases with decrease in the crystallite size to nm dimensions. The Scherrer equation $D = \frac{0.89\lambda}{\beta \cos\theta}$ is often used to estimate the crystallite size D from the linewidth β at a Bragg angle θ using x-rays of wavelength λ. Consequently, in a non-crystalline(amorphous) material only a very broad line is observed.

In the literatures, the use of XRD in the field of graphene research have been mentioned mainly for the studies of graphene oxide , reduced graphene oxide [80], determination of crystallite size, number of graphene layers, interlayer spacing , and defect density [81] . In the recent reports, Seehra *et al.* [82, 83] have highlighted the importance of XRD to identity the phases in multilayer graphene and for the first time quantified the 2H and 3R phases in graphene-based materials by analyzing X-ray diffraction (XRD) patterns. The presence of 3R structure is important since unlike the 2H structure, the 3R phase is a semiconductor with a band gap of 6meV [84, 85]. The presence of a tunable bandgap is essential for many applications of these materials. Nowadays graphene-based materials are available from commercial sources and it is important to characterize the properties of these commercial samples for their quality and applications purpose.

Graphene is simply one atomic layer of graphite -a layer of sp^2 bonded carbon atoms arranged in hexagonal lattice. Graphite is a commonly found mineral and is composed of series of stacked parallel layers planes. It is expected that the adjacent graphene layers in graphite are bound by the weaker van der Waals forces. The spacing between the layer planes is relatively large (3.36 A^0) or more than twice the spacing between the atoms (1.42A^0) within the basal plane. The stacking of these layer planes occurs in two slightly different ways; hexagonal (2H) and rhombohedral (3R) structures. In the 2H graphite structure, which is the most commonly occurring structure, the carbon atoms are in the -ABABAB- sequence, in other word, carbon atoms in every other layer are superimposed over each other as shown in figure 2.8 (a). In the 3R structure, the stacking sequence is …ABCABC.., where the C layer are shifted by the same distance with respect to the B layers, as the B layers are shifted with respect to the A layers [Fig 2.8 (b)]. The 2H phase in graphite is thermodynamically more stable at normal temperature and pressure than the 3R phase [86, 87]. Due to small energy differences between the 2H and 3R structure under normal conditions, it is difficult to distinguish between the two phases electrochemically [86].

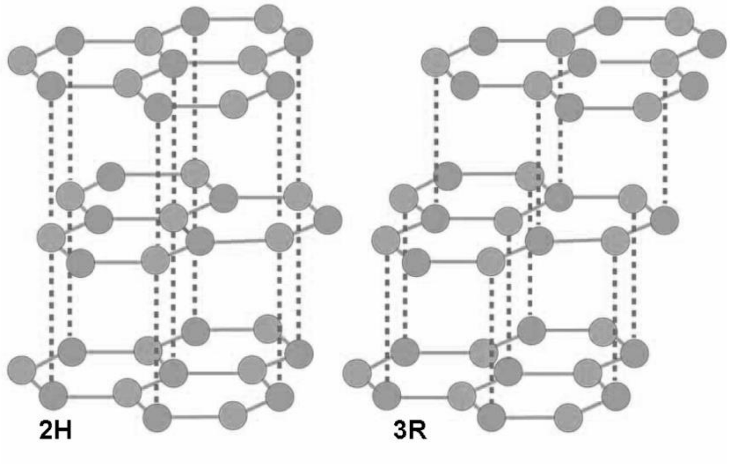

Figure 2.8: (a) hexagonal 2H, and (b) rhombohedral 3R structures in graphite [82].

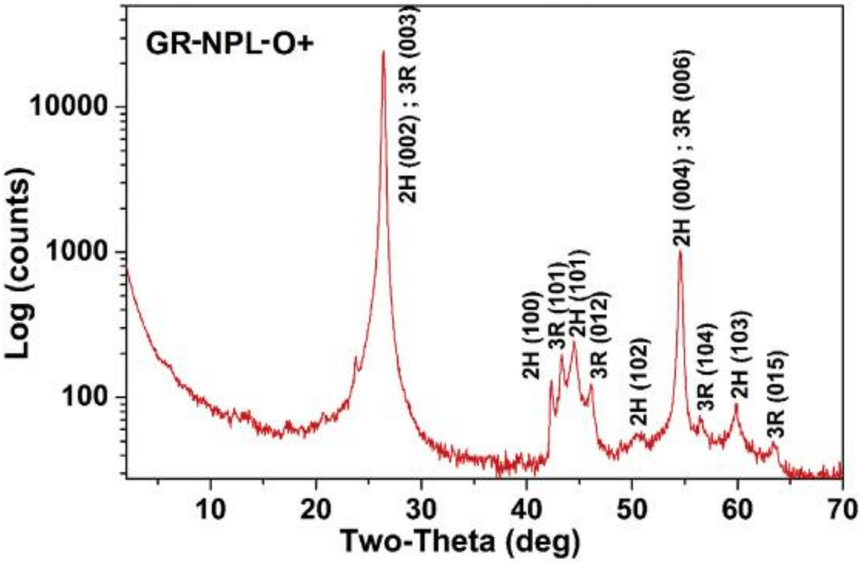

Figure 2.9: X-ray diffraction pattern of a multilayer graphene sample [82].

Figure 2.9 shows the x-ray diffraction pattern of a commercially available graphene-based nanomaterial (Graphene nanoplates grade 4, 99% O+ rich, which is labeled as GR-NPL-O+ in the figure 2.9). The Miller indices of the observed lines for the 2H and 3R phases as labelled in the figure 2.9 are based on the International Center for Diffraction Data (ICDD). The (002) line from the 2H phase at 2θ ~26.38^0 and (003) line from the 3R phase at 2θ ~26.60^0 respectively, are not distinguishable. However, four sharp peaks that are visible in between $2\theta = 42^0$ and 47^0 indicate the presence of both 2H and 3R phases in the given samples. The 2H (100) and 2H (101) peaks are clearly separated. Similarly, the 3R (101) and 3R (012) peaks are very noticeable and their relative intensities are comparable with those of 2H peaks. Based on the distinct features in the XRD patterns along with Raman spectroscopy, Seehra *et al* [82, 83] have classified the commercial graphene-based materials into three group: (i) graphitic nanosheet exhibiting both 2H and 3R phases, (ii) graphene oxide (GO) or carbons with some disorder, and (iii) disordered carbons. The classification and quantification of both the 2H and 3R phases in graphene-based materials by analyzing the XRD pattern are the important results for the research community.

2.6: Atomic Force Microscopy (AFM):

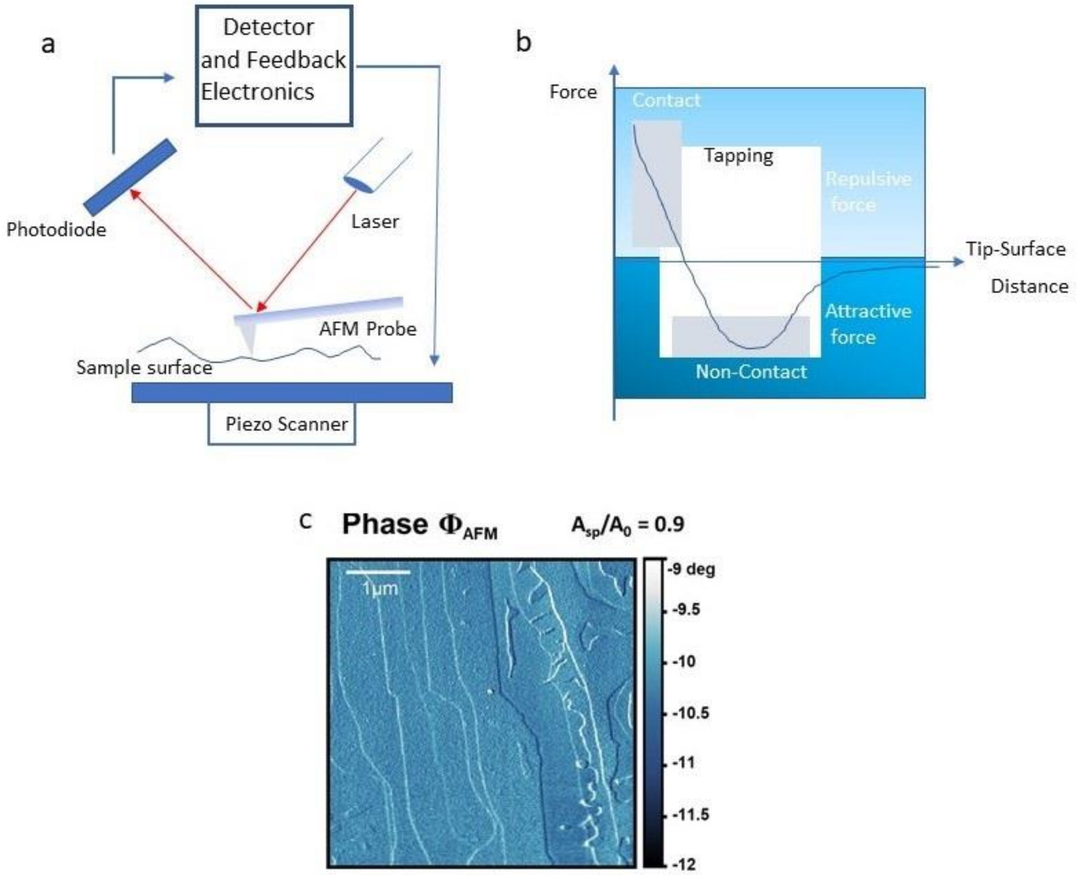

Figure 2.10: a) A schematic diagram of a standard AFM system with optical feedback. (b) Operation regions for contact, tapping and non-contact mode. (c) AFM phase image of the epitaxial graphene sample obtained for free oscillation amplitude $A_0 = 17\ nm$ and amplitude oscillation ratio $\frac{A_{sp}}{A_0} = 0.9$ [88].

Atomic force microscopy (AFM), also called scanning probe microscopy, scans the surface with a flexible cantilever with a pointed tip, making very small and precise movements. AFM was developed in 1986 and initially operated in a contact mode, i.e., with the tip of the cantilever touching and being deflected from the surface of the sample. Resolution of the AFM depends on the diameter of the cantilever. Smaller the diameter of the tip, higher is the resolution. AFM has wide applications and as it has become one of the leading methods for surface characterization, cantilevers of various types of materials and shapes have been developed to suit different application. Most common type of cantilevers are made up of silicon, carbon, silicon nitride (for biological and in-fluid measurements), wear-resistant diamond etc. Conducting coating such as metal (platinum), metal carbide or polycrystalline diamond can be added on the tip of the cantilever, and it allows electrostatic force measurements. Interaction force between the tip and the sample deflects the cantilever. Mathematically, this force (F) is given by:

$$F = cZ$$

where c is force constant and Z is the deflection of the cantilever. Depending the types of materials, the possible forces responsible for this bending are mechanical contact force, van del Waals forces, capillary forces, chemical bonding, electrostatic forces, magnetic forces etc. [89]. The deflection of the cantilever is measured from a reflection of laser from the top surface of the cantilever into a quadrant photodetector (QPD) as shown in the figure 2.8 (a). The sample is mounted on a Piezoelectric scanner which can move in x, y and z directions. The feedback loop applied between the detector and the sample stage adjusts the tip-to-sample distance to maintain a constant force between the tip and the sample surface. Common operation regions for contact, tapping and non-contact mode of AFM are shown in figure 2.8 (b) and are described in a brief in the section below.

Contact mode: In this mode, as name suggests, the tip is in contact with the sample surface all the time. The forces between the AFM tip and the surface are repulsive [Fig 2.8 (b)]. As the tip scans the sample surface, the cantilever bends depending on the surface topography. The most common configuration of contact mode is to operate it in constant force or deflection feedback mode. The cantilever deflection is the feedback parameter. It is set by the user and is related to how hard the tip pushes against the surface so that the user controls how gentle or aggressive the interaction between the probe and the sample is. Contact mode can be useful especially for robust samples in air that can handle the high loads and torsional forces exerted by the cantilever, but also, surprisingly useful for the delicate samples like graphene as long as the force can be controlled below 100 pN (pico- Newton) [90].

AC mode**:** It is also known as non-contact mode, developed a year later of contact mode. In this mode tip does touch the sample surface and cantilever oscillates at the resonant frequency. During the scanning procedure, interactions between the tip and sample surface will modulate the amplitude, phase, and the frequency of the cantilever's vibration. Those changes are measured with a lock-in amplifier and processed as a topography image. The advantage of non-contact mode is that it offers the lowest possible interaction between the tip and the sample surface. Small interaction forces help preserve AFM tip sharpness and achieve high resolution. AFM cantilevers with high force constant and high resonance frequencies are most suitable for non -contact mode.

Tapping mode: The most popular mode nowadays is the tapping mode (introduced in 1993), in which the cantilever oscillates at high frequency at or close to resonance and gently taps the surface during oscillation, improving the resolution. In tapping mode, amplitude modulation mode is the most common AFM imaging mode in which amplitude of the oscillation is the feedback parameter. The cantilever is generally driven with a shaker piezo and starts vibrating at the excitation frequency. By sweeping the frequency across a suitable range, the peak in the frequency spectrum that corresponds to the resonance frequency of the cantilever can be found. Due to the small size of the cantilever, typical resonance frequencies are in the range of kilohertz and even in Megahertz range. As the cantilever is brought closer to the sample surface, the amplitude of the oscillation is reduced due to interaction between the cantilever and sample. This amplitude reduction is the source of the feedback; the user sets an amplitude based on the type of interaction that is desired. The user should consider these three parameters to obtain high resolution images: (i) Cantilever spring constant – the stiffness of the lever must be appropriately suited to image the material. If the cantilever is too stiff, the result may be destructive to the sample or cause tip wear. On the other hand, if the cantilever is too soft, it may not be able to interact with the sample to generate any contrast or it stays in contact with the surface. (ii) Cantilever resonance amplitude- this parameter is set in the unit of volts and for a rough sample surface need a larger free vibration amplitude. (iii) Set point- this is the reduced target amplitude and is expressed as percentage of the free vibration amplitude. Lower set points will favor a more aggressive tip-sample interaction of a more repulsive tip-sample interaction.

In tapping mode, phase contrast imaging is also one of the most common AFM imaging methods to obtain contrast based on material properties. An excited cantilever oscillation will exhibit a phase shift (ϕ) between the drive and the response, as defined by the equation:

$$d = Asin(2\pi ft + \phi), \tag{2.9}$$

where d = deflection; A = amplitude; f = frequency and ϕ = phase shift.

When the interaction between an oscillating cantilever and sample changes, the resonance frequency of the cantilever will shift. It will shift to lower frequencies for attractive force while to the higher frequencies for repulsive force. Consequently, the phase at a fixed frequency shifts when the cantilever-sample interaction changes, for example when the material properties changes; this is the reason that phase is a common imaging mode when contrast based on materials properties are desired. However, the challenge with the phase is that it will shift due to multiple properties of material, such as adhesion, stiffness, dissipation, and viscoelasticity. Thus, while phase is very useful imaging method, it can be difficult to interpret the contrast with respect to individual material properties. An example of phase image of epitaxial graphene sample is shown in figure 2.8 (c). It is possible to observe some terraces with a clear different height with significant contrast with AFM phase image.

Besides imaging surface topography, AFM has a wide range of applications; for examples, it can be used to probe electrical and magnetic properties of materials. These methods operate either in contact mode or tapping mode, depending on the information being sought. For electrical properties, it requires specialized tips, usually in the form of a conventional silicon cantilever coated with an electrically conducting coating (gold or platinum). Similarly, in magnetic force imaging, the magnetic forces acting on a sharp, magnetized tip by the sample are measured. AFM can also be used to measure frictional force between the cantilever and samples. For experimental investigations of contact friction in monolayer and bilayers graphene presented in this dissertation, lateral force microscopy (LFM) is used, and a brief description of its operation principal is presented below.

Lateral Force Microscopy (LFM): Most AFM instruments can also function in the lateral force mode; this is sometimes known as the frictional mode. The essential feature of this method is that the AFM is operated and controlled in the conventional contact mode, but that torsional deformations of the cantilever are monitored by sensors orthogonal to those that generate the signal for the AFM control loop. By measuring the lateral bending of the cantilever, information regarding the surface friction characteristic of a sample can be determined. Lateral forces can arise from changes in the frictional coefficient of a region on the sample surface or from onsets of changes in height.

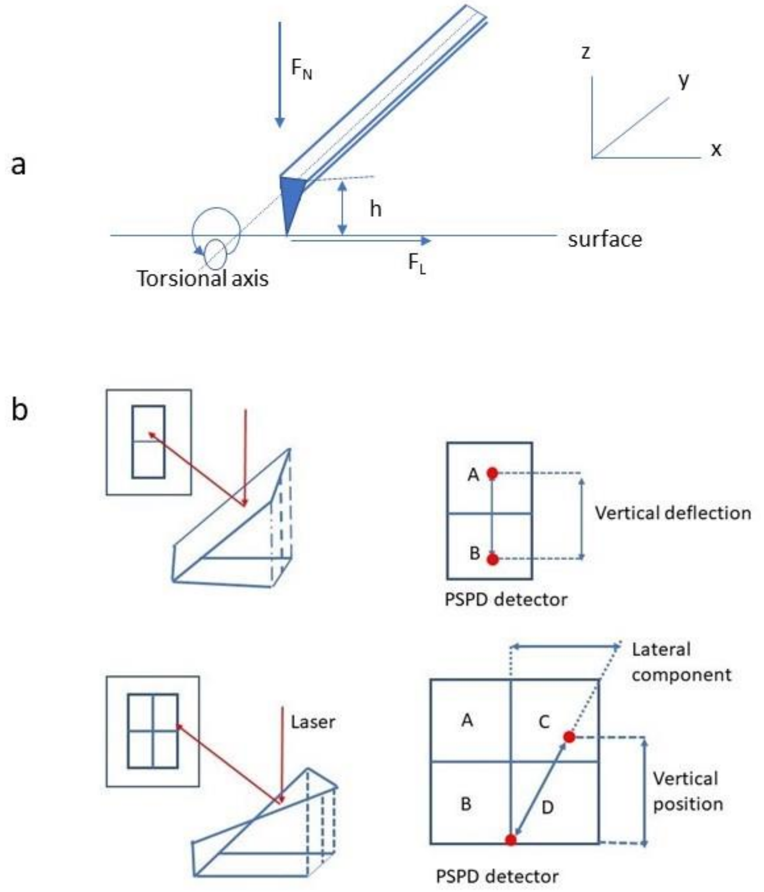

Figure 2.11: The principal elements of the LFM system. (a) The normal force, F_N, is applied by the lever with normal spring constant k_N and transmitted through the tip to the surface. The tip is travelling along the x axis, and subjected to a lateral force, F_L, which causes a torsional deformation. (b) Schematic illustration of laser position on photodetector (PSPD) in the operation of LFM.

Lateral force microscopy system [Fig. 2.9 (a)] are characterized by the following quantities and relationships [91]:

$$F_L = \mu(F_N + F_N^{inter}) \tag{2.10}$$

where, F_L is the lateral force, F_N is the normal force as sensed by the cantilever, and F_N^{inter} is the additional normal force due to net attractive interactions between tip and surface, and μ is a coefficient of dynamic friction. The normal force can be expressed as,

$$F_N = k_N \Delta z \tag{2.11}$$

where, k_N is the normal spring constant (in the range 10^{-2} to 10^{2} Nm^{-1}), and Δz is the deflection of the free end of the cantilever along the z direction when loaded. Similarly, lateral force is

$$F_L = k_L \Delta x \tag{2.12}$$

where, k_L is the lateral spring constant of the cantilever, which is related to torsional spring constant and the height of the tip, h. The deflection of the tip at the point of contact from its vertical position is Δx . The angle of rotation of the cantilever at the position of the tip will be Δx/h. Disregarding the static friction regime, the dynamic coefficient of friction is then,

$$\mu = F_L/(F_N + F_N^{inter}) \tag{2.13}$$

if $F_N^{inter} << F_L$, then the $\mu = (k_L/ k_N) (\Delta x/ \Delta z)$ (2.14)

Figure 2.9 (b) shows schematic illustration of laser position on position sensitive photodetector (PSPD), which is made up of four compartments known as a quad-cell. In order to acquire topographical details of surface (deflection of the cantilever in vertical plane i.e., Δz), bi-cell signal in relation to the difference between the cells on top (A+C) and the bottom cells (B+D) recorded from the quadrant detector is needed.

$$Topographic\ information = (A + C) - (B + D)$$

In contrast, to obtain the surface frictional properties (deflection of cantilever in the horizonal plane i.e., Δx), the signal is taken from the difference between the right cells (A+B) and the left cells (C+D).

$$Frictional\ information = (A + B) - (C + D)$$

The lateral voltage signal read by the photodiode is linearly proportional on the lateral force on the probe, allowing for a least-squares fit to obtain a conversion factor between lateral force and voltage.

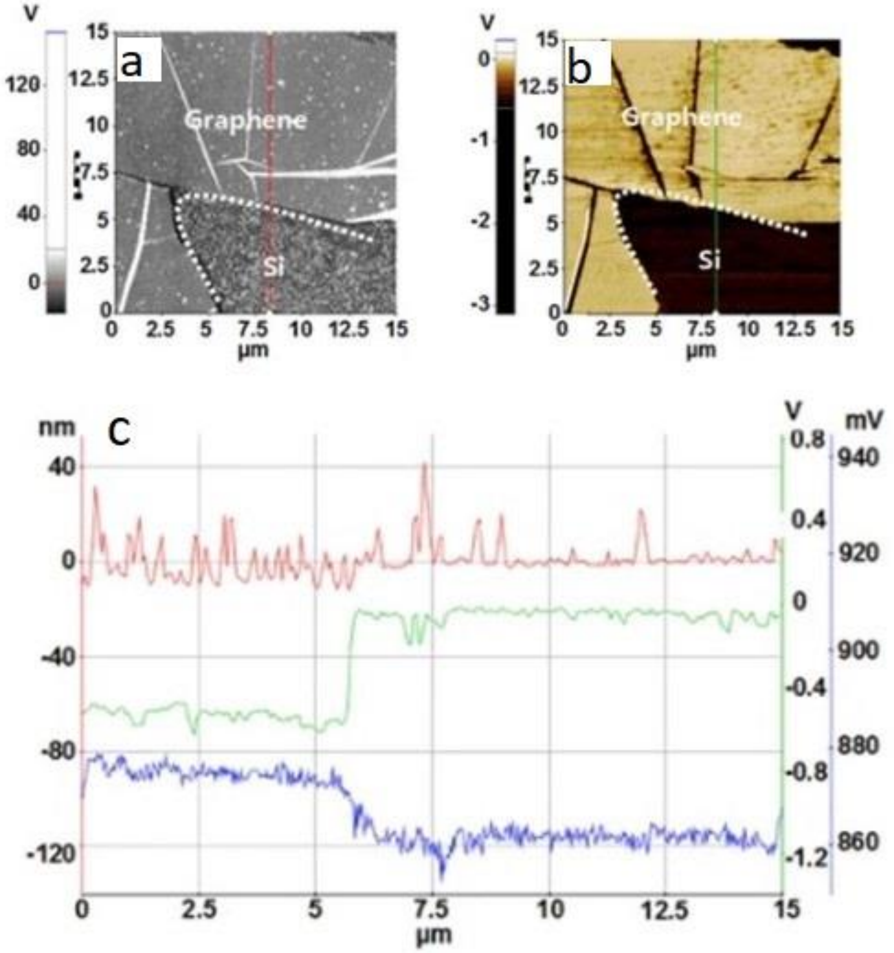

Figure 2.12: (a) AFM topography image of graphene on Si. (b) Lateral force microscopy image to measure friction on graphene/Si and Si substrate. (c) Line profiles along red line seen in (a) and green line seen in (b) showing the frictional forces.

Figure 2.12 (a) represents AFM topography image of graphene on Si. The boundary between graphene and Si, as indicated by the white dashed line, is discernable. The redline shown in figure 2.10 (c) is the heigh profile of the sample and Δz ~ 5 nm was measured between the graphene and Si. From the lateral force microscopy image in figure 2.12 (b), the two materials were clearly differentiated. From the green line profile [Fig 2.12 (c)] of the LFM signal, a large frictional coefficient was observed for Si compared to that of graphene, as evident by the downward shift in the LFM signal over Si as compared to that over the graphene.

2.7: Conclusions:

As research on graphene-based materials has been growing rapidly in recent years, new characterization techniques to enhance the current and classical methods may be needed to ensure the quality and reproducibility of these measurements. One of the major goals of examining graphene and its derivatives is to clearly separate graphene from graphene oxide and reduced graphene and then explore the corresponding electronic and transport properties. One of the best ways to identify the high-quality graphene is by Raman spectroscopy. In our experience, at a first glance, the Raman intensity ratio of I_D/I_G might be helpful to identify the quality of graphene as the I_D/I_G value is directly proportional to the extent of defects/ oxidation level.

Apart from the Raman spectroscopy, a major microscopy image must also be made to better characterize the quality and nature of the graphene produced by a given method, prior to any further study and application of the given preparation. Transmission electron microscope (TEM) and atomic force microscope (AFM) data are the complementary to Raman analysis, which provide information about defect density, lateral size and number of layers present in the flakes. However, the microscopy methods alone cannot distinguish graphene from its oxide derivatives or functional groups unless coupled with methods such as x-ray photoelectron spectroscopy (XPS), energy dispersive x-ray spectroscopy (EDX) and IR spectroscopy. Recent studies have added the important of X-ray diffraction (XRD) to quantify the 2H and 3R phases in multilayered graphene.

With the new cutting-edge technologies, AFM can be used for a wide range of applications. We used later force microscopy (AFM in contact mode with lateral scanning) to investigate the friction properties on monolayer and bilayer graphene.

Chapter 3

Development of Frame-assisted Graphene Transfer Methods

3.1: Introduction:

In this chapter, development of a simple but an effective frame -assisted graphene transfer method is described, and experimental results are compared with those obtained with a regular graphene transfer process. In a regular transfer process, a thin layer of poly- methyl methacrylate (PMMA), a supportive layer, is spin-coated onto the graphene surface, and the metal below is etched away completely. Copper foils, a substrate used in chemical vapor deposition (CVD) of graphene, have an irregular surface and graphene follows the surface morphology of the underlying copper during the growth process, making adhesion of transfer materials to the graphene film a challenging process. We addressed this issue by electropolishing copper foil (25µm thick, Alfa Aesar) before the synthesis of single layer graphene. The resulting graphene was characterized using atomic force microcopy (AFM) and Raman spectroscopy measurements and our results showed a clean graphene film having less wrinkles and crack free with low sheet resistance.

3.2: Synthesis of Single Layer Graphene by CVD:

Graphene can be synthesized by many techniques such as mechanical exfoliation [92, 93], electrochemical exfoliation [94], chemical vapor deposition (CVD) [95], epitaxial growth on silicon carbide (SiC) [96] and other methods like unzipping nanotubes and pyrolysis of sodium ethoxide [97]. Mechanical exfoliation is time -consuming process that yields relatively small samples. Among these methods, the most promising way to synthesis graphene is CVD because it can produce high-quality graphene at low cost in a large scale and fulfill the demand of graphene.

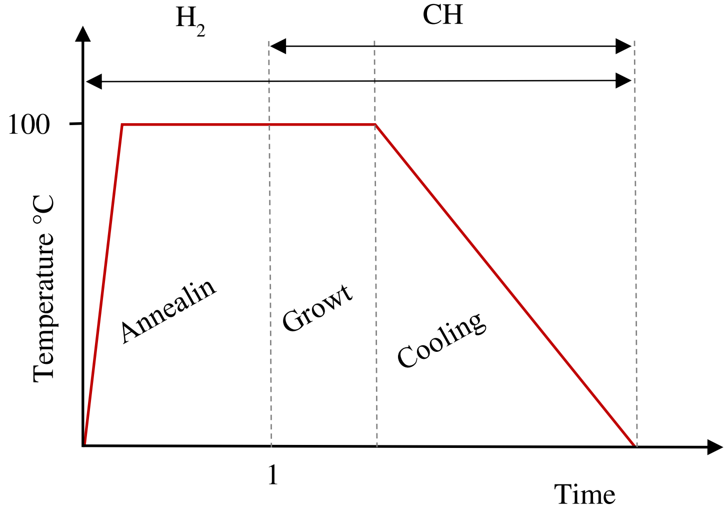

Figure 3.1: Summary of CVD grown graphene.

Copper foil (25 µm thick, Alfa Aesar, item No.46365) was used for CVD growth of graphene. Cu foil was cut into approximately 1.5 cm × 6 cm strips and treated with electropolishing (EP). In brief, copper foil is electrolyzed at a voltage range between 2-5 V for 60 s in phosphoric acid solution (500 ml of deionized water, 250 ml of phosphoric acid, 250 ml ethanol, 50 ml isopropyl alcohol, and 5 g of urea). Only polished anode copper foil was used for graphene growth. After EP treatment, anode copper foil was rinsed with deionized water and blow-dried with a nitrogen gun. Electropolished copper foil was then inserted into a 1-inch-diameter fused quartz tube furnace and pumped down to ~50 mTorr. The tube was back filled with $H_{2(g)}$ (~100 mTorr) and annealed for 1 h at 1000 °C. After annealing, $CH_{4(g)}$ (~500 mTorr) was introduced for 30 min (growth) while H_2 flow and temperature during the growth were kept the same. After the growth step, furnace was rapidly cooled to room temperature with the same gas flow growth step for both H_2 and CH_4. The graphene samples are stored in container filled with nitrogen.

3.3: Transfer Methods:

The first step necessary in fabricating devices from CVD-grown graphene is transfer of graphene from a metal growth substrate onto a desired substrate. Poor graphene transfer process could alter the intrinsic properties of graphene inducing cracks, wrinkles and folding. Various researchers have developed different transfer methods such as mechanical exfoliation [98], polymer-assisted transfer [99-101] and continuous transfer by a roll-to roll process [102, 103]. All the transfer processes mentioned above involve the use of chemicals. Depending upon the need, transfer process is carried out either in dry or wet conditions. Hence the graphene transfer process is divided into two types i.e. dry and wet transfer process. Some novel techniques used in dry transfer method involve direct delamination of graphene from a metal substrate [104]. It eliminates the need for the conventional metal etching process and as a result there is no risk of physical damage to the graphene film by surface tension of etchant solution. Ren *et al* [105] reported that direct transfer method does not degrade the graphene structure and does not produce extra doping in graphene; in contrast PMMA-based transfers (wet transfer) have strong n-doping. Others have proposed clean and effective dry graphene transfer process by: electrochemical etching [106] of copper substrate, and mild heat and pressure assisted mechanical peeling [107]. Martins and co-workers [108] have developed transfer of graphene onto flexible bulk substrates *via* lamination while Milan *et al* [109] has reported a dry transfer method using PDMS as a stamping polymer and a polyisobutylene (PTB) layer as the graphene-support polymer. This approach is beneficial to transfer graphene onto hydrophobic substrates.

Although there are different aforementioned methods to transfer graphene, some methods follow multiple steps and are time consuming; while others need excess of chemicals, cleaning process, depositing chemicals, and polymer residues on the graphene surface and as a result degrade the quality of graphene. So, people are still exploring a clean graphene transfer process for graphene-based device fabrication. Below, we have discussed and compared the results with our proposed graphene transfer method with the most common one.

3.3.1: Regular transfer method

Regular graphene transfers i.e., Poly (methyl methacrylate) (PMMA)-coated transfer process is one of the most common methods of graphene transfer mentioned in literatures [110-113]. However, challenges remain in yielding a clean and high-quality graphene. Schematic diagram to transfer graphene by this method is shown in figure 3.2(a). We cut a rectangular CVD grown graphene of size 1cm x 1cm and graphene on the back of copper foil was removed by oxygen plasma (RF Power of oxygen 100W for 60 s). We used 950 PMMA A_4 (950,000 molecular weight and 4% in anisole) as a supportive layer. To better spin coat the PMMA on the surface of graphene we performed 3 steps spin coating with parameters as shown in table 3.1 and then baked the sample at 80^0C for 10 mins at room temperature. Further, the sample was left overnight in vacuum to dry it completely. We recommended slow baking of PMMA/ graphene about $\leq 80^0$ C, otherwise, longer baking time at higher temperature (150^0 C >) leads the PMMA layer hardening and later it would be more difficult to remove the PMMA by chemicals.

Steps	Speed (rpm)	Time t (s)
1	100	6
2	500	30
3	3000	45

Table 3.1: Spin coat parameters of PMMA.

In the chemical etching process, Cu foil was etched by ammonium persulfate solution [$(NH_4)_2S_2O_8$] having concentration of 6.9 grams/150 ml of DI water, for 6 hours. The copper and heavy metal residues were settled at the bottom while the sample (PMMA/graphene) remained floating on etchant solution. The residues were cleaned with continuous flow of DI water for 2-3 hours.

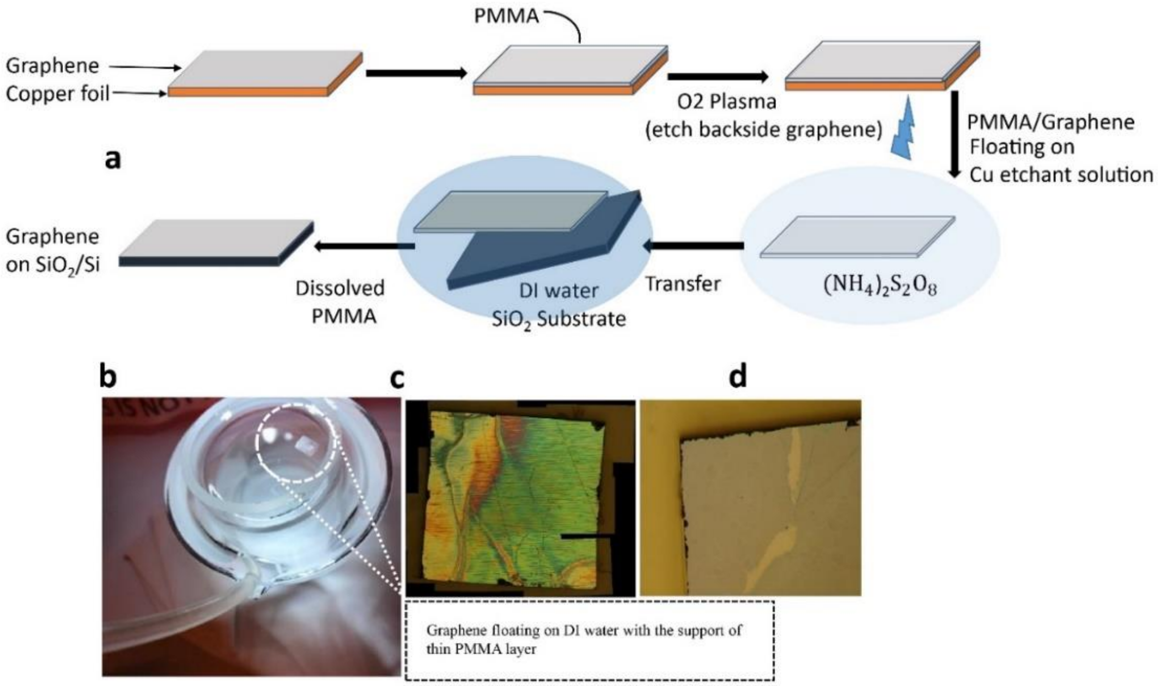

Figure 3.2: (a) Schematic diagram showing a regular graphene transfer process. Optical images of (b) graphene floating on DI water, (c) PMMA/graphene just after transfer on SiO_2/Si substrate and (d) graphene on SiO_2/Si after the removal of photoresist.

The target substrate (SiO_2/Si) was cleaned using the following procedure: First, it was sonicated in acetone for 10 mins, followed by sonication in isopropyl alcohol (5 mins). After this procedure, the target substrate was further rinsed by IPA to remove the acetone residues in ambient temperature and dried using a nitrogen gun and graphene was transferred manually. After transfer, the sample (PMMA/graphene/substrate) was cured by the following steps: first, gently blew with nitrogen gun for 10s to improve the contact between the layers and then gradually heated up to 100^0 C (about 30 mins) to evaporate the trapped water. To make better adhesion of the graphene with the substrate, the sample was kept into vacuum overnight. Finally, the sacrificial layer i.e. PMMA was removed from the graphene surface using the following chemical treatments:

1-soaked in warm acetone (50^0 C) for 1 hr.

2-sokaed in isopropanol alcohol (IPA) for 1 hr.

3- annealed the sample at 200^0C in Argon atmosphere for 2hrs.

4-finally soaked in acetone for 20mins, rinsed by IPA and made dry with nitrogen gun.

3.3.2: PMMA- frame assisted transfer method

This is a modified technique we developed for transferring chemical vapor grown graphene (CVD). In this method instead of spin coating the PMMA, we prepared PMMA gel and applied it to make a frame on the edges of graphene / copper sample as shown in figure 3.3 (a). To make thick PMMA gel like substance, we baked the 950 PMMA A_4 gradually from 50^0 C- 80^0 C for 10 mins and then immediately cooled it down by DI water. The thick PMMA acts like a gel, was then applied by Q-tip with the help of optical microscope on the edges of Graphene/copper and the frame then gradually heated up to 100^0 C for 10 mins to make it harder. With care, the sample was gently laid on the surface of $(NH_4)_2S_2O_8$ aqueous etchant solution (6.9 grams/ 150 ml DI water) mixed with few drops of isopropanol alcohol (IPA). The usage of IPA was to control the surface tension, as the surface tension of IPA (21.7 dyn/cm) is lower than that of water (72 dyn/cm) [114]. If there was no thin layer of isopropanol below the graphene film, the atomic thin layer graphene could turn apart due to the surface tension of etchant solution after graphene detached from Cu film. The role of PMMA frame is to minimize the external force from ambient or solution and it prevents the graphene from mechanical degradation i.e. folding or tearing during the transfer process. We designed a 3D stage for the precise movements of the substrate and used it for controlled transfer.

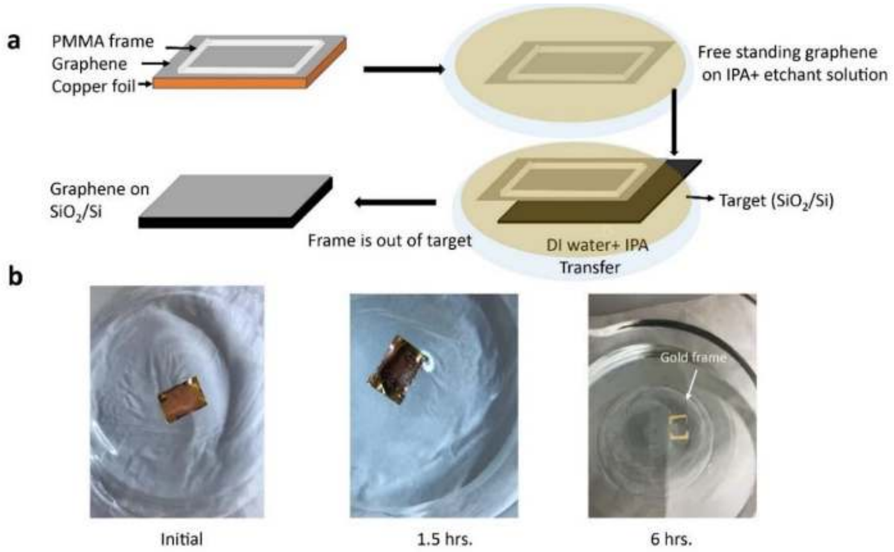

Figure 3.3: (a) Schematic diagram of PMMA-frame assisted transfer process (b) Optical images of graphene/ copper at the interface of hexane and copper etchant solution in a gold - frame method.

3.3.3: Gold- frame assisted polymer free transfer method

Though, PMMA-frame assisted transfer process minimized the PMMA residues (discussed in section 3.4), often the frame hits the substrate edges during manual transfer process and polymer residues get contaminated on the graphene surface after its chemical treatments. To address this issue, we made a thin gold frame (10nm) by e-beam evaporation instead of PMMA gel and followed a polymer-free biphasic (liquid/ liquid) approach [115] for the transfer of monolayer CVD grown graphene to a wide range of target substrates. As shown in figure 3.3 (b), a nonpolar hexane solution was gently added with the help of pipette on the top surface of copper etchant solution after 1.5 hours. Hexane is an inert nonpolar molecule having low viscosity. It is immiscible to copper etchant solution so that the graphene/Cu sample was trapped at the organic/aqueous biphasic interface, with the gold -frame on graphene in contact only with the hexane and Cu foil exposed to the bottom etchant solution. Due to lack of heteroatoms and aromatic groups in hexane, as well as its volatility and rapid evaporation nature, no residues are left on the graphene surface and there is no doping after transfer onto the desired substrate [115]. After enough etching time (6 hours), only CVD grown monolayer graphene sheet remained trapped at the interface of liquids with the support of gold frame (Fig.

3.3c). To minimize any possible contamination from etchant salts produced, we made a continuous flow of DI water for about 2 hours and finally the free-standing graphene sheet was scooped out from the interface by use of any substrate of interest with the help of 3D stage. The surface tension for hexane/ water interface is ca. 45 mN.m^{-1} [114, 116], lower than that of the air/water interface and as a result free standing graphene sheet did not pull apart. The gold frame played a significant role to make free standing graphene sheet visible at the interface of liquids, otherwise transfer would be impossible. Further, the gold-frame minimized external force around the graphene from ambient or solution making it more stable in liquids interface.

3.4: Results and Discussion:

Atomic force microscopy (AFM) is a well-suited technique for a quantitative analysis of residual impurities on the graphene surface. We used Asylum MFP-3D AFM in contact mode for topography images. Figure 3.4 (a-d) compares the surface morphology of regular transfer graphene with those obtained with frame assisted-transfers. Transferred graphene on SiO_2/Si substrates (in all methods) have an excellent surface uniformity. Less significant structural defects such as hole, cracks and fold are observed. This is achieved by our careful and slow baking approach for the removal of water trapped at the graphene/ SiO2 interfere as well as sequential drying process that we applied for PMMA/graphene sample for better contact with the substrate. Some darker lines visible in AFM topography images (Fig. 3.4 a-d) are wrinkles. Some of these wrinkles could be generated during the CVD growth and few others were produced during the transfer process. We did not notice any significant change in those wrinkles after annealing the sample in argon atmosphere at 200^{0}C for 2 hours. Though the results are satisfactory, a supportive polymer i.e. PMMA that we used in regular graphene transfer process produced scattered residues (Fig. 3.4a).

Annealing might be an easy solution to remove polymer contaminants on graphene but annealing graphene sample in air (in the presence of oxygen) results in defect formation if the annealing time is longer (> 3hrs) at temperature above 200^0 C [117]. So, we annealed the samples to burn off the PMMA residues at 200^0 C in argon atmosphere for 2 hrs. AFM topography image of annealed sample (Figure 3.4 b) showed a satisfactory result with less defect density of polymers (PMMA). The average rms surface roughness of the graphene samples were 2.2 nm, 1.51 nm, 0.7 nm, and 0.5 nm respectively for the samples shown in figure 3.4 (a-d). Comparatively the larger rms value of the PMMA coated samples suggest that graphene films are rough due to the remaining high density PMMA residues particles, considering the rms roughness of the SiO_2/Si substrate is smaller than 1nm. On the other hand, lower average rms values for the frame-assisted transfer methods indicate less defects transfer.

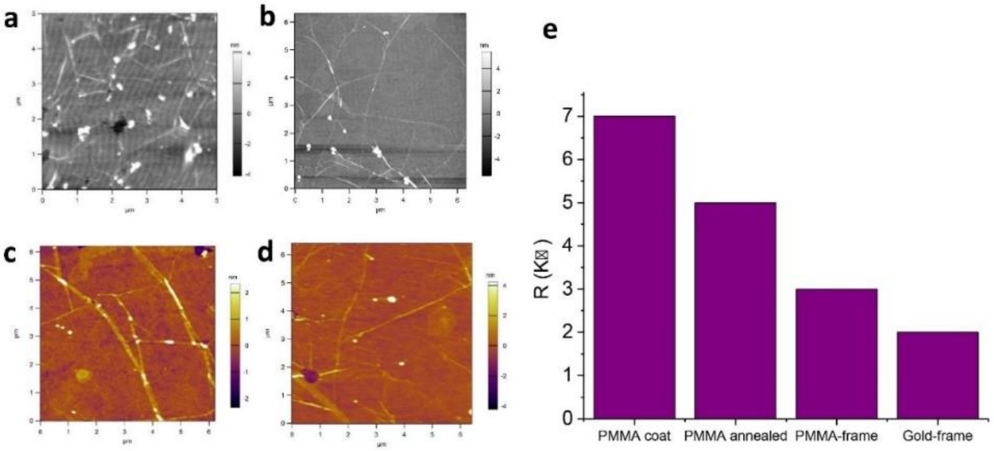

Figure 3.4: AFM topography images of graphene before (a) and after (b) annealing (regular transfer). The annealing was done at 200^0C in argon atmosphere. Similarly, AFM topography images of graphene transferred on SiO2/Si substrate by (c) PMMA-frame assisted and (d) gold frame polymer free biphasic methods. (e) Bar diagram to compare two -probes contact resistance of graphene.

Figure 3.4 (e) shows a comparison of two probes contact resistance of monolayer graphene transferred on SiO_2/Si substrate by different methods. Two probe contact resistance of the PMMA coated transferred graphene before annealing was in the range of 5-7 **KΩ**. The resistance decreased by about 30% with annealing at 200^0C, implying improved electrical properties due to reduced surface contamination on graphene. Our result is similar to the reports by Cheng *et al* [111] and Pirkle *et al* [113], where they have demonstrated increase in mobility of annealed samples at low temperature regime due to reduced surface contamination on graphene surface. On the other hand, it has been reported that annealing at higher temperature (400^0C >) caused heavy-hole doping and serious degradation of carrier mobilities in graphene devices [111]. Possible reasons for the increment of resistance are due to scattering of electrons by hardened polymer residues and chemisorption on graphene.

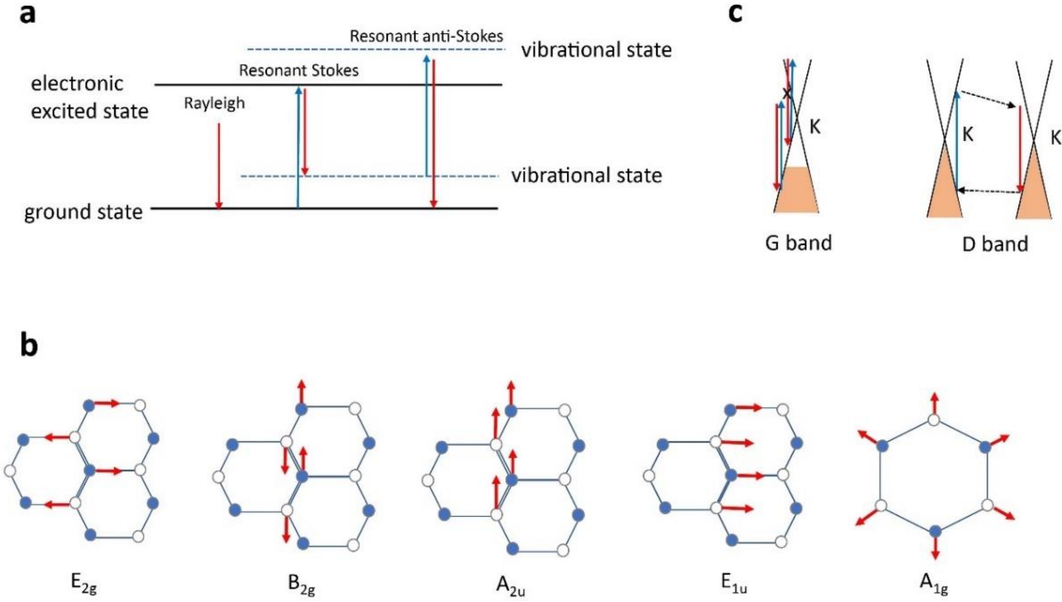

Figure 3.5: (a) Raman scattering process (b) Phonon vibrational modes in a single layer graphene (c) One phonon process for G band and in the presence of defects the D peak for intervalley scattering.

To further investigate the quality of the transferred graphene crystals, we performed Raman spectroscopy measurements. Raman spectroscopy is an integral part of graphene research and it is a non -destructive method and widely used in academic research as well as in industry for samples inspection. By analyzing the Raman spectra, we can identify the number of graphene layers [118, 119], unwanted by products [120-122], structural damage [123], functional groups and chemical modifications [124, 125] introduced during the transfer process. Raman scattering is an inelastic scattering of photons by phonons. Raman scattering consists of three scattering process as shown in figure 3.5 (a). In stokes process, an incoming photon having energy $\hbar\omega_i$ excites an electron-hole pair (e-h). The pair decays into a phonon and another electron hole pair (e-h'). The latter electron-hole pair recombines emitting photon with lower energy $\hbar\omega_S$. Similarly, in anti-stokes process, the phonon is absorbed by the e-h pair and as a result a photon can leave the crystal with an increased energy $\Delta E = \hbar\omega_S - \hbar\omega_i$. In the scattering process if the frequency of the emitted photon remains the same as incident one, it is called Rayleigh scattering (also known as elastic scattering). Due to elastic scattering process, it is possible to see the single layer graphene on a thin spacer i.e. on SiO_2 thin film.

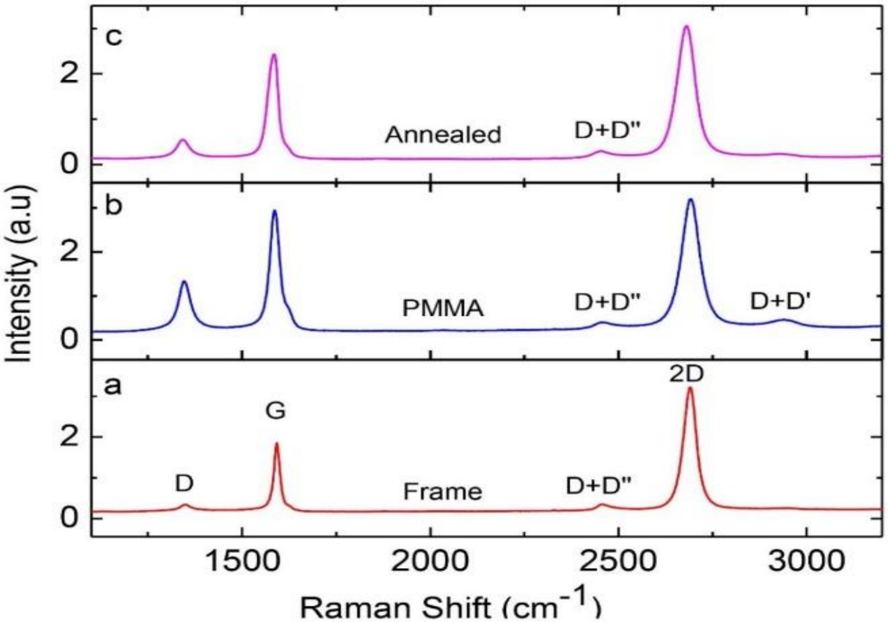

Figure 3.6: Raman spectra of graphene transferred by (a) PMMA-frame and (b) regular methods. The sample was annealed at 200^0C in argon atmosphere for 2 hrs. (c) Raman spectra of annealed sample.

Raman spectra of three graphene samples are shown in figure 3.6. Two main peaks are clearly observed, the prominent 2D peak at ~2700 cm^{-1} and the G peak centered at ~1580cm^{-1}. In figure 3.6 (a) a very weak D peak was observed at ~1350 cm^{-1}, which correspond to the defective non sp^2 bonds in graphene, suggests negligible amounts of defects are introduced by frame-assisted transfer process. The narrow and single symmetrical Lorentzian 2D peak, the high 2D to G peak intensity ratio (I_{2D}/I_G~2) and very low defect density (I_D/I_G~0.1) are further evidences of the high crystalline quality monolayer graphene [71] obtained by frame - assisted transfer method. On the other hand, for regular transfer graphene (Fig 2.6 b) the disorder induced Raman D peak at 1350cm^{-1} has been found to be more pronounced and broadened, suggesting that PMMA residues contributed with the increase of D band intensity. The D peak intensity is directly related to the amount of disorder [71], implying chemical reaction between the carbon atoms and PMMA molecules. Disorder in a monolayer graphene can be quantified by analyzing the intensity ratio of D band to G band i.e. I_D/I_G [126]. Initial I_D/I_G ratio in PMMA contaminated graphene was ~0.45 and after annealing the samples at 200^0 C in argon atmosphere, it reduced to 0.22. Similar reduction of I_D/I_G after annealing the PMMA at low temperature was reported by other groups [113, 127]. This is attributed to the reduction of PMMA contamination on graphene surface. This result supports our previous measurements i.e. decrease in two-probe resistance and reduction of average rms surface roughness of annealed PMMA samples.

A blue shift for 2D band in Raman spectra has been reported in literature[128, 129] for annealed samples at higher temperatures (>650^{0}C). Thermal decomposition of PMMA is a complex radical chain reaction [117] and in the decomposition process, many radicals are generated. Radicals react with graphene defects and local rehybridization of carbon from sp^2 to sp^3 may occur and consequently the resistance of the graphene sample will be increased. On the other hand, strong chemical interaction between the graphene and organic residues causes the broadening of Dirac cone in the band structure near Fermi energy, shifting the 2D peak to higher momentum. Another reason for 2D-peak shift is related to doping effect. The doping effect is related to the substrate coupling, where the charge from a substrate is transferred into the graphene in annealing process [130]. Raman 2D shift depends upon the types of doping charges. Electrons doping causes the red-shift, while the hole doping causes blue-shift [131]. We did not observe shift in Raman 2D peaks after annealing our samples at low temperature regime (200^{0}C), except a significant decrease in D peak intensity. It indicates no structural damages in graphene samples as well as no doping.

3.5: Conclusions:

In summary, we transferred graphene onto the SiO_2/Si substrates by regular and frame -assisted methods and characterized the graphene by AFM and Raman spectroscopy measurements. On the basis of these experimental results, frame-assisted methods significantly improved the graphene quality with less cracked film, less wrinkles with lower surface roughness and no polymer residues. Although the sheet resistance might be affected by the quality of the original graphene layers grown on Cu, we took graphene samples of the same batch and found that graphene transferred by frame methods have lower sheet resistance than that of PMMA-coated transfer method. Though the transfer process was demonstrated on silicon substrates in this work, it can also be generalized to the other types of substrates. The frame-assisted transfer method might be one of the ways toward the clean transfer of graphene that could enable large-scale device production.

Chapter 4

Investigations of Contact Friction and Transport Properties in Graphene

4.1: Introduction:

In this chapter, two sets of results on graphene along with their discussion and analysis are presented: (i) measurements of contact frictional force on gradually oxidized monolayer and bilayer graphene; and (ii) measurements of transport properties of graphene samples prepared in this work.

Regarding contact friction, experimental results revealed that contact friction on oxidized and reduced graphene is dominated by the generated vacancies on graphene instead of the add-atoms. This effect is attributed to the vacancy enhanced out-of-plane deformation flexibility in graphene, which tends to produce large puckering of graphene sheet near the contact edge and thus increases the effective contact area.

Proper discussion of the results on transport properties in graphene require a good understanding of the background theory. Therefore, in section 4.2, I have briefly reviewed relevant fundamental transport properties of graphene based on published papers cited here and these are used later in the chapter for analysis of the measured transport behaviors in high contact friction graphene. Modified graphene with large contact friction was heavily defected, but remained a good electrical conductor, in which the carrier transport was strongly affected by quantum localization effects even at room temperature. Furthermore, I noticed that the oxidation process in graphene is substrate sensitive. Compared to monolayer graphene on SiO_2 substrate, the oxidation process progressed much faster when the substrate is strontium titanate ($SrTiO_3$), while bilayer graphene exhibited great oxidation resistance on both substrates. The collection of observations described in detail in the following pages in this chapter provide important information for tailoring the mechanical, electrical, and chemical properties of graphene through selected defects and substrates.

4.2: Review of the Transport Properties in Graphene:

Graphene is a single layer of carbon atoms densely packed in a honeycomb lattice [98, 132]. The most noteworthy property of the band structure in graphene is the existence of two degenerate Dirac cones (as shown in the left inset of figure 4.1), which leads to two degenerate valleys (K and K'). Electrons in graphene behave as massless Dirac fermions at opposite corners of the Brillouin zone and show opposite chirality at each Dirac cone[133]. The existence of these valleys, each with a linear dispersion and pseudospin rotation are the main reasons that graphene has transport properties which differ from most other semiconductors or semimetals. Here, I have outlined fundamental transport properties of graphene related to my experimental works.

4.2.1: Tunable carrier density with higher mobility

The enormous list of publications on transport measurements in graphene started with the seminal papers by the group from Manchester and Columbia in the late 2004 and early 2005. The first experiments on graphene by Novoselov *et al* [134] and Zhang *et al* [135] revealed very characteristic transport properties in graphene. Monolayer as well as a stack of few layers' graphene sheets have been experimentally realized that with external gate voltage the charge carrier density can be tuned. Sheet resistance as a function of applied gate voltage is shown in figure 4.1 (a). The resistivity exhibits a sharp peak to the value of several kilohms near the Dirac point and decays to ~100 ohms at high gate voltage (V_g). The Hall coefficient (R_H) decreases with increasing carrier concentration in the usual way, as $R_H = 1/n$e. At the same applied gate voltage (V_g), where resistivity (ρ) has its peak, the hall coefficient R_H exhibits a sharp reversal of its sign [Fig 4.1 (c)]. This shows the ambipolar field effect on graphene.

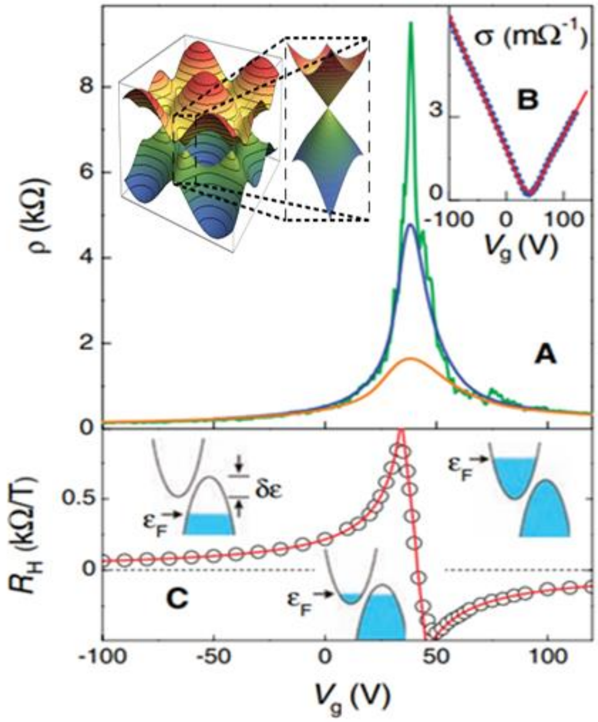

Figure 4.1: Field effect in graphene. (a) Resistivity as a function og gate voltage for diffeent temperature (b) Change in film conductivity and (C) Hall coefficient R_H versus V_g at T= 5K [98].

An equally important reason for the research interest in graphene is due to its high mobility carriers. Having electrons and holes concentrations n as high as $10^{13} cm^{-2}$, their mobilities μ can exceed 15,000 cm^2/Vs even under ambient conditions[98, 134, 136]. Moreover, the observed mobility in graphene is weakly temperature dependent, which means that mobility at room temperature (300K) is still limited by impurity scattering and, therefore, can be improved significantly even up to $\approx 100{,}000\ cm^2/Vs$. In graphene, mobility remains high in both electrically and chemically doped devices [137], which translates into ballistic transport on submicron scale (up to $\approx 0.3um$ at 300K). The gate voltage shifts the position of the Fermi energy E_F . A surface charge density induced by the gate voltage is given by $|\Delta n_s| = \frac{\varepsilon_0 \varepsilon \Delta V_g}{te}$, where ε_0 and ε are the permittivity of free space and substrate (SiO$_2$ as an example) respectively; e is the electron charge; and t is the thickness of the gate dielectric (SiO$_2$). Within the regime of long range, charged impurity scattering, the added free graphene carriers result in a roughly linear change in the graphene sheet conductance, σ_s, with the field mobility being a proportionality factor. Thus, sheet conductance can be expressed as [138]

$$|\Delta\sigma_s| = e\mu_{FE}|\Delta n_s| = |\Delta V_g \frac{\mu_{FE}\varepsilon_0\varepsilon}{t}| \tag{4.1}$$

and field effect-mobility is

$$\mu_{FE} = \frac{t}{\varepsilon_{0\varepsilon}}|\frac{\Delta\sigma_s}{\Delta V_g}| \tag{4.2}$$

4.2.2: Half integers QHE and minimum conductivity

The hallmark of the massless Dirac fermions (graphene) is QHE (Quantum Hall Effect) plateau in conductivity σ_{xy} at half integers of $4e^2/h$ [132]. As shown in figure 4.2, an uninterrupted ladder of equidistant steps in the hall conductivity σ_{xy} persists passing through the neutrality (Dirac) point, where charge carriers change from electrons to holes. The shift in the quantum plateau with respect to the standard QHE is by 1/2, so that $\sigma_{xy} = \pm\frac{4e^2}{h}(N + \frac{1}{2})$,where N is the Landau level (LL) index and factor 4 is due to the double valley and double spin degeneracy in graphene.

One of the reasons for the half -integer QHE might be the coupling between the pseudospin and orbital motion, which gives rise to a geometrical phase of π accumulated along the cyclotron paths, which is known as Berry's phase [135, 139] .The additional phase leads to a π-shift in the phase of quantum oscillations and as a result half -step shift in QHE limit.

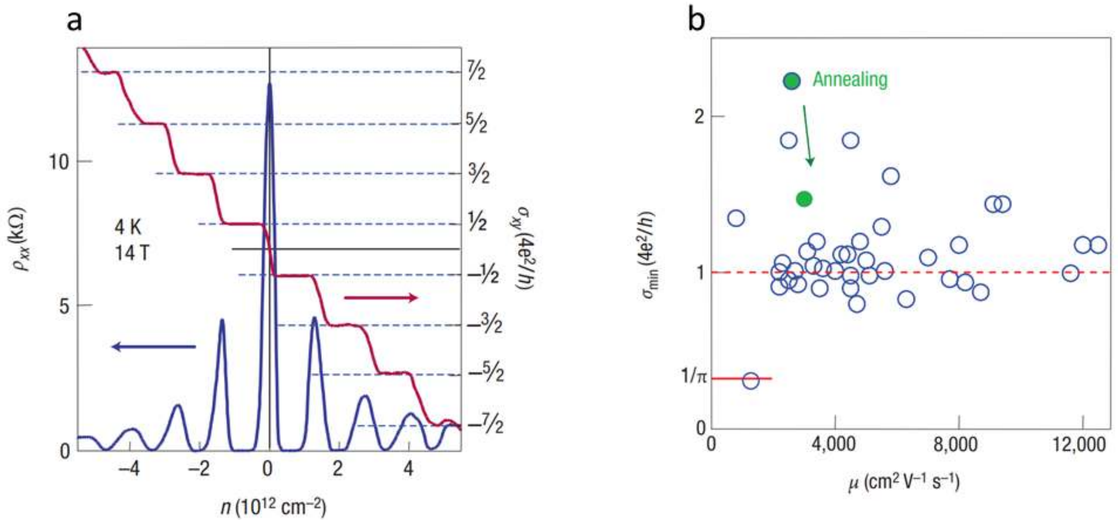

Figure 4.2: (a) Chiral quantum Hall effect in monolayer graphene. (b) Minimum conductivity at charge neutrality point with different carrier mobilities [132]**.**

Graphene's zero-field conductivity does not disappear in the limit of vanishing n but instead exhibits values close to the conductivity quantum $\frac{e^2}{h}$ per carrier type [134]. Figure 4.2 (b) shows the lowest conductivity σ_{min} measured near the neutrality as a function of charge carrier mobility. The result indicates that minimum conductivity of graphene is independent of their carrier mobility μ and different graphene devices exhibit approximately the same conductivity at the neutral point with most data clustering around $\approx \frac{4e^2}{h}$. For all others known materials, such a low conductivity at low temperature leads to a metal-insulator transition but no sign of transition has been observed in graphene down to liquid-helium temperature. The persistence of the metallic state with low conductivity of the order of $\frac{e^2}{h}$ is the most exceptional feature in graphene. In another words, the resistivity (conductivity) is quantized in graphene, in contrast to the resistance (conductance) quantization known in many other transport phenomena[140]. Most theories suggest $\sigma_{min} \approx \frac{4e^2}{\pi h}$ for graphene[141-143], which is π times smaller than the typical values observed experimentally ($\sigma_{min\,exp} \approx \frac{4e^2}{h}$). This disagreement has become known as the mystery of a missing π, and it remains unclear whether it is due to theoretical approximations about electron scattering in graphene, or because the experiments probed only a limited range of possible sample parameter (length -to -width ratio).

Close to the neutrality point ($n \leq 10^{11} cm^{-2}$) graphene conducts as a random network of electron and hole puddles[144, 145] and such microscopic inhomogeneity need to be considered in the theoretical calculation of σ_{min}.

4.2.3: Quantum correction to the Drude conductivity

Before discussing the quantum correction in disordered graphene, let us consider the elementary transport theory in a normal metal, where electrons have an effective mass m^*. The velocity of the electrons at the Fermi surface is given by $v_F = \hbar k_F / m^*$, where k_F is the Fermi wave vector whose value depends on the density of electrons. Impurities in a crystal deflect the electrons trajectories and introducing the relaxation time τ, defined as $\tau v_F = l$ (mean free path), the electronic conductivity in the metal is expressed as

$$\sigma_0 = e^2 n\tau / m^* \qquad (4.3)$$

This is purely classical results, known as Drude's formula, and which assumes that after each collision, the electron loses memory of its previous linear momentum state. It is also possible to view the conductivity as a random walk and the conductivity is related to the diffusion constant D through Einstein relation as

$$\sigma_0 = e^2 D\rho(E_F) \qquad (4.4)$$

where $\rho(E_F)$ is the density of states per unit area.

The resistivity of a metal or semiconductor is related to the probability of an electron to propagate between two given points in space. Classical physics assumes that the total probability is the sum of individual probabilities of diffusive paths. However, quantum mechanics suggests that total probably is the sum up quantum -mechanical amplitudes of the paths rather than probabilities themselves. Quantum correction to the conductivity of a disordered metal or semiconductor is due to quantum interference of election's wave functions and originates in quantum-mechanical superposition principle.

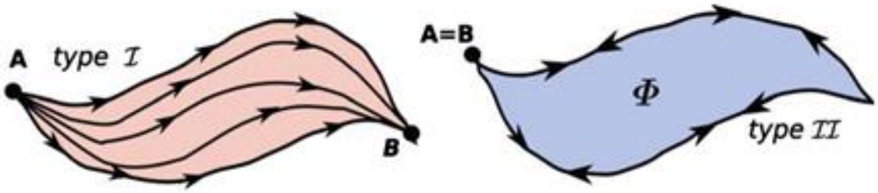

Figure 4.3: Pictorial representation of two types of scattering process. The presence of magnetic field is represented by the flux Φ enclsoed by the two time reversed trajectories [133]

Let us consider two types of scattering process as shown in figure 4.3. From classical point of view total probability of electrons traveling from A to B is

$$P^{cl}(A \rightarrow B) = |\sum_i a_i\, e^{i\Phi_i}|^2 \quad (4.5)$$

(sum of individual probabilities)

From quantum mechanics: for type I trajectories ($A \neq B$), we have

$$P^{I}(A \rightarrow B) = |\sum_i a_i\,|^2 + \sum_{i\neq j} a_i a_j\, e^{-i(\Phi_i - \Phi_j)} = |\sum_i a_i\,|^2 = P^{cl}(A \rightarrow B) \quad (4.6)$$

Since the phases for different trajectories of type I are uncorrelated, we assume that second terms averages to zero, leaving classical result, in which the probability to go from A to B is just the sum of the probabilities over all possible trajectories. However, for trajectories of type II (the same initial and final points), in the presence of time reversal symmetry, the situation is quite different. For the trajectories of type II, total probability is

$$P^{II}(A \rightarrow B) = 2|\sum_i a_i\,|^2 \quad (4.7)$$

From relation (4.7), it is clear that quantum interference associated with the two-time reversed trajectories of type II, enhances the probability of return relative to the classical results at low temperature, decreasing diffusion and therefor decrease in the conductivity. This phenomenon is known as weak localization (WL). In other words, WL results from constructive interference between pairs of time-reversed closed -loop electrons trajectories and provides a positive correction to the Drude resistivity. The result is just opposite for a system having strong spin -orbit coupling. The spin of the carrier rotates as it goes around a self - intersecting path, and the direction of this rotation is opposite for the two directions about the loop and as a result they interfere destructively. In ordinary semiconductor, spin -orbit coupling leads to suppressed backscattering due to destructive interference, leading to WAL and provides a negative correction to the Drude resistivity.

In the presence of magnetic field B, the relative phase of the electron's wave function, associated with the two-time reversed trajectories of type II is $\delta\phi = \frac{\pi\Phi}{\phi_0}$, where Φ is the magnetic flux passing through the area enclosed by closed trajectory. Therefore, applying the magnetic field to the system suppresses the interference effect (because relative phase is nonzero value) and as a result low temperature conductivity of the metal increases[133].

$$\Delta\sigma(B) = \frac{\sigma_{WL}(B) - \sigma_{WL}(0)}{\sigma_{WL}(0)} > 0 \quad \text{(positive magnetoconductivity for WL)} \tag{4.8}$$

4.2.4: Weak localization in graphene

Carrier scattering mechanisms in a graphene can be investigated via a magneto-transport measurement. There are two major types of scattering mechanisms in graphene: intervalley scattering , where electrons are scattered from one valley to another i.e. from K to K' (shown by solid green line on Fig 4.4 b) with a rate here denoted as τ_i^{-1} , and intravalley scattering ,where electrons scatter within a valley (solid red line in Fig 4.4 b) as described by a rate $\tau_a{}^{-1}$. In general, intervalley scattering originates from short range scattering, such as lattice defects, including grain boundaries, whereas intravalley scattering is a long range and typically stronger and also includes large scale inhomogeneities and charged impurities in the substrate. There is also another term $\tau_w{}^{-1}$, adding contribution to intravalley scattering. This scattering time has its origin in the fact that chirality is not exact symmetry of Dirac fermions in graphene (trigonal warping), therefore allowing for some amount of backscattering with the same valley[146]. The importance of this scattering time grows as the Fermi energy increases.

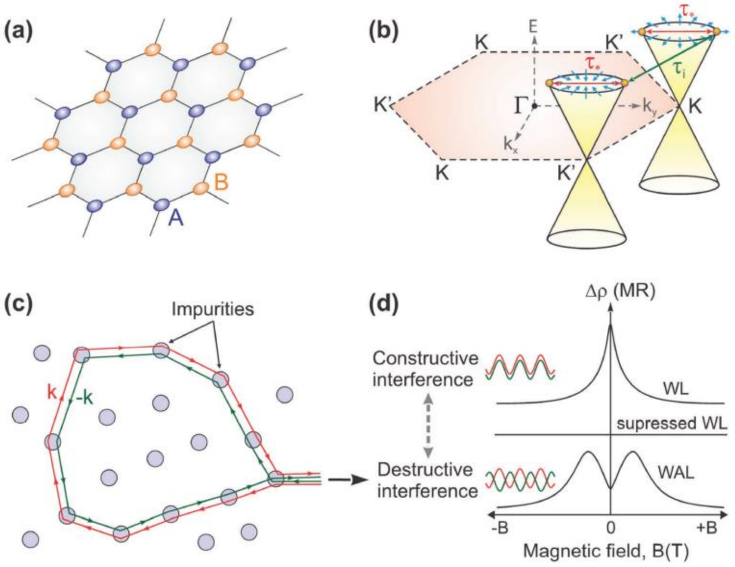

Figure 4.4: Schematic diagram to illustrate quantum interference mechanism in graphene. (a) Lattice structure of graphene. (b) Diagram illustrating intervalley and intravalley scattering process. (c) Schematic view of two time-reversed electron trajectories in a closed quantum diffusive path. (d) Magnetoresistance behavior in graphene [147]**.**

In graphene the intrinsic spin-orbit coupling is weak[148]. The charge carriers in graphene possess a pseudospin degree of freedom, which arises from the degeneracy introduced by the two inequivalent atomic sites per unit cell in graphene[134, 135]. Based on the sublattice composition of electronic Bloch states and band structure, charge carrier in monolayer and bilayer graphene have attributed Berry phases π and 2 π, respectively[149, 150]. On the basis of the Berry phase analysis, monolayer graphene can be expected to display typically weak anti-localization behavior as the two-time reversal pair in a closed quantum diffusive path results destructive interference (similar to that in materials with strong spin orbit coupling), in contrast, to bilayer graphene that displays standard weak localization effect and negative magnetoresistance (MR) due to the constructive interference. As long as the scattering potential are long range, intervalley scattering is negligible and backscattering in the graphene is absent, except from a small contribution from ${\tau_w}^{-1}$. Hence, scatterings within the same Dirac cone preserve the chirality of electrons [151] and electrons show WAL effect. In the presence of very short-range potentials, such as adatoms and vacancies, back scattering is permitted because of the intervalley scattering, which couples the states of opposite chirality at K and K' valleys and as a result smooth out π-phase contribution in monolayer graphene. Hence short-range scattering contributes to WL effect. Experimentally both weak localization (WL) and weak antilocalization (WAL) can be observed in graphene[152, 153], which depends on the dominating scattering process.

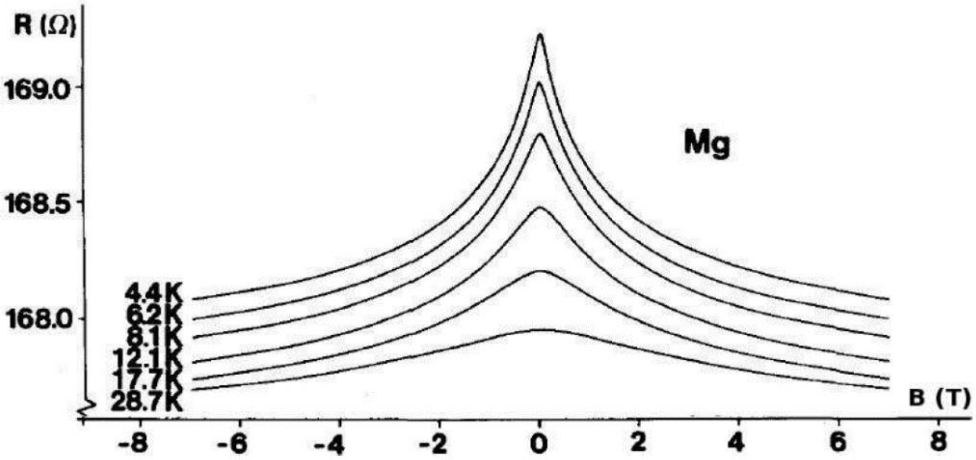

Figure 4.5: Experimentally measured resistance of a thin Mg film as a function of magnetic field at different temperatures. The magnetic field break the constructive interference of waves counter-propagation along closed loop, reduces the weak localization effect, and thus results in negative magnetoresistance [154].

How can weak localization be observed experimentally? Weak localization is due to the constructive interference between a multiple scattered path and its time-reversal. If one breaks time -reversal symmetry on purpose, then the interference is likely to disappear, and an enhancement of diffusive transport should be observed. Figure 4.5 shows the experimentally measured resistance of a 2D Mg film as a function of magnetic field at various temperatures. Magnetic field is applied perpendicular to the sample and in the presence of a vector potential A, a charged particle picks an additional phase $\int eA. {}^{dl}/_{h}$ along the close loop, which is $\frac{e}{h}$ times the enclosed magnetic flux. If this phase fluctuates largely from one loop to others, the resulting interferential contributions will vanish. As the smallest area enclosed by a diffusive loop is l^2, the weak localization correction is expected to vanish above $B\sim\frac{h}{el^2}$. For a sample with a mean free path a fraction of μm , this is in the Tesla range. At a very low temperature, propagation is all most fully phase coherent (phonons are locked) and one observes a decreasing resistance when a magnetic field is applied (negative magnetoresistance). At a high temperature the peak of the resistance at zero -field decreases because, larger temperatures reduce the phase coherence of the electronic wavefunction and reduce weak localization corrections.

The WL correction to the conductivity of graphene is obtained by considering the return probability of all possible trajectories. At zero magnetic field, the coherent return probability can be expressed as[155]

$$P(t) = \int_0^{\infty} \frac{1}{4\pi Dt}(1 - e^{-t/\tau_i})\, e^{-t/\tau_\Phi} dt = ln\, (\frac{\tau_\Phi}{\tau_i} + 1) \quad (4.9)$$

where the first term $(\frac{1}{4\pi Dt})$ in the integrant is the return probability $(P_0(t))$ for diffusion constant D, the second term represents the short time cut-off (τ_i), below which no elastic scattering occurs, and the third term is the phase coherence time cut-off (τ_Φ), below which phase coherence is lost. In general, the intervalley scattering in graphene contributes coherent backscattering; hence in equation (9) I included only intervalley scattering time τ_i (assuming small contribution from τ_w). At zero magnetic field, WL correction to the low temperature conductivity ($\tau_\Phi >> \tau_i$) can be written as[156]

$$\Delta\sigma = -(\,4e^2\,D/h)\;P(t)$$

and with the substitution of $P(t)$ from equation (9), we get

$$\Delta\sigma = -(e^2/\pi h)\,\ln\,(\frac{\tau_\Phi}{\tau_i}) \quad (4.10)$$

The negative sign in equation (10) indicates the decrease in conductivity due to weak localization effect.

A magnetic field destroys the phase coherence of these two paths, resulting in an increased conductivity (decreased resistivity). For a thin film in a perpendicular magnetic field, phase coherence is lost after a time $\tau_B \sim \hbar/eBD$ (D is the diffusion coefficient). McCann and coworkers have obtained a general expression for the WL and WAL correction specific to graphene[157], which determines the dependence of the magneto-resistivity as a function of B involving the scattering paraments τ_i (intervalley) and τ_a (intravalley) explicitly. They obtain the following expression:

$$\Delta\sigma(B) = \frac{e^2}{\pi h}\left[F\left(\frac{B}{B_{\phi}}\right) - F\left(\frac{B}{B_{\phi}+2B_i}\right) - 2F\left(\frac{B}{B_{\phi}+B_i+B_*}\right)\right] \tag{4.11}$$

where, $F(Z) = ln(Z) + \Psi\left(\frac{1}{2} + \frac{1}{Z}\right)$, where Ψ is the digamma function and $B_{\phi,i,*} = \frac{\hbar}{4eD} L_{\phi,i,*}^{-2}$ denotes the characteristic magnetic fields associated with the diffusion constant D. The first term in equation (12) corresponds to the usual WL observed in typical 2D system where electron mean free path is shorter than the phase coherence length, the second and third term lead to WAL and $\Delta\sigma(B)$ can be either positive or negative depending on the relative values of the different scattering times, including τ_B. Here, L_{ϕ} denotes the phase coherence length, L_i is the elastic intervalley scattering length, and L_* is related to the intravalley scattering length L_a and trigonal warping length L_w with the relation

$$\frac{1}{{L_*}^2} = \frac{1}{{L_a}^2} + \frac{1}{{L_w}^2} \tag{4.12}$$

and corresponding scattering rates are related by

$$\frac{1}{\tau_*} = \frac{1}{\tau_a} + \frac{1}{\tau_w} \tag{4.13}$$

(Note: scattering rate is related to the scattering length by $L = \sqrt{D\tau}$, where D is the diffusion constant and can be calculated by using the relation $D = \frac{v_F . l}{2} = \left(\frac{v_F}{2}\right).\left(\frac{h}{2e^2 k_F R_{xx}}\right)$, where v_F is the fermi velocity, k_F is the Fermi wave vector, and l is the carrier mean free path. The Fermi wave vector k_F in graphene is related to the carrier density n by $k_F = \sqrt{\pi n}$).

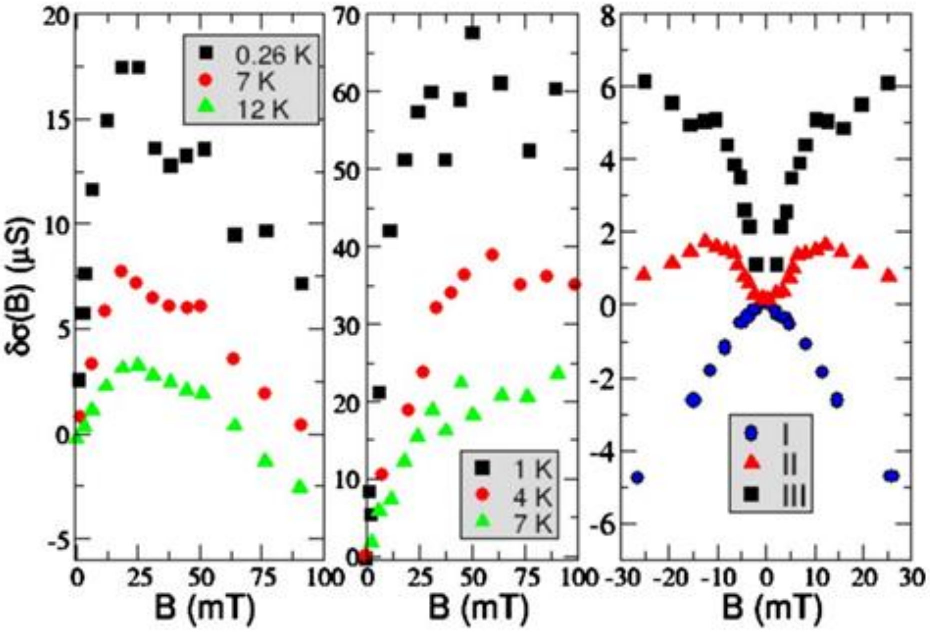

Figure 4.6: Magnetoconductivity of graphene. Left: weak antilocalization behavior (electron density $n \leq 7 \times 10^{10} cm^{-2}$). Center: weak localization behavior ($n \leq 8 \times 10^{11} cm^{-2}$). Right: dependence $\delta\sigma(B)$ on the electronic density (it grows from I to III) [153].

Figure 4.6 shows the typical magneto-conductivity behaviors as a function of magnetic field in a graphene. In the left panel of figure, for small values of magnetic field, $\Delta\sigma(B)$ grows (WL) up to a certain field value B_* and then starts to decrease (WAL*)* up on increasing the magnetic field over B_* and no saturation of $\Delta\sigma(B)$ is observed. The central panel shows WL behavior in graphene since the corrections $\Delta\sigma(B)$ never decrease upon increasing the magnetic field and tend to saturation. Since the electronic density in the central panel of figure is a few times larger than that in the left one, it seems that the effect of short -range scatters (intervalley) is more effective at higher densities; at lower densities long-range scatterers (intravalley) dominate. In the right panel of Fig 4.6, we clearly see a crossover from weak antilocalization to weak localization as the electronic densities increases from I to III, at a temperature 27K.

4.3: Experimental Section:

4.3.1: Graphene transfer

To prepare samples for this research project, thin layer of Poly (methyl methacrylate) (950 PMMA A_3) was spin coated onto the graphene to act as a support and allowed to dry at room temperature for 2 hours. Graphene residues, on the other side of copper foil, were cleaned by oxygen plasma. In the chemical etching process, Cu foil was etched using Ammonium persulfate solution [$(NH_4)_2S_2O_8$] having concentration of 6.9 grams/ 150 ml DI water, for 17 hours. The floating sample (PMMA/graphene) on solution was cleaned with continuous flow of deionized (DI) water for 2-3 hours and transferred on SiO_2/Si substrate manually. The transferred PMMA/graphene sample was gradually heated up to 100^0 C (about 30 mins) to evaporate the water and the PMMA layer on the graphene surface was cleaned with warm acetone (50^0 C).

4.3.2: Shield oxygen plasma treatment

To gradually oxidize the graphene, we used March PX -250 Plasma Asher and set up oxygen gas flow of 49 sccm (standard cubic centimeters per minute) for a process pressure of 300mTorr. The pristine graphene on SiO_2/Si substrate was placed on the sample holder with graphene facing downward and the edges of the sample (5mm × 5mm) further shielded with Kapton tape. Then, the graphene was gradually oxidized with RF power of 200W setting different oxygen plasma exposure times.

4.3.3: laser induced reduction

Laser reduction experiment was performed using a diode laser (wavelength 405 nm) and output power was set to 100 mW. The laser irradiated area on the sample was 12 mm^2. Graphene oxide film was exposed to laser in air at room temperature for 14 hours.

4.3.4: Sample characterizations

X-ray photoelectron spectroscopy (XPS) measurement was performed with a commercial Physics Electronics PHI 5000 Versa Probe system equipped with a focused monochromatic X-ray source (Al Kα at 1486.6 eV with 100 μm beam size). All XPS experiment was carried at room temperature at a pressure better than 10^{-8} mbar. Commercial

Renishaw Invia Raman Spectrometer with 532 nm excitation wavelength and 0.02 cm^{-1} spectral resolution was used for Raman characterizations. The Raman emission was collected by Olympus 50 × objective for better signal to noise ratio, and the excitation laser was set to low power to prevent the potential structure damages of graphene.

4.3.5: Magneto-transport measurements

For magneto-transport measurements, we patterned the graphene standard Hall bars structure. For electrical contacts, we deposited Au/Ti (30 nm/ 5 nm) by KJL Lab 18 e-beam Evaporator. Magneto resistance measurements at temperature ranging from 2 K to 300 K were performed using a PPMS system manufactured by Quantum Design Inc. Magnetic field up to 9T (90 kOe) was applied perpendicular to the sample surface.

4.4: Results and Discussion:

4.4.1: Abruptly enhanced contact friction in gradually oxidized graphene

Graphene synthesized by chemical vapor deposition (CVD) was transferred to SiO_2/Si substrate using the PMMA-based method [158]. Instead of regular laboratory solvents (acetone and isopropyl alcohol) cleaning, the transferred graphene was also annealed at 300ºC in a vacuum of 10^{-9} mbar to remove traces of PMMA residue. To produce a graduate oxidation process, samples with transferred graphene were placed upside down on a glass slide inside the chamber of an oxygen plasma etcher. The greatly shielded plasma exposure ensured good structural integrity in graphene even after plasma exposure durations (τ_{OP}) longer than two minutes.

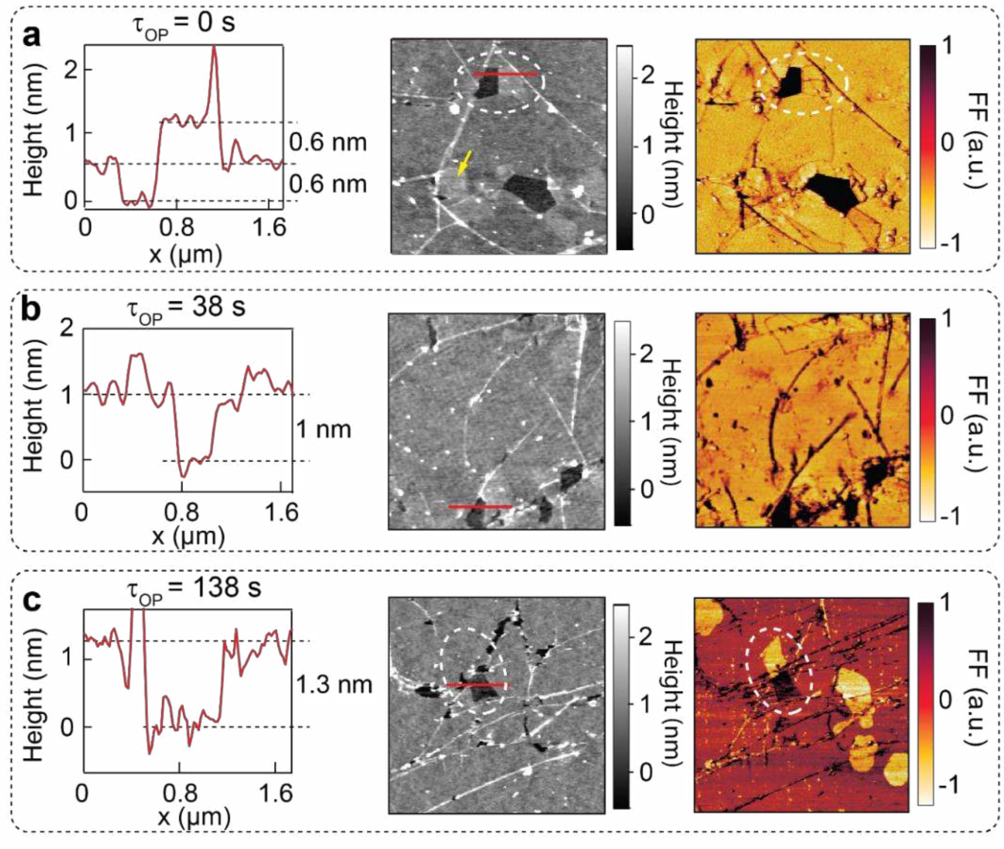

Figure 4.7: Evolution of contact friction in monolayer and bilayer graphene (a-c) Scanning probe imaging performed at three oxygen plasma durations (a) τ_{OP}=0 s, (b) τ_{OP}=38 s, and (c) τ_{OP}=138 s. The middle and right columns are topography and frictional force images measured simultaneously. Height profiles along regions marked by red lines are plotted on the left. White dash circles mark the location where the graphene sheet breaks and folds over during transfer. All images have the same dimension of 5 μm × 5 μm.

Figure 4.7 shows the contact mode atomic force microscope (AFM) topography and frictional force images taken at three oxygen plasma doses (τ_{OP}). In order to reliably track the evolution of graphene properties, all imaging was performed near graphene cracks where the exposed oxidation inert SiO_2 substrate can serve as a reference. After each plasma exposure, the samples were stored in the air for at least five hours before the scanning probe measurements. This wait time ensures a consistent equilibrium state of the surface adsorption of airborne hydrocarbons and prevents the related variation in surface friction. Transferred graphene was mostly monolayer, though bilayer regions were also present and could be found in every 5 μm × 5 μm scans size. In pristine state, bilayer graphene was clearly distinguishable in the surface topography (Fig. 4.7 a, middle). Some bilayer regions were produced directly by CVD growth (yellow arrow, Fig. 4.7 a) and some were generated during the transfer when cracked monolayer graphene pieces got folded over (white dash circles, Fig.4.7a, c). The thickness of monolayer graphene before plasma treatment was around 0.6 nm (Fig.4.7a, left). There was no obvious friction contrast between monolayer and bilayer graphene, though both exhibited a much smaller contact friction comparing to SiO_2 (Fig.4.7a, right).

At τ_{OP} = 38 s, thickness of monolayer graphene increased to 1 nm (Fig.4.7b, left), most likely due to the adsorption of oxidation functional groups [159]. In the meanwhile, bilayer graphene regions became harder to distinguish in the topography image (Fig.4.7b, middle), indicating their much less thickness growth. Despite the topography variation, the frictional force contrast between monolayer/bilayer graphene and SiO_2 remained almost the same as the pristine state.

The similar low contact friction in both monolayer and bilayer graphene showed little variation for τ_{OP} up to 100 s (Fig.4.9 c). However, a drastic change occurred when τ_{OP} increased to 138 s. At this state, although frictional force was still at the pristine level in bilayer graphene, it became much larger in monolayer graphene (Fig.4.7c, right). On the other hand, surface topography change follows the similar trend as observed at smaller τ_{OP}. Monolayer graphene thickness increased to around 1.3 nm, and bilayer graphene became completely undistinguishable from the topography image. The gradual increase of monolayer thickness indicates a continuous and smooth progress of oxidation, raising the question of what caused the abrupt change in the contact friction. Additionally, the different response found in bilayer graphene also needs to be understood.

4.4.2: Correlation of contact friction with vacancy density

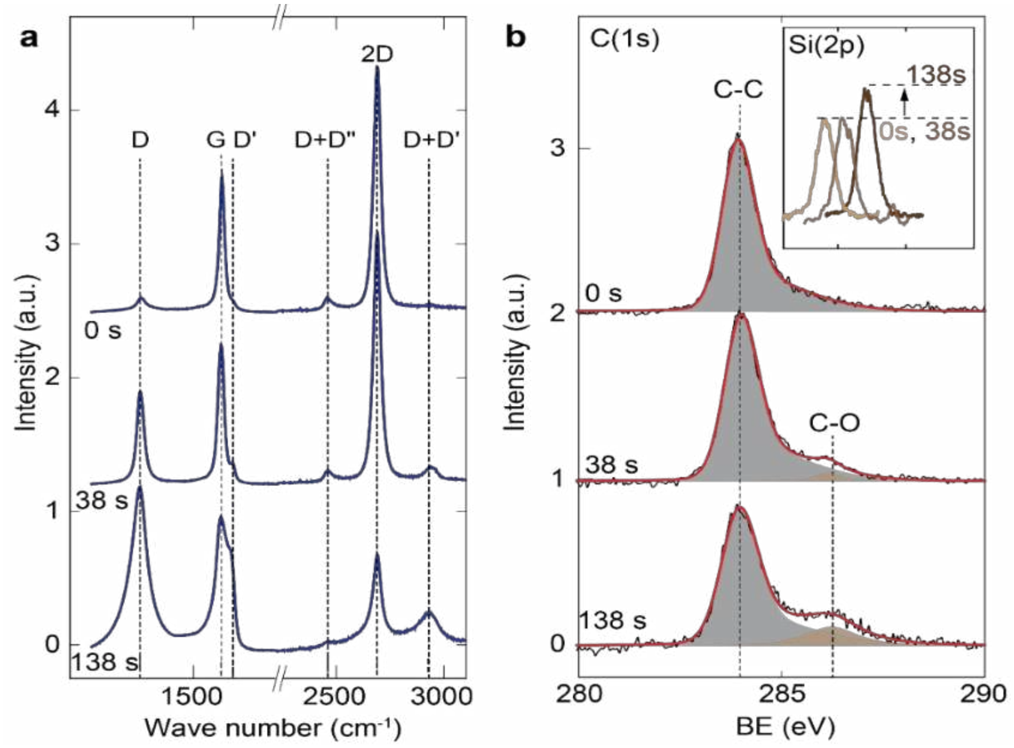

Figure 4.8: Evolution of defect density and type (a) Raman spectrums and (b) XPS spectrum of C(1s) taken at different τ_{OP} (vertically displaced for clarity). Inset in (b) shows the Si(2p) peak normalized by carbon concentration.

To answer these questions, Raman spectroscopy (Fig.4.8 a) and X-ray photoelectron spectroscopy (XPS) (Fig.4.8 b) were performed to examine the exact effects of plasma induced oxidation. The Raman spectra obtained from the pristine graphene was dominated by two first order peaks at ~ 1589 cm^{-1} (denoted by G) and ~2684 cm^{-1} (2D), while disorder related peaks (D, D’, D+D”, D+D’) were very weak, indicating high crystallinity of the sample [160]. At τ_{OP} of 38 s, disorder related Raman peaks increased significantly, which was accompanied by the emergence of XPS peak at around 287 eV (C-O bond), indicating the formation of epoxide and/or hydroxyl groups. Since the ratio between 2D and G Raman peaks remained unchanged comparing to pristine graphene and the D’ peak was still very weak at this stage, the sample is expected to be in a low defect density regime where disordered regions are well isolated from each other [72].

In this regime, an average distance between disordered regions ($l_D \approx 12$ nm) can be extracted from D and G peaks intensity ratio using the equation of $I(D)/I(G) = C(\lambda)/l_D^2$ [76, 161]. In the meanwhile, XPS spectrum indicates that around 3.5% of carbon atoms contribute to the C-O bonds. At this percentage, if all oxygen add-atoms are well scattered, the average defect distance will be 0.8 nm, much less than the previous estimation from Raman spectrum. Therefore, the oxidation functional groups likely tend to congregate into heavily defected islands, and the 12 nm value of l_D may represent the distance between such islands. As can be seen in Figure 4.7b, although the oxidation at this stage produced a significant increase in the AFM measured monolayer thickness, the adsorption of epoxy or hydroxyl groups have little effect on the contact friction of graphene.

At τ_{OP}=138 s, Raman peaks started to broaden. D and D' peaks became more pronounced and $I(2D)/I(G)$ reduced significantly. These features indicate a high defect density regime where disordered regions start to coalesce [72]. In this regime, $I(D)/I(G)$ ratio is known to become proportional to l_D^2 [76, 161], and $l_D \approx 4$nm can be estimated by imposing continuity between the low and high defect regimes. XPS spectrum shows that the percentage of carbon atoms associated with C-O bonds increased to 12.7%. In addition, XPS signals from the SiO_2 substrate also increased considerably (Fig.4.8 b inset), which was not observed at τ_{OP} = 38 s. This effect is produced most likely due to the formation of vacancies in graphene sheet and the consequent exposure of the substrate. Unlike the continuously increasing functional group density, vacancies in graphene only occurred at large τ_{OP}, manifesting a better correlation with the contact friction in monolayer graphene.

4.4.3: Friction enhancement caused by laser-induced vacancy generation

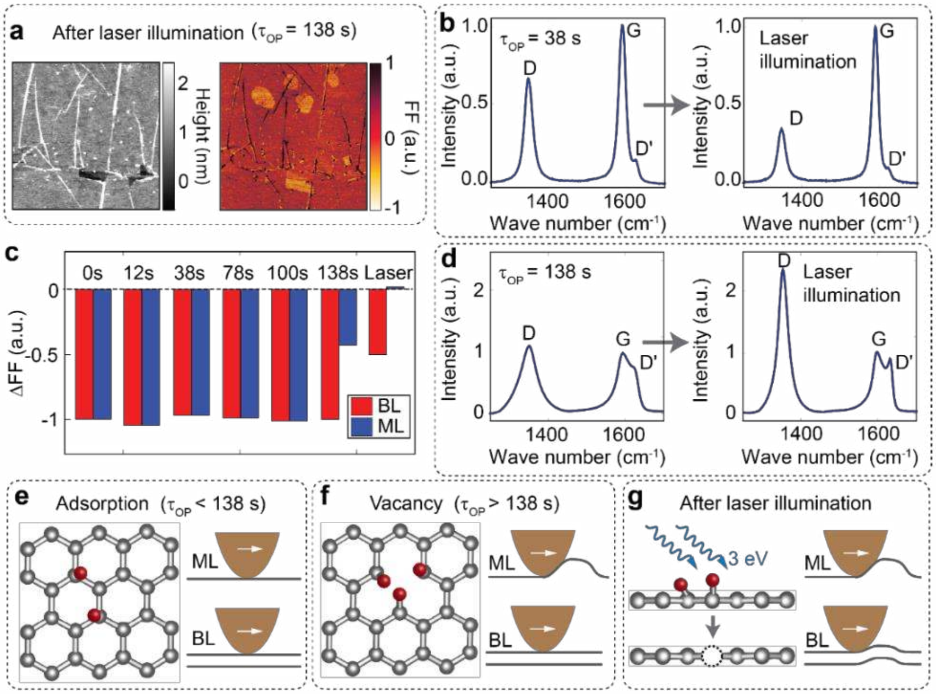

Figure 4.9: Vacancy enhanced contact friction (a) At τ_{OP}=138 s, surface topography (left) and frictional force (right) images taken after laser illumination. (c) Relative frictional forces in monolayer and bilayer graphene in reference to SiO_2 measured in pristine state, after different τ_{OP}, and after laser illumination. (b, d) Change of Raman spectrum before and after laser illumination at (b) τ_{OP}=38 s and (d) τ_{OP}=138 s. (e) For small τ_{OP}, the adsorption of oxygen/hydroxyl has little effect on the surface friction of graphene. (f) For large τ_{OP}, vacancies start to form in monolayer graphene and significantly increases its frictional contact with the scanning probe. (g) Laser excitation facilitates both the desorption of oxygen and hydroxyl.

To elucidate the roles of different defects in controlling the contact friction of graphene, oxidized graphene sheets were re-measured after being illuminated by 405 nm laser. Since the photon energy (~3.1 eV) is larger than the typical bonding energies of C-O based functional groups ($E_{hydroxyl}$ ~ 0.7 eV, E_{epoxy} < 2.7 eV) [162, 163], laser illumination can cause these functional group to partially dissociate. Such laser induced reduction[164, 165] was clearly reflected in Raman measurements (Fig.4.9b, d). In samples where disordered regions were well isolated ($I(D)/I(G)\propto 1/l_D^2$), $I(2D)/I(G)$ decreased after laser illumination (Fig.4.9 b). In samples where disordered regions coalesce ($I(D)/I(G)\propto l_D^2$), $I(2D)/I(G)$ increased after laser illumination (Fig.4.9 d). Both observations indicate the decrease in defect density [76, 161]. Although the overall defect density was reduced by oxygen desorption, the density of vacancies was affected by laser differently. On one hand, existing vacancies cannot be removed by laser. On the other hand, the breaking of C-O bonds is known to cause atomic rearrangement and can create new vacancies or other structural distortions (Fig.4.9 g). Therefore, decrease in functional group density and increase in vacancy density are expected after laser illumination.

Figure 4.9a shows the topography (left) and frictional force (right) images taken after the τ_{OP} = 138 s sample was illuminated by laser. Although density of functional group was reduced (Fig.4.9 d), the contact friction of monolayer graphene further increased above the SiO_2 level, and the friction in bilayer graphene also increased (Fig.4.9 c), which most likely resulted from the laser facilitated vacancy generation. It is thus clear that the contact friction in oxidized graphene is dominantly controlled by the presence of vacancies rather than the adsorbed functional groups.

To understand the effects of vacancies on contact friction, the elastic flexibility of graphene needs to be considered. Unlike conventional 3D materials, the atomically thin graphene sheet weakly bond to the substrate can undergo significant out-of-plane deformation. It has been suggested that adhesion with the scanning probe can cause puckering in graphene near the contact edge[33, 34, 41, 166]. This effect significantly increases the contact area and strongly affects the frictional force. The magnitude of local puckering is closely related to the out-of-plane stiffness of graphene. This quantity, very similar to the contact friction reported here, was experimentally found to be insensitive to adsorption of oxygen add-atoms and degrades only in presence of vacancies [72]. Therefore, we attribute the abruptly changed contact friction in monolayer graphene to the creation of vacancies that requires long enough oxidation time (Fig.4.9e, f). Once adequate amount of vacancies is present, the graphene sheet becomes more flexible to pucker, giving rise to the much larger frictional force measured.

4.4.4: Substrate-dependent oxidation resistance

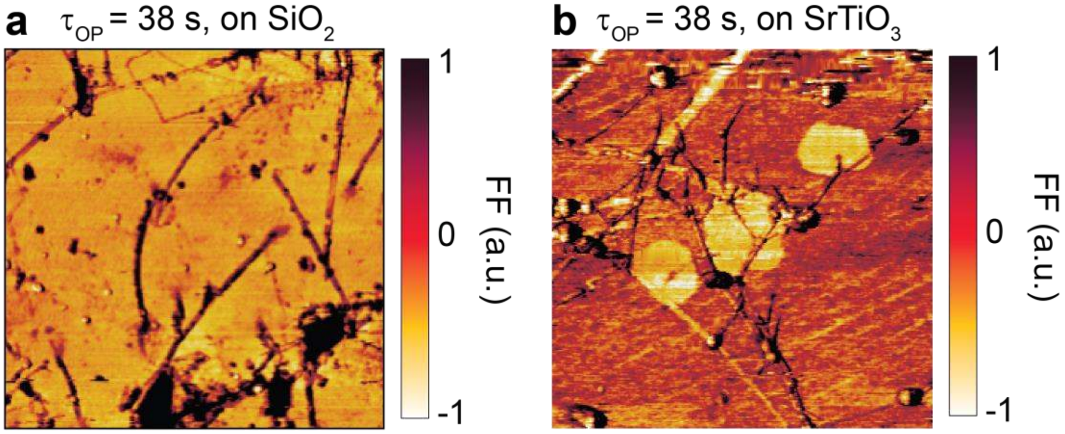

Figure 4.10: Substrate dependent oxidation rate. Frictional force images of graphene on (a) SiO_2 (same as shown in Figure 4.7 b) and (b) $SrTiO_3$ after 38 s plasma treatment.

The observations presented above also prove the substrate-sensitive chemical inertness of graphene and the better oxidation resistance of bilayer graphene as predicted by first-principle calculations[167]. The diminishing height difference between monolayer and bilayer graphene upon slow oxidation as well as the clear friction contrast observed at τ_{OP} = 138 s (Fig.4.7) show that, compared to graphene on SiO_2 substrate, graphene on graphene substrate (i.e. bilayer graphene) is much more difficult to oxidize [168]. Though exposure to short wavelength light after plasma treatment seemed capable of generating vacancies in both monolayer and bilayer graphene (Fig.4.9 g). In addition, we also found that vacancies are much easier to form in monolayer graphene transferred to $SrTiO_3$ substrate (Fig.4.10 b). For a τ_{OP} of 38 s, contact friction in monolayer graphene on $SrTiO_3$ increased significantly, producing a clear contrast with bilayer graphene. On the contrary, the same τ_{OP} produced almost no effects in friction for graphene on SiO_2 substrate (Fig 4.10 a). The reduced oxidation resistance in graphene on $SrTiO_3$ might be related to the strong orbital hybridization at the interface [169] that can facilitate the charge transfer to oxidative ions in the plasma.

4.4.5: Transport behaviors in the high contact friction state

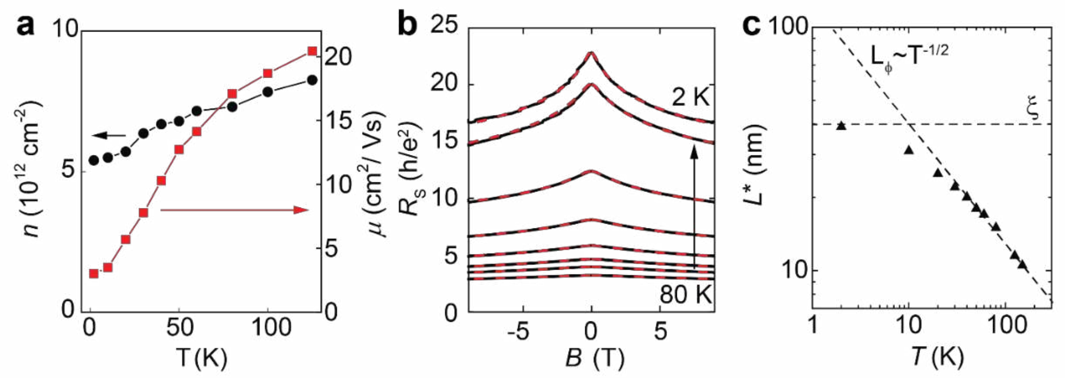

Figure 4.11: Localization effect at high defect density (a) Temperature dependent carrier density and mobility measured in graphene at τ_{OP} = 138 s. (b) Magnetoresistance measured at various temperatures. Black solid lines are original data and red dash lines are fitting using weak localization model as described by Eq.1. (c) Temperature dependence of the characteristic length L* extracted from the fitting. At higher temperatures L* is dominated by the phase coherence length $L_\phi \sim T^{-1/2}$. As L_ϕ increases at low temperatures, L* becomes more significantly affected by the temperature independent localization length ξ

Although the defect density (>12.7%) accompanying the enhanced contact friction was very large, the electrical conduction of graphene at τ_{OP} =138 s remained ohmic. This is likely owing to the congregation of defects, which preserve nanometer-level pristine regions between defect islands. At this oxidation stage, the sheet resistance R_S (2.3 h/e^2) became larger than the resistance quantum $R_0 = h/e^2$ even at room temperature. R_S only weakly depended on the gate bias, and the temperature dependence of carrier density (Fig.4.11 a) was also weak; both are against bandgap opening. Therefore, it is still reasonable to analyze the electrical properties of the heavily oxidized sample within the framework of disordered graphene, where the resistance is affected by both diffusive scattering and quantum interferences. Due to the Dirac electron dispersion, semi-classical calculations predicted a maximum diffusive scattering based resistivity $R_{S-C}^{\max} = \pi h / 4e^2$ for disordered graphene systems [170, 171]. Since R_S was considerably larger than $R_{S-C}^{\max}$, influences of quantum interference induced localization effect are not negligible even at room temperature. Additionally, since R_S is also larger than R_0, the crossover from weak localization to strong localization need to be considered.

The strength of localization effects can be quantified by the ratio between phase decoherence length L_ϕ and localization length ξ. Magnetoresistance measurements were performed to characterize L_ϕ and ξ in the heavily oxidized graphene. As shown in figure 4.11b, resistance peak at zero magnetic field was observed and became more pronounced as temperature decreases. We first compare such feature to typical weak localization model in graphene with equation (10) described on section 4.2; according to which

$$\Delta\sigma(B) = \frac{e^2}{\pi h}\left[F\left(\frac{B}{B_\Phi}\right) - F\left(\frac{B}{B_\Phi + 2B_i}\right) - 2F\left(\frac{B}{B_\Phi + B_i + B_*}\right)\right] \tag{4.14}$$

Fitting results based on equation (4.14) are shown in figure 4.11 b. It was found that the influences of the last two weak antilocalization terms are negligible. This was likely the result of the frequent defect facilitated intervalley scattering (*i.e.* large τ_i^{-1}), which were also evidenced by the large *D* and *D'* peaks in the Raman spectrum. From B_ϕ, a characteristic length $L^* = \sqrt{\hbar / 4eB_\phi}$ can be extracted. As shown in figure 4.11c, L^* shows a $T^{-1/2}$ dependence at higher temperatures but gradually saturates below 30 K. Such behavior was also observed in semiconducting two-dimensional electron gas (2DEG) systems with sheet resistance between R_0 and $100R_0$ that undergo the transition from weak localization to strong localization [172]. In this regime, the characteristic length L^* depends on both the phase coherence length L_ϕ and the localization length ξ : $\frac{1}{L^{*2}} = \frac{1}{L_\phi^2} + \frac{1}{\xi^2}$. When the carrier dephasing is dominated by electron-electron scattering, L_ϕ follows a $T^{-1/2}$ temperature dependence [173]. At higher temperatures when $\xi > L_\phi$, L^* is approximately equal to L_ϕ and therefore also obey the same $T^{-1/2}$ dependence. As L_ϕ increases and eventually exceeds ξ at low temperatures, the value of L^* instead becomes dominated by the temperature invariant ξ. As can be seen from figure 4.5 c, localization length ξ at τ_{OP}=138 s ($l_D \approx 4$nm) is around 40 nm, which is consistent with the theoretical prediction based on similar average defect distances [170, 171, 174, 175].

4.5: Conclusions:

In conclusion, the contact friction in graphene can be significantly enhanced by the introduction of vacancies but is relatively insensitive to the adsorption of C-O based add-atoms and functional groups. Presence of vacancies can make the graphene sheet more flexible to pucker at the contact edge, which increases the contact area and thus leads to a larger contact friction. Modified graphene in the large friction state functions as a good electrical conductor, making it potentially useful in applications such as triboelectric devices. Additionally, bilayer graphene, showing much higher oxidation resistance than monolayer graphene, is expected to be a better choice in applications requiring high chemical stability.

Chapter 5

Conclusions and Future Work

The objectives of this research on graphene were to develop the polymer-free graphene transfer methods and understand the nano frictional behavior of monolayer and bilayer graphene for triboelectricity and energy harvesting. For this purpose, in this work we used chemical vapor deposition grown graphene samples on copper foils. In a regular graphene transfer process, a thin layer of poly-methyl methacrylate (PMMA), a supportive layer, is spin -coated onto the graphene surface, and metal below is etched away completely. Although regular transfer is a simple and widely used method, this method leaves polymer residues on the graphene surface. To address this issue, we developed an effective polymer-free and gold frame -assisted graphene transfer method. The resulting graphene was characterized by using atomic force microscopy (AFM), Raman and X-ray photon electron spectroscopy (XPS) measurements. Our results showed a clean, and crack-free graphene film having less wrinkles and with low sheet resistance.

The next important result is on the contact frictional force in oxidized monolayer and bilayer graphene transferred on SiO_2. In order to produce gradual oxidation process, samples with transferred graphene were placed upside down on a glass slide inside the chamber of an oxygen plasma etcher. The greatly shield plasma exposure ensures good structural integrity in graphene even after plasma exposure duration longer than 2 minutes. Micro-scale tribological studies showed that introduction of defects in graphene increases friction. Also, chemical modifications of graphene by hydrogenation, fluorination, or oxidation results in 2, 6, and 7 times increase in friction, respectively. In contrast, our experimental results demonstrated that contact friction in monolayer graphene can be significantly enhanced by the introduction of vacancies but is relatively insensitive to the adsorption of C-O based add -atoms and functional groups. Presence of vacancies can make the graphene sheet more flexible to pucker at the contact edge, which increases the contact area and thus leads to a large contact friction. Modified monolayer graphene in the large friction state remained as a good electrical conductor, making it potentially useful in applications such as triboelectric devices.

Additionally, frictional force in bilayer graphene was observed to be less as compared to the monolayer graphene. In other words, bilayer graphene, showing much higher oxidation resistance than monolayer graphene, is expected to be a better choice in applications requiring high chemical stability and super solid lubricant. Success in tailoring the frictional properties of monolayer graphene by gradual oxidation process, has opened path to carry further research on graphene-based smart electric generators that can produce electricity in response to moisture, friction, pressure, and heat.

Experimentally, we observed negative magnetoresistance on the graphene oxide samples and the measured data fitted well with the weak localization model of graphene. Our experiments were performed at much lower temperature (~2K), but one can explore the temperature dependence of magnetoconductivity at high temperature and even at room temperature on the pristine graphene samples. In conventional 2D systems the quantum correction usually disappears at much lower temperatures, due to intensive electron-phonon scattering. In graphene, however electron -phonon scattering is expected to be weak, and thus it is interesting to search the quantum interference effect at high T. The negative magnetoresistance observed on the graphene samples having higher defect density and higher frictional state has suggested that the scattering process on the given samples is dominated by short-range scatterers (intervalley). This result has raised an additional question; how the magnetoconductivity evolves with increasing defect densities on the monolayer and bilayers graphene samples. Further studies are required to better understand the dependence of magnetoconductivity on the electronic density of graphene.

Understanding carrier scattering and low temperature conductivity of graphene is one of the fundamental but still debatable questions in physics. The effect of magnetic field on the electrons transport in graphene with various levels of impurities doping can be understood using magnetoconductivity or magneto-resistivity measurements. The difference in the negative and positive magnetoresistance is attributed to different types of scattering mechanisms in various samples. In recent years, graphene nano ribbons are of particular interest because they exhibit a conduction bandgap that arises due to size confinement and edge effect. Besides, theoretical studies have suggested that graphene nanoribbons could have interesting magneto-electronic properties, with a very large predicted magnetoresistance

[176-178]. Graphene nanoribbons field -effect transistors with tunable magnetoresistance have been reported in the literature [179, 180] with the possibility of opening up exciting opportunity in magnetic sensing and a new generation of magneto -electronic devices.

The change in the resistivity as a function of magnetic field is usually small in metals, with $\frac{\Delta\rho}{\rho} \sim 0.1 - 1\%\ \mathrm{T}^{-1}$. The reciprocal phenomena also exist i.e., a spin -polarized current flowing through a magnetic nanostructure can influence its magnetic state. Hence, magnetoresistance measurement might be one of the important parameters for spin-related studies and to characterize the junction of a two-layer structure consisting of a magnetic semiconductor and a nonmagnetic semiconductor. As an example, Lin *et al.*[181] fabricated MnSi/Si/MnSi heterostructures and performed two-terminal magnetoresistance measurements. In their two-terminal measurement, a bias voltage was applied across the axial heterostructure and resistance was measured as a function of magnetic field. They observed a small negative magnetoresistance at a low magnetic field and a moderately high bias voltage. This magnetoresistance was attributed to spin injection from ferromagnetic MnSi at one end of the heterostructure and spin detection by MnSi at the other end. On the other hand, semiconductor -ferromagnetic core/shell heterostructure may have potential applications in three -dimensional magnetic recording and data storage devices. Unlike two-dimensional magnetic recording in which magnetic moments align parallel to the film/substrate, it requires a heterostructure that behaves as a nano-bar magnet with a magnetization perpendicular to the substrate. Hyun *et al.*[182] fabricated the heterostructures of semiconducting GaAs-ferromagnetic Fe_2Si nanowires and characterized the magnetization of the individual nanowires by magnetic force microscopy. Despite the promising features from their studies, experimental studies along this direction are still at an initial stage.

There is no doubt that graphene has enormous potential as a future material, but at the present we faces may challenges in achieving industrial applications. The chemical vapor deposition (CVD) method is suitable for large-scale and low -cost synthesis of graphene, but damage free transfer technology is a difficult challenge. Direct growth of graphene on the desired substrates might be a reasonable solution in future but it is at an early stage of development at present. Furthermore, the ideal graphene does not have a band gap, which impedes the development of the logic devices. Various attempts to create a band gap in graphene have been made from materials science and device sciences approaches and there is continue ongoing research and studies in this direction. At present graphene, and graphene - based hybrid nanostructures are appealing choices as novel materials for nanotechnology, biomedical engineering, and material science due to their tunable physical properties, high surface area, modified electronic and thermal properties. Since graphene is an inspiration for other 2D materials, system such as hexagonal boron nitride, Germanene, molybdenum dislphide, and different transition metal chalcogenides nanosheets are emerging as new and novel nanostructures for the next generation of materials in nanoscience and nanotechnology research. Focused research and development efforts are required for their industrial-scale applications. Therefore, these 2D materials present new challenges and opportunities in research and development for the material scientists.

A part of the descriptions and discussion of the results presented in this dissertation has appeared in the literature with details given below.

- P. Gajurel, M. Kim, Q. Wang, W. Dai, H. Liu, C. Cen; Vacancy-Controlled Contact Friction in Graphene. Advanced Functional Materials 27(47), 1702832 (2017).

References

[1] K.S. Novoselov, A.K. Geim, S.V. Morozov, D. Jiang, Y. Zhang, S.V. Dubonos, I.V. Grigorieva, A.A. Firsov, Electric Field Effect in Atomically Thin Carbon Films, Science, 306 (2004) 666.

[2] P.R. Wallace, The Band Theory of Graphite, Physical Review, 71 (1947) 622-634.

[3] A.H. Castro Neto, F. Guinea, N.M.R. Peres, K.S. Novoselov, A.K. Geim, The electronic properties of graphene, Reviews of Modern Physics, 81 (2009) 109-162.

[4] C. Kittel, C. Fong, Quantum Theory of Solids, John Wiley & Sons1987.

[5] N. Tombros, A. Veligura, J. Junesch, M.H.D. Guimarães, I.J. Vera-Marun, H.T. Jonkman, B.J. van Wees, Quantized conductance of a suspended graphene nanoconstriction, Nature Physics, 7 (2011) 697-700.

[6] K. Nakayama, K. Nakatani, S. Khamseh, M. Mori, K. Maezawa, Step Hall Measurement of InSb Films Grown on Si(111) Substrate Using InSb Bilayer, Japanese Journal of Applied Physics, 50 (2011) 01BF01.

[7] S.V. Morozov, K.S. Novoselov, M.I. Katsnelson, F. Schedin, D.C. Elias, J.A. Jaszczak, A.K. Geim, Giant Intrinsic Carrier Mobilities in Graphene and Its Bilayer, Physical Review Letters, 100 (2008) 016602.

[8] A.S. Mayorov, R.V. Gorbachev, S.V. Morozov, L. Britnell, R. Jalil, L.A. Ponomarenko, P. Blake, K.S. Novoselov, K. Watanabe, T. Taniguchi, A.K. Geim, Micrometer-Scale Ballistic Transport in Encapsulated Graphene at Room Temperature, Nano Letters, 11 (2011) 2396-2399.

[9] R. Bistritzer, A.H. MacDonald, Moiré bands in twisted double-layer graphene, Proceedings of the National Academy of Sciences, 108 (2011) 12233.

[10] Y. Cao, V. Fatemi, A. Demir, S. Fang, S.L. Tomarken, J.Y. Luo, J.D. Sanchez-Yamagishi, K. Watanabe, T. Taniguchi, E. Kaxiras, R.C. Ashoori, P. Jarillo-Herrero, Correlated insulator behaviour at half-filling in magic-angle graphene superlattices, Nature, 556 (2018) 80-84.

[11] G. Tarnopolsky, A.J. Kruchkov, A. Vishwanath, Origin of Magic Angles in Twisted Bilayer Graphene, Physical Review Letters, 122 (2019) 106405.

[12] R. Ribeiro-Palau, C. Zhang, K. Watanabe, T. Taniguchi, J. Hone, C.R. Dean, Twistable electronics with dynamically rotatable heterostructures, Science, 361 (2018) 690-693.

[13] J. Moser, A. Barreiro, A. Bachtold, Current-induced cleaning of graphene, Applied Physics Letters, 91 (2007) 163513.

[14] F. Schwierz, Graphene transistors, Nature Nanotechnology, 5 (2010) 487-496.

[15] F. Xia, T. Mueller, Y.-m. Lin, A. Valdes-Garcia, P. Avouris, Ultrafast graphene photodetector, Nature Nanotechnology, 4 (2009) 839-843.

[16] N.S. Tambe, B. Bhushan, Friction model for the velocity dependence of nanoscale friction, Nanotechnology, 16 (2005) 2309-2324.

[17] G. Tomlinson, CVI. A molecular theory of friction, The London, Edinburgh, and Dublin philosophical magazine and journal of science, 7 (1929) 905-939.

[18] J. Frenkel, T. Kontorova, On the theory of plastic deformation and twinning, Izv. Akad. Nauk, Ser. Fiz., 1 (1939) 137-149.

[19] J. Krim, Atomic-scale origins of friction, langmuir, 12 (1996) 4564-4566.

[20] M.O. Robbins, J. Krim, Energy dissipation in interfacial friction, MRS BULL, 23 (1998) 23-26.

[21] J. Krim, Friction and energy dissipation mechanisms in adsorbed molecules and molecularly thin films, Advances in Physics, 61 (2012) 155-323.

[22] C.M. Mate, G.M. McClelland, R. Erlandsson, S. Chiang, Atomic-scale friction of a tungsten tip on a graphite surface, Scanning Tunneling Microscopy, Springer1987, pp. 226-229.

[23] G. Amontons, De la resistance cause dans les machines (About Resistance and Force in Machines), Mem. l'Acedemie R, DOI 257-282.

[24] F. Bowden, D. Tabor, The Friction and Lubrication of Solids, Part I, Clarendon, Oxford, 1950.

[25] Y. Mo, K.T. Turner, I. Szlufarska, Friction laws at the nanoscale, Nature, 457 (2009) 1116-1119.

[26] D. Dietzel, M. Feldmann, U.D. Schwarz, H. Fuchs, A. Schirmeisen, Scaling Laws of Structural Lubricity, Physical Review Letters, 111 (2013) 235502.

[27] E. Cihan, S. İpek, E. Durgun, M.Z. Baykara, Structural lubricity under ambient conditions, Nat Commun, 7 (2016) 12055.

[28] E. Koren, U. Duerig, Moiré scaling of the sliding force in twisted bilayer graphene, Physical Review B, 94 (2016) 045401.

[29] E.-S. Yoon, A. Singh, H.-J. Oh, H. Kong, The effect of contact area on nano/micro-scale friction, Wear, 259 (2005) 1424-1431.

[30] E. Gnecco, R. Bennewitz, T. Gyalog, C. Loppacher, M. Bammerlin, E. Meyer, H.-J. Güntherodt, Velocity dependence of atomic friction, Physical Review Letters, 84 (2000) 1172.

[31] Y. Sang, M. Dubé, M. Grant, Thermal effects on atomic friction, Physical Review Letters, 87 (2001) 174301.

[32] L. Jansen, H. Hölscher, H. Fuchs, A. Schirmeisen, Temperature dependence of atomic-scale stick-slip friction, Physical review letters, 104 (2010) 256101.

[33] A. Smolyanitsky, J.P. Killgore, V.K. Tewary, Effect of elastic deformation on frictional properties of few-layer graphene, Physical Review B, 85 (2012) 035412.

[34] S. Li, Q. Li, R.W. Carpick, P. Gumbsch, X.Z. Liu, X. Ding, J. Sun, J. Li, The evolving quality of frictional contact with graphene, Nature, 539 (2016) 541-545.

[35] W. Qu, X. Chen, C. Ke, Temperature-dependent frictional properties of ultra-thin boron nitride nanosheets, Applied Physics Letters, 110 (2017) 143110.

[36] V.L. Popov, J. Gray, Prandtl-Tomlinson model: History and applications in friction, plasticity, and nanotechnologies, Wiley Online Library, 2012.

[37] D. Andersson, A.S. de Wijn, Understanding the friction of atomically thin layered materials, Nat Commun, 11 (2020) 420.

[38] D. Mandelli, I. Leven, O. Hod, M. Urbakh, Sliding friction of graphene/hexagonal –boron nitride heterojunctions: a route to robust superlubricity, Scientific Reports, 7 (2017) 10851.

[39] Z. Chen, A. Khajeh, A. Martini, S.H. Kim, Chemical and physical origins of friction on surfaces with atomic steps, Science advances, 5 (2019) eaaw0513.

[40] T. Filleter, R. Bennewitz, Structural and frictional properties of graphene films on SiC(0001) studied by atomic force microscopy, Physical Review B, 81 (2010) 155412.

[41] C. Lee, Q. Li, W. Kalb, X.-Z. Liu, H. Berger, R.W. Carpick, J. Hone, Frictional characteristics of atomically thin sheets, science, 328 (2010) 76-80.

[42] H. Lee, N. Lee, Y. Seo, J. Eom, S. Lee, Comparison of frictional forces on graphene and graphite, Nanotechnology, 20 (2009) 325701.

[43] P. Egberts, G.H. Han, X.Z. Liu, A.T.C. Johnson, R.W. Carpick, Frictional Behavior of Atomically Thin Sheets: Hexagonal-Shaped Graphene Islands Grown on Copper by Chemical Vapor Deposition, ACS Nano, 8 (2014) 5010-5021.

[44] T. Filleter, J.L. McChesney, A. Bostwick, E. Rotenberg, K.V. Emtsev, T. Seyller, K. Horn, R. Bennewitz, Friction and Dissipation in Epitaxial Graphene Films, Physical Review Letters, 102 (2009) 086102.

[45] C.M. Almeida, R. Prioli, B. Fragneaud, L.G. Cançado, R. Paupitz, D.S. Galvão, M. De Cicco, M.G. Menezes, C.A. Achete, R.B. Capaz, Giant and tunable anisotropy of nanoscale friction in graphene, Scientific reports, 6 (2016) 31569.

[46] F. Ptak, C. Almeida, R. Prioli, Velocity-dependent friction enhances tribomechanical differences between monolayer and multilayer graphene, Scientific reports, 9 (2019).

[47] E. Riedo, E. Gnecco, R. Bennewitz, E. Meyer, H. Brune, Interaction potential and hopping dynamics governing sliding friction, Physical review letters, 91 (2003) 084502.

[48] O.J. Furlong, S.J. Manzi, V.D. Pereyra, V. Bustos, W.T. Tysoe, Kinetic Monte Carlo theory of sliding friction, Physical Review B, 80 (2009) 153408.

[49] S. Kwon, J.-H. Ko, K.-J. Jeon, Y.-H. Kim, J.Y. Park, Enhanced nanoscale friction on fluorinated graphene, Nano letters, 12 (2012) 6043-6048.

[50] Y. Peng, J. Li, X. Tang, B. Liu, X. Chen, L. Bai, Friction Reduction of Hydrogenated Graphene by Strain Engineering, Tribology Letters, 68 (2020) 22.

[51] H.P. Mungse, O.P. Khatri, Chemically Functionalized Reduced Graphene Oxide as a Novel Material for Reduction of Friction and Wear, The Journal of Physical Chemistry C, 118 (2014) 14394-14402.

[52] S. Park, R.S. Ruoff, Chemical methods for the production of graphenes, Nature nanotechnology, 4 (2009) 217-224.

[53] B. Seger, P.V. Kamat, Electrocatalytically active graphene-platinum nanocomposites. Role of 2-D carbon support in PEM fuel cells, The Journal of Physical Chemistry C, 113 (2009) 7990-7995.

[54] H.M. Hassan, V. Abdelsayed, S.K. Abd El Rahman, K.M. AbouZeid, J. Terner, M.S. El-Shall, S.I. Al-Resayes, A.A. El-Azhary, Microwave synthesis of graphene sheets supporting metal nanocrystals in aqueous and organic media, Journal of Materials Chemistry, 19 (2009) 3832-3837.

[55] D.A. Sokolov, K.R. Shepperd, T.M. Orlando, Formation of graphene features from direct laser-induced reduction of graphite oxide, The Journal of Physical Chemistry Letters, 1 (2010) 2633-2636.

[56] G.K. Ramesha, S. Sampath, Electrochemical reduction of oriented graphene oxide films: an in situ Raman spectroelectrochemical study, The Journal of Physical Chemistry C, 113 (2009) 7985-7989.

[57] A. Kongkanand, K. Vinodgopal, S. Kuwabata, P.V. Kamat, Highly dispersed Pt catalysts on single-walled carbon nanotubes and their role in methanol oxidation, The Journal of Physical Chemistry B, 110 (2006) 16185-16188.

[58] L. Ramos-Galicia, L.N. Mendez, A.L. Martínez-Hernández, A. Espindola-Gonzalez, I.R. Galindo-Esquivel, R. Fuentes-Ramirez, C. Velasco-Santos, Improved Performance of an Epoxy Matrix as a Result of Combining Graphene Oxide and Reduced Graphene, International Journal of Polymer Science, 2013 (2013) 493147.

[59] C. Kittel, P. McEuen, J. Wiley, Sons, Introduction to Solid State Physics, John Wiley & Sons, Limited2018.

[60] C.V. Kumar, A. Pattammattel, Chapter 3 - Characterization techniques for graphene, in: C.V. Kumar, A. Pattammattel (Eds.) Introduction to Graphene, Elsevier2017, pp. 45-74.

[61] M. Yi, Z. Shen, Kitchen blender for producing high-quality few-layer graphene, Carbon, 78 (2014) 622-626.

[62] A.C. Ferrari, D.M. Basko, Raman spectroscopy as a versatile tool for studying the properties of graphene, Nature Nanotechnology, 8 (2013) 235-246.

[63] A.C. Ferrari, Raman spectroscopy of graphene and graphite: Disorder, electron–phonon coupling, doping and nonadiabatic effects, Solid State Communications, 143 (2007) 47-57.

[64] K.R. Paton, E. Varrla, C. Backes, R.J. Smith, U. Khan, A. O'Neill, C. Boland, M. Lotya, O.M. Istrate, P. King, Scalable production of large quantities of defect-free few-layer graphene by shear exfoliation in liquids, Nature materials, 13 (2014) 624-630.

[65] A. Smekal, Zur Quantentheorie der Dispersion, Naturwissenschaften, 11 (1923) 873-875.

[66] C.V. Raman, K.S. Krishnan, A New Type of Secondary Radiation, Nature, 121 (1928) 501-502.

[67] D.S. Moore, S.D. McGrane, Raman temperature measurement, Journal of Physics: Conference Series, 500 (2014) 192011.

[68] A. Pattammattel, C.V. Kumar, Kitchen Chemistry 101: Multigram Production of High Quality Biographene in a Blender with Edible Proteins, Advanced Functional Materials, 25 (2015) 7088-7098.

[69] Y. Liu, Z. Liu, W.S. Lew, Q.J. Wang, Temperature dependence of the electrical transport properties in few-layer graphene interconnects, Nanoscale Research Letters, 8 (2013) 335.

[70] I. Childres, L.A. Jauregui, W. Park, H. Cao, Y.P. Chen, Raman spectroscopy of graphene and related materials, New developments in photon and materials research, 1 (2013) 1-20.

[71] A.C. Ferrari, J.C. Meyer, V. Scardaci, C. Casiraghi, M. Lazzeri, F. Mauri, S. Piscanec, D. Jiang, K.S. Novoselov, S. Roth, A.K. Geim, Raman Spectrum of Graphene and Graphene Layers, Physical Review Letters, 97 (2006) 187401.

[72] A. Zandiatashbar, G.-H. Lee, S.J. An, S. Lee, N. Mathew, M. Terrones, T. Hayashi, C.R. Picu, J. Hone, N. Koratkar, Effect of defects on the intrinsic strength and stiffness of graphene, Nat Commun, 5 (2014) 3186.

[73] L.G. Cançado, A. Jorio, E.M. Ferreira, F. Stavale, C.A. Achete, R.B. Capaz, M.V.d.O. Moutinho, A. Lombardo, T. Kulmala, A.C. Ferrari, Quantifying defects in graphene via Raman spectroscopy at different excitation energies, Nano letters, 11 (2011) 3190-3196.

[74] M.M. Lucchese, F. Stavale, E.M. Ferreira, C. Vilani, M.V.d.O. Moutinho, R.B. Capaz, C.A. Achete, A. Jorio, Quantifying ion-induced defects and Raman relaxation length in graphene, Carbon, 48 (2010) 1592-1597.

[75] A. Eckmann, A. Felten, A. Mishchenko, L. Britnell, R. Krupke, K.S. Novoselov, C. Casiraghi, Probing the nature of defects in graphene by Raman spectroscopy, Nano letters, 12 (2012) 3925-3930.

[76] P.T. Araujo, M. Terrones, M.S. Dresselhaus, Defects and impurities in graphene-like materials, Materials Today, 15 (2012) 98-109.

[77] C. Lee, X. Wei, J.W. Kysar, J. Hone, Measurement of the elastic properties and intrinsic strength of monolayer graphene, science, 321 (2008) 385-388.

[78] S. Mathew, T. Chan, D. Zhan, K. Gopinadhan, A. Roy Barman, M. Breese, S. Dhar, Z. Shen, T. Venkatesan, J.T. Thong, Mega-electron-volt proton irradiation on supported and suspended graphene: A Raman spectroscopic layer dependent study, Journal of Applied Physics, 110 (2011) 084309.

[79] Y. Hernandez, V. Nicolosi, M. Lotya, F.M. Blighe, Z. Sun, S. De, I.T. McGovern, B. Holland, M. Byrne, Y.K. Gun'Ko, J.J. Boland, P. Niraj, G. Duesberg, S. Krishnamurthy, R. Goodhue, J. Hutchison, V. Scardaci, A.C. Ferrari, J.N. Coleman, High-yield production of graphene by liquid-phase exfoliation of graphite, Nature Nanotechnology, 3 (2008) 563-568.

[80] L. Stobinski, B. Lesiak, A. Malolepszy, M. Mazurkiewicz, B. Mierzwa, J. Zemek, P. Jiricek, I. Bieloshapka, Graphene oxide and reduced graphene oxide studied by the XRD, TEM and electron spectroscopy methods, Journal of Electron Spectroscopy and Related Phenomena, 195 (2014) 145-154.

[81] A. Kaushal, S.K. Dhawan, V. Singh, Determination of crystallite size, number of graphene layers and defect density of graphene oxide (GO) and reduced graphene oxide (RGO), AIP Conference Proceedings, 2115 (2019) 030106.

[82] M.S. Seehra, U.K. Geddam, D. Schwegler-Berry, A.B. Stefaniak, Detection and quantification of 2H and 3R phases in commercial graphene-based materials, Carbon, 95 (2015) 818-823.

[83] M.S. Seehra, V. Narang, U.K. Geddam, A.B. Stefaniak, Correlation between X-ray diffraction and Raman spectra of 16 commercial graphene-based materials and their resulting classification, Carbon N Y, 111 (2017) 380-384.

[84] M. Craciun, S. Russo, M. Yamamoto, J.B. Oostinga, A. Morpurgo, S. Tarucha, Trilayer graphene is a semimetal with a gate-tunable band overlap, Nature nanotechnology, 4 (2009) 383-388.

[85] C.H. Lui, Z. Li, K.F. Mak, E. Cappelluti, T.F. Heinz, Observation of an electrically tunable band gap in trilayer graphene, Nature Physics, 7 (2011) 944-947.

[86] H. Shi, J. Barker, M.Y. Saïdi, R. Koksbang, L. Morris, Graphite structure and lithium intercalation, Journal of Power Sources, 68 (1997) 291-295.

[87] E. Matuyama, Rate of transformation of rhombohedral graphite at high temperatures, Nature, 178 (1956) 1459-1460.

[88] F. Lavini, F. Cellini, M. Rejhon, J. Kunc, C. Berger, W. de Heer, E. Riedo, Atomic force microscopy phase imaging of epitaxial graphene films, Journal of Physics: Materials, 3 (2020) 024005.

[89] B. Cappella, G. Dietler, Force-distance curves by atomic force microscopy, Surface science reports, 34 (1999) 1-104.

[90] A.M. Goossens, V.E. Calado, A. Barreiro, K. Watanabe, T. Taniguchi, L.M.K. Vandersypen, Mechanical cleaning of graphene, Applied Physics Letters, 100 (2012) 073110.

[91] C.T. Gibson, G.S. Watson, S. Myhra, Lateral force microscopy—a quantitative approach, Wear, 213 (1997) 72-79.

[92] S. Fukada, Y. Shintani, M. Shimomura, F. Tahara, R. Yagi, Graphene Made by Mechanical Exfoliation of Graphite Intercalation Compound, Japanese Journal of Applied Physics, 51 (2012) 085101.

[93] O. Frank, M. Kalbac, 2 - Chemical vapor deposition (CVD) growth of graphene films, in: V. Skákalová, A.B. Kaiser (Eds.) Graphene, Woodhead Publishing2014, pp. 27-49.

[94] T.C. Achee, W. Sun, J.T. Hope, S.G. Quitzau, C.B. Sweeney, S.A. Shah, T. Habib, M.J. Green, High-yield scalable graphene nanosheet production from compressed graphite using electrochemical exfoliation, Scientific Reports, 8 (2018) 14525.

[95] X. Chen, L. Zhang, S. Chen, Large area CVD growth of graphene, Synthetic Metals, 210 (2015) 95-108.

[96] V. Borovikov, A. Zangwill, Step-edge instability during epitaxial growth of graphene from SiC(0001), Physical Review B, 80 (2009) 121406.

[97] L. Speyer, S. Fontana, S. Cahen, C. Hérold, Simple production of high-quality graphene foams by pyrolysis of sodium ethoxide, Materials Chemistry and Physics, 219 (2018) 57-66.

[98] K.S. Novoselov, A.K. Geim, S.V. Morozov, D. Jiang, Y. Zhang, S.V. Dubonos, I.V. Grigorieva, A.A. Firsov, Electric field effect in atomically thin carbon films, science, 306 (2004) 666-669.

[99] K.S. Kim, Y. Zhao, H. Jang, S.Y. Lee, J.M. Kim, K.S. Kim, J.-H. Ahn, P. Kim, J.-Y. Choi, B.H. Hong, Large-scale pattern growth of graphene films for stretchable transparent electrodes, Nature, 457 (2009) 706-710.

[100] Y. Lee, S. Bae, H. Jang, S. Jang, S.-E. Zhu, S.H. Sim, Y.I. Song, B.H. Hong, J.-H. Ahn, Wafer-Scale Synthesis and Transfer of Graphene Films, Nano Letters, 10 (2010) 490-493.

[101] A. Reina, H. Son, L. Jiao, B. Fan, M.S. Dresselhaus, Z. Liu, J. Kong, Transferring and Identification of Single- and Few-Layer Graphene on Arbitrary Substrates, The Journal of Physical Chemistry C, 112 (2008) 17741-17744.

[102] S. Bae, H. Kim, Y. Lee, X. Xu, J.-S. Park, Y. Zheng, J. Balakrishnan, T. Lei, H. Ri Kim, Y.I. Song, Y.-J. Kim, K.S. Kim, B. Özyilmaz, J.-H. Ahn, B.H. Hong, S. Iijima, Roll-to-roll production of 30-inch graphene films for transparent electrodes, Nature Nanotechnology, 5 (2010) 574-578.

[103] Z.-Y. Juang, C.-Y. Wu, A.-Y. Lu, C.-Y. Su, K.-C. Leou, F.-R. Chen, C.-H. Tsai, Graphene synthesis by chemical vapor deposition and transfer by a roll-to-roll process, Carbon, 48 (2010) 3169-3174.

[104] S.Y. Yang, J.G. Oh, D.Y. Jung, H. Choi, C.H. Yu, J. Shin, C.-G. Choi, B.J. Cho, S.-Y. Choi, Metal-Etching-Free Direct Delamination and Transfer of Single-Layer Graphene with a High Degree of Freedom, Small, 11 (2015) 175-181.

[105] Y. REN, C. ZHU, W. CAI, H. LI, Y. HAO, Y. WU, S. CHEN, Q. WU, R.D. PINER, R.S. RUOFF, AN IMPROVED METHOD FOR TRANSFERRING GRAPHENE GROWN BY CHEMICAL VAPOR DEPOSITION, Nano, 07 (2012) 1150001.

[106] X. Yang, H. Peng, Q. Xie, Y. Zhou, Z. Liu, Clean and efficient transfer of CVD-grown graphene by electrochemical etching of metal substrate, Journal of Electroanalytical Chemistry, 688 (2013) 243-248.

[107] G.J.M. Fechine, I. Martin-Fernandez, G. Yiapanis, R. Bentini, E.S. Kulkarni, R.V. Bof de Oliveira, X. Hu, I. Yarovsky, A.H. Castro Neto, B. Özyilmaz, Direct dry transfer of chemical vapor deposition graphene to polymeric substrates, Carbon, 83 (2015) 224-231.

[108] L.G.P. Martins, Y. Song, T. Zeng, M.S. Dresselhaus, J. Kong, P.T. Araujo, Direct transfer of graphene onto flexible substrates, Proceedings of the National Academy of Sciences, 110 (2013) 17762.

[109] M. BOUŠA, M. KALBÁČ, I. JIRKA, L. KAVAN, O. FRANK, Experimental Study of PIB-Based CVD Graphene Transfer Efficiency, DOI (2015).

[110] G. Deokar, J. Avila, I. Razado-Colambo, J.L. Codron, C. Boyaval, E. Galopin, M.C. Asensio, D. Vignaud, Towards high quality CVD graphene growth and transfer, Carbon, 89 (2015) 82-92.

[111] Z. Cheng, Q. Zhou, C. Wang, Q. Li, C. Wang, Y. Fang, Toward Intrinsic Graphene Surfaces: A Systematic Study on Thermal Annealing and Wet-Chemical Treatment of SiO2-Supported Graphene Devices, Nano Letters, 11 (2011) 767-771.

[112] G. Borin Barin, Y. Song, I. de Fátima Gimenez, A.G. Souza Filho, L.S. Barreto, J. Kong, Optimized graphene transfer: Influence of polymethylmethacrylate (PMMA) layer concentration and baking time on graphene final performance, Carbon, 84 (2015) 82-90.

[113] A. Pirkle, J. Chan, A. Venugopal, D. Hinojos, C.W. Magnuson, S. McDonnell, L. Colombo, E.M. Vogel, R.S. Ruoff, R.M. Wallace, The effect of chemical residues on the physical and electrical properties of chemical vapor deposited graphene transferred to SiO2, Applied Physics Letters, 99 (2011) 122108.

[114] W.-H. Lin, T.-H. Chen, J.-K. Chang, J.-I. Taur, Y.-Y. Lo, W.-L. Lee, C.-S. Chang, W.-B. Su, C.-I. Wu, A Direct and Polymer-Free Method for Transferring Graphene Grown by Chemical Vapor Deposition to Any Substrate, ACS Nano, 8 (2014) 1784-1791.

[115] G. Zhang, A.G. Güell, P.M. Kirkman, R.A. Lazenby, T.S. Miller, P.R. Unwin, Versatile Polymer-Free Graphene Transfer Method and Applications, ACS Applied Materials & Interfaces, 8 (2016) 8008-8016.

[116] Handbook of Chemistry. Rev. 10th ed. Compiled and edited by Norbert A. Lange. McGraw-Hill Book Co., Inc., 330W. 42nd St., New York, NY 10036, 1967. xiv + 2001pp. 13.5 × 20.5cm. Price $12.00, Journal of Pharmaceutical Sciences, 57 (1968) 356.

[117] Y.-C. Lin, C.-C. Lu, C.-H. Yeh, C. Jin, K. Suenaga, P.-W. Chiu, Graphene Annealing: How Clean Can It Be?, Nano Letters, 12 (2012) 414-419.

[118] M. Lucchese, F. Stavale, E. Martins Ferreira, C. Vilani, M. Moutinho, R. Capaz, C. Achete, A. Jorio, Quantifying ion-induced defects and Raman relaxation length in graphene, Carbon, 48 (2010) 1592-1597.

[119] T. Gokus, R.R. Nair, A. Bonetti, M. Böhmler, A. Lombardo, K.S. Novoselov, A.K. Geim, A.C. Ferrari, A. Hartschuh, Making Graphene Luminescent by Oxygen Plasma Treatment, ACS Nano, 3 (2009) 3963-3968.

[120] L.G. Cançado, A. Jorio, E.H.M. Ferreira, F. Stavale, C.A. Achete, R.B. Capaz, M.V.O. Moutinho, A. Lombardo, T.S. Kulmala, A.C. Ferrari, Quantifying Defects in Graphene via Raman Spectroscopy at Different Excitation Energies, Nano Letters, 11 (2011) 3190-3196.

[121] B. Gupta, N. Kumar, K. Panda, V. Kanan, S. Joshi, I. Visoly-Fisher, Role of oxygen functional groups in reduced graphene oxide for lubrication, Scientific Reports, 7 (2017) 45030.

[122] P. Vecera, J.C. Chacón-Torres, T. Pichler, S. Reich, H.R. Soni, A. Görling, K. Edelthalhammer, H. Peterlik, F. Hauke, A. Hirsch, Precise determination of graphene functionalization by in situ Raman spectroscopy, Nat Commun, 8 (2017) 15192-15192.

[123] F. Banhart, J. Kotakoski, A.V. Krasheninnikov, Structural Defects in Graphene, ACS Nano, 5 (2011) 26-41.

[124] D. Yang, A. Velamakanni, G. Bozoklu, S. Park, M. Stoller, R.D. Piner, S. Stankovich, I. Jung, D.A. Field, C.A. Ventrice, R.S. Ruoff, Chemical analysis of graphene oxide films after heat and chemical treatments by X-ray photoelectron and Micro-Raman spectroscopy, Carbon, 47 (2009) 145-152.

[125] P. Pokharel, B. Pant, K. Pokhrel, H.R. Pant, J.-g. Lim, D.S. Lee, H.-Y. Kim, S. Choi, Effects of functional groups on the graphene sheet for improving the thermomechanical properties of polyurethane nanocomposites, Composites Part B: Engineering, 78 (2015) 192-201.

[126] M.S. Dresselhaus, A. Jorio, M. Hofmann, G. Dresselhaus, R. Saito, Perspectives on Carbon Nanotubes and Graphene Raman Spectroscopy, Nano Letters, 10 (2010) 751-758.

[127] H.J. Hwang, Y. Lee, C. Cho, B.H. Lee, Facile process to clean PMMA residue on graphene using KrF laser annealing, AIP Advances, 8 (2018) 105326.

[128] A. Piazza, F. Giannazzo, G. Buscarino, G. Fisichella, A. La Magna, F. Roccaforte, M. Cannas, F.M. Gelardi, S. Agnello, In-situ monitoring by Raman spectroscopy of the thermal doping of graphene and MoS2 in O2-controlled atmosphere, Beilstein Journal of Nanotechnology, 8 (2017) 418-424.

[129] J. Hong, M.K. Park, E.J. Lee, D. Lee, D.S. Hwang, S. Ryu, Origin of New Broad Raman D and G Peaks in Annealed Graphene, Scientific Reports, 3 (2013) 2700.

[130] S. Berciaud, S. Ryu, L.E. Brus, T.F. Heinz, Probing the Intrinsic Properties of Exfoliated Graphene: Raman Spectroscopy of Free-Standing Monolayers, Nano Letters, 9 (2009) 346-352.

[131] A. Das, S. Pisana, B. Chakraborty, S. Piscanec, S.K. Saha, U.V. Waghmare, K.S. Novoselov, H.R. Krishnamurthy, A.K. Geim, A.C. Ferrari, A.K. Sood, Monitoring dopants by Raman scattering in an electrochemically top-gated graphene transistor, Nature Nanotechnology, 3 (2008) 210-215.

[132] A.K. Geim, K.S. Novoselov, The rise of graphene, Nanoscience and technology: a collection of reviews from nature journals, World Scientific2010, pp. 11-19.

[133] N. Peres, Colloquium: The transport properties of graphene: An introduction, Reviews of modern physics, 82 (2010) 2673.

[134] K.S. Novoselov, A.K. Geim, S.V. Morozov, D. Jiang, M.I. Katsnelson, I. Grigorieva, S. Dubonos, Firsov, AA, Two-dimensional gas of massless Dirac fermions in graphene, nature, 438 (2005) 197-200.

[135] Y. Zhang, Y.-W. Tan, H.L. Stormer, P. Kim, Experimental observation of the quantum Hall effect and Berry's phase in graphene, nature, 438 (2005) 201-204.

[136] K.S. Novoselov, D. Jiang, F. Schedin, T. Booth, V. Khotkevich, S. Morozov, A.K. Geim, Two-dimensional atomic crystals, Proceedings of the National Academy of Sciences, 102 (2005) 10451-10453.

[137] F. Schedin, A.K. Geim, S.V. Morozov, E. Hill, P. Blake, M. Katsnelson, K.S. Novoselov, Detection of individual gas molecules adsorbed on graphene, Nature materials, 6 (2007) 652-655.

[138] S.D. Sarma, S. Adam, E. Hwang, E. Rossi, Electronic transport in two-dimensional graphene, Reviews of modern physics, 83 (2011) 407.

[139] G. Mikitik, Y.V. Sharlai, Manifestation of Berry's phase in metal physics, Physical review letters, 82 (1999) 2147.

[140] I.P. Batra, Origin of conductance quantization, Surface science, 395 (1998) 43-45.

[141] E. Gorbar, V. Gusynin, V. Miransky, I. Shovkovy, Magnetic field driven metal-insulator phase transition in planar systems, Physical Review B, 66 (2002) 045108.

[142] K.S. Novoselov, E. McCann, S. Morozov, V.I. Fal'ko, M. Katsnelson, U. Zeitler, D. Jiang, F. Schedin, A. Geim, Unconventional quantum Hall effect and Berry's phase of 2π in bilayer graphene, Nature physics, 2 (2006) 177-180.

[143] K. Nomura, A. MacDonald, Quantum transport of massless Dirac fermions, Physical review letters, 98 (2007) 076602.

[144] J. Martin, N. Akerman, G. Ulbricht, T. Lohmann, J.v. Smet, K. Von Klitzing, A. Yacoby, Observation of electron–hole puddles in graphene using a scanning single-electron transistor, Nature physics, 4 (2008) 144-148.

[145] L. Moriconi, D. Niemeyer, Graphene conductivity near the charge neutral point, Physical Review B, 84 (2011) 193401.

[146] K. Kechedzhi, V.I. Fal'ko, E. McCann, B. Altshuler, Influence of trigonal warping on interference effects in bilayer graphene, Physical review letters, 98 (2007) 176806.

[147] G. Jnawali, M. Huang, J.F. Hsu, H. Lee, J.W. Lee, P. Irvin, C.B. Eom, B. D'Urso, J. Levy, Room-Temperature Quantum Transport Signatures in Graphene/LaAlO3/SrTiO3 Heterostructures, Advanced Materials, 29 (2017) 1603488.

[148] S. Konschuh, M. Gmitra, J. Fabian, Tight-binding theory of the spin-orbit coupling in graphene, Physical Review B, 82 (2010) 245412.

[149] T. Ando, T. Nakanishi, R. Saito, Berry's phase and absence of back scattering in carbon nanotubes, Journal of the Physical Society of Japan, 67 (1998) 2857-2862.

[150] E. McCann, V.I. Fal'ko, Landau-level degeneracy and quantum Hall effect in a graphite bilayer, Physical review letters, 96 (2006) 086805.

[151] A. Morpurgo, F. Guinea, Intervalley scattering, long-range disorder, and effective time-reversal symmetry breaking in graphene, Physical review letters, 97 (2006) 196804.

[152] F. Tikhonenko, D. Horsell, R. Gorbachev, A. Savchenko, Weak localization in graphene flakes, Physical review letters, 100 (2008) 056802.

[153] F. Tikhonenko, A. Kozikov, A. Savchenko, R. Gorbachev, Transition between electron localization and antilocalization in graphene, Physical Review Letters, 103 (2009) 226801.

[154] G. Bergmann, Weak localization in thin films: a time-of-flight experiment with conduction electrons, Physics Reports, 107 (1984) 1-58.

[155] C. Beenakker, H. Van Houten, Boundary scattering and weak localization of electrons in a magnetic field, Physical Review B, 38 (1988) 3232.

[156] M. Hilke, M. Massicotte, E. Whiteway, V. Yu, Weak localization in graphene: theory, simulations, and experiments, The Scientific World Journal, 2014 (2014).

[157] E. McCann, K. Kechedzhi, V.I. Fal'ko, H. Suzuura, T. Ando, B. Altshuler, Weak-localization magnetoresistance and valley symmetry in graphene, Physical Review Letters, 97 (2006) 146805.

[158] X. Li, Y. Zhu, W. Cai, M. Borysiak, B. Han, D. Chen, R.D. Piner, L. Colombo, R.S. Ruoff, Transfer of Large-Area Graphene Films for High-Performance Transparent Conductive Electrodes, Nano Letters, 9 (2009) 4359-4363.

[159] C. Gómez-Navarro, R.T. Weitz, A.M. Bittner, M. Scolari, A. Mews, M. Burghard, K. Kern, Electronic Transport Properties of Individual Chemically Reduced Graphene Oxide Sheets, Nano Letters, 7 (2007) 3499-3503.

[160] M.S. Seehra, V. Narang, U.K. Geddam, A.B. Stefaniak, Correlation between X-ray diffraction and Raman spectra of 16 commercial graphene–based materials and their resulting classification, Carbon, 111 (2017) 380-385.

[161] M.M. Lucchese, F. Stavale, E.H.M. Ferreira, C. Vilani, M.V.O. Moutinho, R.B. Capaz, C.A. Achete, A. Jorio, Quantifying ion-induced defects and Raman relaxation length in graphene, Carbon, 48 (2010) 1592-1597.

[162] R.J.W.E. Lahaye, H.K. Jeong, C.Y. Park, Y.H. Lee, Density functional theory study of graphite oxide for different oxidation levels, Physical Review B, 79 (2009) 125435.

[163] M.C. Kim, G.S. Hwang, R.S. Ruoff, Epoxide reduction with hydrazine on graphene: A first principles study, The Journal of Chemical Physics, 131 (2009) 064704.

[164] M.F. El-Kady, V. Strong, S. Dubin, R.B. Kaner, Laser scribing of high-performance and flexible graphene-based electrochemical capacitors, Science, 335 (2012) 1326-1330.

[165] L.J. Cote, R. Cruz-Silva, J. Huang, Flash Reduction and Patterning of Graphite Oxide and Its Polymer Composite, Journal of the American Chemical Society, 131 (2009) 11027-11032.

[166] J.S. Choi, J.-S. Kim, I.-S. Byun, D.H. Lee, M.J. Lee, B.H. Park, C. Lee, D. Yoon, H. Cheong, K.H. Lee, Friction anisotropy–driven domain imaging on exfoliated monolayer graphene, Science, 333 (2011) 607-610.

[167] Z. Zhang, J. Yin, X. Liu, J. Li, J. Zhang, W. Guo, Substrate-Sensitive Graphene Oxidation, The Journal of Physical Chemistry Letters, 7 (2016) 867-873.

[168] L. Liu, S. Ryu, M.R. Tomasik, E. Stolyarova, N. Jung, M.S. Hybertsen, M.L. Steigerwald, L.E. Brus, G.W. Flynn, Graphene Oxidation: Thickness-Dependent Etching and Strong Chemical Doping, Nano Letters, 8 (2008) 1965-1970.

[169] P.K. Gogoi, P.E. Trevisanutto, M. Yang, I. Santoso, T.C. Asmara, A. Terentjevs, F. Della Sala, M.B.H. Breese, T. Venkatesan, Y.P. Feng, K.P. Loh, A.H.C. Neto, A. Rusydi, Optical conductivity renormalization of graphene on $\mathrm{SrTiO_3}$ due to resonant excitonic effects mediated by Ti3d orbitals, Physical Review B, 91 (2015) 035424.

[170] A. Cresti, N. Nemec, B. Biel, G. Niebler, F. Triozon, G. Cuniberti, S. Roche, Charge transport in disordered graphene-based low dimensional materials, Nano Research, 1 (2008) 361-394.

[171] A. Lherbier, S.M.M. Dubois, X. Declerck, Y.-M. Niquet, S. Roche, J.-C. Charlier, Transport properties of graphene containing structural defects, Physical Review B, 86 (2012) 075402.

[172] G.M. Minkov, A.V. Germanenko, O.E. Rut, A.A. Sherstobitov, B.N. Zvonkov, Giant suppression of the Drude conductivity due to quantum interference in the disordered two-dimensional system $\mathrm{GaAs/In_xGa_{1\text{-}x}/\ GaAs}$, Physical Review B, 75 (2007) 235316.

[173] B.L. Altshuler, D. Khmel'nitzkii, A.I. Larkin, P.A. Lee, Magnetoresistance and Hall effect in a disordered two-dimensional electron gas, Physical Review B, 22 (1980) 5142-5153.

[174] A. Lherbier, S.M.-M. Dubois, X. Declerck, S. Roche, Y.-M. Niquet, J.-C. Charlier, Two-dimensional graphene with structural defects: elastic mean free path, minimum conductivity, and Anderson transition, Physical review letters, 106 (2011) 046803.

[175] N. Leconte, A. Lherbier, F. Varchon, P. Ordejon, S. Roche, J.-C. Charlier, Quantum transport in chemically modified two-dimensional graphene: From minimal conductivity to Anderson localization, Physical Review B, 84 (2011) 235420.

[176] Y.-W. Son, M.L. Cohen, S.G. Louie, Energy gaps in graphene nanoribbons, Physical review letters, 97 (2006) 216803.

[177] T. Li, Y. Huang, S. Chang, C. Chang, M.-F. Lin, Magnetoconductance of graphene nanoribbons, Philosophical Magazine, 89 (2009) 697-709.

[178] N. Peres, A.C. Neto, F. Guinea, Dirac fermion confinement in graphene, Physical Review B, 73 (2006) 241403.

[179] J. Bai, R. Cheng, F. Xiu, L. Liao, M. Wang, A. Shailos, K.L. Wang, Y. Huang, X. Duan, Very large magnetoresistance in graphene nanoribbons, Nature Nanotechnology, 5 (2010) 655-659.

[180] S. Thornhill, N. Wu, Z.F. Wang, Q.W. Shi, J. Chen, Graphene nanoribbon field-effect transistors, 2008 IEEE International Symposium on Circuits and Systems, 2008, pp. 169-172.

[181] Y.-C. Lin, Y. Chen, Y. Huang, Nanoelectronic Devices from Nanowire Heterostructures, ECS Transactions, 33 (2019) 3-11.

[182] J.K. Hyun, S. Zhang, 5 - Growth of nanowire heterostructures and their optoelectronic and spintronic applications, in: M. Vázquez (Ed.) Magnetic Nano- and Microwires (Second Edition), Woodhead Publishing2020, pp. 103-133.